ELECTROMAGNETIC WAVE PHENOMENA IN PERIODIC METASTRUCTURES

by

John Otto Schenk

A dissertation submitted to the faculty of
The University of North Carolina at Charlotte
in partial fulfillment of the requirements
for the degree of Doctor of Philosophy in
Optical Science and Engineering

Charlotte

2010

Approved by:

_____
Dr. Michael A. Fiddy

_____
Dr. Greg J. Gbur

_____
Dr. Angela D. Davies

_____
Dr. Yong Zhang

ABSTRACT

JOHN SCHENK. Electromagnetic wave phenomena in periodic metastructures. (Under the direction of DR. MICHAEL A. FIDDY.)

There is an active effort toward the development of negative index metamaterials for application in high-resolution imaging. In particular, engineering an artificial material exhibiting an index of exactly -1, may permit sub-wavelength imaging. This research was directed toward the development of a negative one index metamaterial using a modified version of an S patterned meta model designed and experimentally tested by Jin Au Kong. This modified S model provided the necessary insight into the basic elementary parameters responsible for realizing a negative index. Based on this, it became clear how variable conductivity could result in achieving a –1 index. What followed was an investigation into the Drude model of conductivity. This model though not physically realizable demonstrated a negative one-index metamaterial using CST (Computer Simulation Technology) software, and high-resolution imaging was accomplished using the Drude model and CST simulations. These encouraging numerical results provided an ideal model for development toward a physically realizable –1 index meta model. Three different thickness metamaterial negative index lens models were designed using CST having indices in the range of -0.8 and with reasonably low loss. We examined the difficulties in adjusting the designs to better approach -1. These models were built and tested experimentally for comparison with CST simulations, but due specifically to loss made the possibility of viewing images difficult. The primary conclusion is that without a –1 index, the resulting image resolution seen in the simulation would not be significantly improved over the traditional diffraction limit. It

was also established that it may be difficult to make further progress toward a -1 index using fixed conductivity models in view of coupling between the many variables involved that determined the actual index in the real built models.

ACKNOWLEDGMENTS

It has been a blessing to have the advice and guidance of many talented people, whose knowledge and skills helped make it possible to accomplish this research of Electromagnetic Wave Phenomena in Periodic Structures. It is with great pleasure that the author once again expresses his gratitude to Dr. Michael A. Fiddy in the Department of Physics & Optical Science at UNCC for his guidance, patience, encouragement, support and most of all, his scholarly example of building upon the work accomplished throughout academia. Without these this work would not have come to completion. Thank you, Dr. Fiddy.

The author further acknowledges another blessing, Dr. Walter Niblack for his contribution of unending knowledge, inspirational support and long-standing academic mentor. Thank you, Dr. Niblack.

Special thanks in memory of my cousin Joseph William Mezzapelle for always being available to help me throughout my life since childhood. Joey supported experimental science in the study of electricity and magnetism. He could never say no to any request involving the pursuit of higher learning, especially electrical experiments. I thank God for his existence in my life.

Paula Daniels; a blessed friend and English tutor for many academic years of my life. Thank you Paula.

Last but not least, the author acknowledges Dr.Yang Cao from the Department of Physics and Optical Science from UNCC for her tireless contribution of optical engineering.

TABLE OF CONTENTS

LIST OF FIGURES

CHAPTER 1: INTRODUCTION

This research has focused on the novel electromagnetic properties of artificially structured materials, i.e. that do not occur naturally. Our interest in these metastructures or metamaterials was initially stimulated by the claim that one particular design for such a metastructure could slow electromagnetic waves down considerably while also greatly enhancing its intensity. This theoretical prediction was made early in 2005 by Figotin and Vitebskiy [1] from the University of California Irvine. They showed that a gigantic transmission band-edge resonance in periodic stacks of anisotropic layers could be realized from a specific material prescription of misaligned anisotropy in each period [1]. This theory became the stimulus for our metamaterials development and applications.

We first attempted to numerically model and then build such a structure based on this theory, which assumed low loss materials and an infinite half-space. Their prediction was that for certain specific band edge characteristics (such as a degenerate band edge (DBE)) large slow down factors and high enhancements would be apparent. Fabrication of the DBE structure was first considered for use at optical frequencies, but the high degrees of birefringence required made this difficult. We then redirected our efforts to designing and building a lower frequency structure. In addition, it was designed as a form birefringent structure to provide insights on the importance of dimensional tolerances for a future optical structure. In other words, this would provide insights for effective nanopatterning. The microwave X band was selected given that these devices, such as

antennas, transmitters and receivers are common in this frequency range between 8 and 12 GHz. The microwave structures were made to our specification using a rapid prototyping tool. Rapid prototyping capabilities were available at Western Carolina University (WCU). After an extended period of experimental trials enough evidence was collected showing results that did represent a significant field enhancement response, which reached a factor of eighty and at a location consistent with the theory. This result (discussed later and shown in FIGURE 4) was presented at the OSA Topical Meeting on Slow Light in Salt Lake City Utah, 2007.

We also found enhancement factors smaller than expected but these were attributed to structural degradations and increasing tolerance errors over time. During this early investigation into metastructures further insight was gained into effectively characterizing the elements or parameters leading to quantifiable enhancement. This period provided the needed experience to continue on with further development in this chosen field of electromagnetic phenomena. A significant amount of published literature was available linking small degrees of disorder to rapid declines in enhancement factor (Jung and Teixeira [2]) and the difficulty in realizing a DBE (or SBE (see Chabanov [3]) point in practice. A review was conducted to understand the issues and it was determined that the mechanical precision required prevented the experimental data from approaching ideal theory. In view of both experimental and manufacturing issues further investigation would be needed. What followed were two issues that needed ongoing study in order to continue this line of research. One was a higher index contrast that in turn required starting material indices higher than were available before they were patterned for form birefringence. This would permit thinner and perhaps more easily fabricated elements.

Other difficulties involved were related to designing non-standard microwave test probes that correctly matched the characteristic impedance of the physical microwave test structures. . Today material development is on going while the test equipment setup is being used for many parallel tasks. This early work was useful experience but the research direction of this dissertation has since focused on a different challenge, field enhancement and negative index.

1.1 Field Enhancement And Negative Index

Electromagnetic field enhancement is relevant to a wide variety of interesting applications, such as heightened wireless reception sensitivity, automotive ignition, optical sensors, and well-known devices such as spark gap transmitters. These types of transmitters were founded on the conceptual basis of resonance phenomena. Electrical resonance is a special case condition existing in RCL (Resistance, Capacitance and Inductance) circuits. When various topological constructs of RCL become energized or excited at a frequency in which the inductive reactance equals the capacitance reactance, then one has the well-known condition of resonance. One example of how to use this special condition is seen below in FIGURE 1.

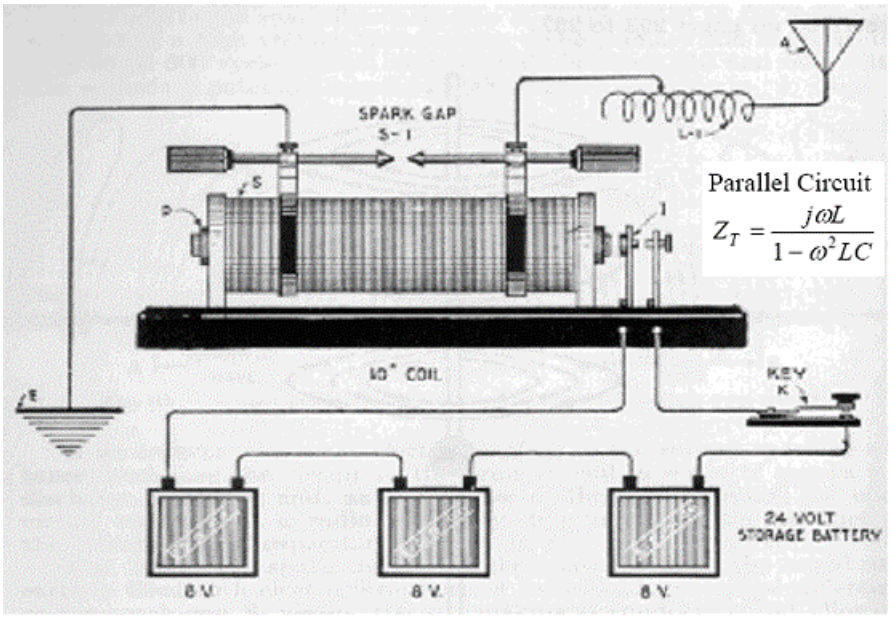

FIGURE 1: Spark gap wireless transmitter

FIGURE 1 represents a practical realization and construction of a parallel RCL circuit whose impedance follows the mathematical expression located in the upper right side of FIGURE 1. This equation simply states that at resonance the electrical impedance will be maximized. It is exactly this behavior that directly underlies field enhancement. Electrical resonance phenomena depend primarily on two material properties that associate indirectly with L (inductance) based on permeability and C (capacitance) based on permittivity. It is also helpful to introduce here, though briefly, and again later on, that conductivity plays a key role in the development of electrical resonance. To further emphasize the elementary electrical characteristic properties of the spark gap transmitter, a schematic diagram is introduced in FIGURE 2. One final point related to resonance is that these enhanced fields tend to be localized to some prescribed position as can be seen by the placement of the spark gap in FIGURE 2.

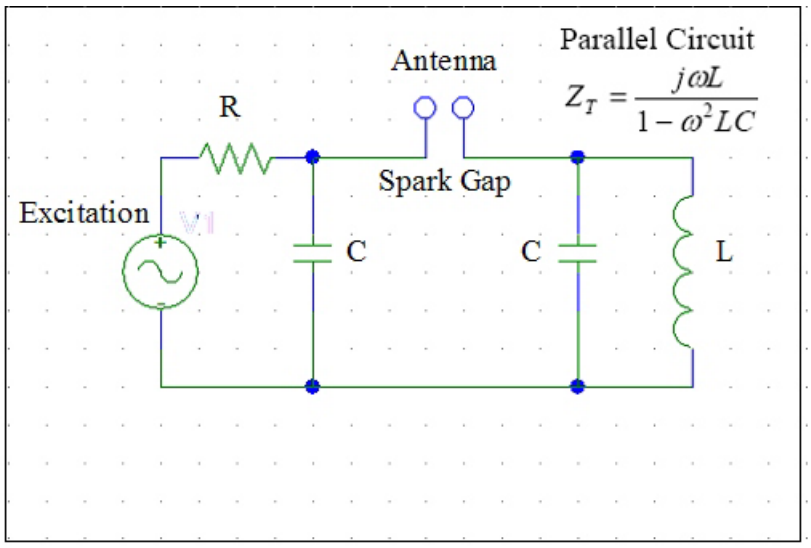

FIGURE 2: Spark gap wireless transmitter circuit

This basic circuit is described by σ (conductivity), ε (permittivity) and μ (permeability), which constitute the essential parameters determining resonance. As we shall also see in this dissertation, electrical resonance provides a central basis for negative index design as well. Applications related to negative index materials are as follows; high-resolution imaging, non-diffraction limited planar lenses and tunable indices between negative and positive.

1.2 Negative Index Possible Using Metamaterials

The term metamaterials was coined in 1999 by Rodger Walser to describe structured materials having new electromagnetic properties. This came at a time when Pendry [4] had predicted artificial electromagnetic properties using arrays of thin wires and the first papers began to appear showing how "artificial atoms" such as split ring resonator structures, essentially abstracted LCR resonant circuits, could be made in patterned arrays to produce bulk media having these new properties. Their work tied back to a forgotten

but very insightful paper by Pafomov [5] in 1959 and most notably by Veselago published in 1967 [6]. Pafomov was the first to theoretically investigate the idea of a material having both values of permittivity and permeability negative simultaneously before there was any idea about how to make it [5]. Veselago [6] demonstrated mathematically how radiation emanating from a point and propagating into a negative index region in which both permittivity and permeability were negative, could refocus at a point. In other words, a flat slab of a metamaterial with a negative index could image, as was easily seen by invoking Snell's law.

Later on, John Pendry building on Veselago's finding published a theoretical paper in 2000, entitled "Negative Refraction Makes A Perfect Lens."[4] Pendry's new contribution showed how for the very special case of such negative index materials having an index of exactly - 1, even evanescent wave components from an object would be captured and amplified by this material, leading to a so-called "perfect", i.e. non-diffraction limited, image. The point being, both propagating and evanescent waves could contribute to the final image reconstruction. Therefore there might be no physical obstacle to perfect image formation; thereby allowing longer wavelengths to be used to achieve higher resolution than would typically be expected. This conclusion has incentivized thousands of groups around the world to try to make a metamaterial with these properties which to date has not proved successful. Our research (and funding!) diverted me from the study of periodic 1D structures to periodic 2D and 3D structures but now with this goal in mind.

We have used Computer Simulation Technology (CST) to model a number of abstracted resonant circuits that would i) provide the negative permittivity and negative permeability we were seeking and ii) we have systematically assembled them to identify the way in which bulk properties can be realized. A major challenge to achieving a negative index metamaterial is ensuring that an effective medium approximation [7][8] is also valid, i.e. that the discrete circuit elements can be patterned on a sub-wavelength scale to ensure that refraction rather than diffraction dominates the overall bulk properties.

This dissertation is organized into a collection of chapters intended to show the basis upon which the research was conducted. Chapter 2 describes how slow wave structures introduced the insight into metastructure resonant field enhancement. Chapter 3 talks about how resonant field enhancement is applied to negative index metamaterials, while Chapter 4 discusses in detail the theory of metamaterial negative index models. Chapters 5 and 6 experimentally investigate negative index metastructures from an imaging objective beginning with evanescence followed by image resolution, respectively. Chapter 7 describes the final experiments on the negative index metamaterial structure designed and built to possibly demonstrate a sub wavelength planar lens.

CHAPTER 2: SLOW WAVE STRUCTURE

2.1 Field Enhancement Using Periodic Dielectrics

FIGURE 3 represents a periodic stack of N unit cells (each of length L) that exhibit band gaps capable of supporting a DBE (Degenerate Band Edge) [9]. A1 and A2 are 45 degrees misaligned anisotropic layers with in-plane anisotropy, and equal thickness. B is an isotropic layer (e.g. air) and the material choice for A layer is dielectric. Anisotropy provides a mechanism for electromagnetic wave slow down by coupling the allowed polarization states; this introduces a slow wave structure, which can also enhance the field near the band edges.

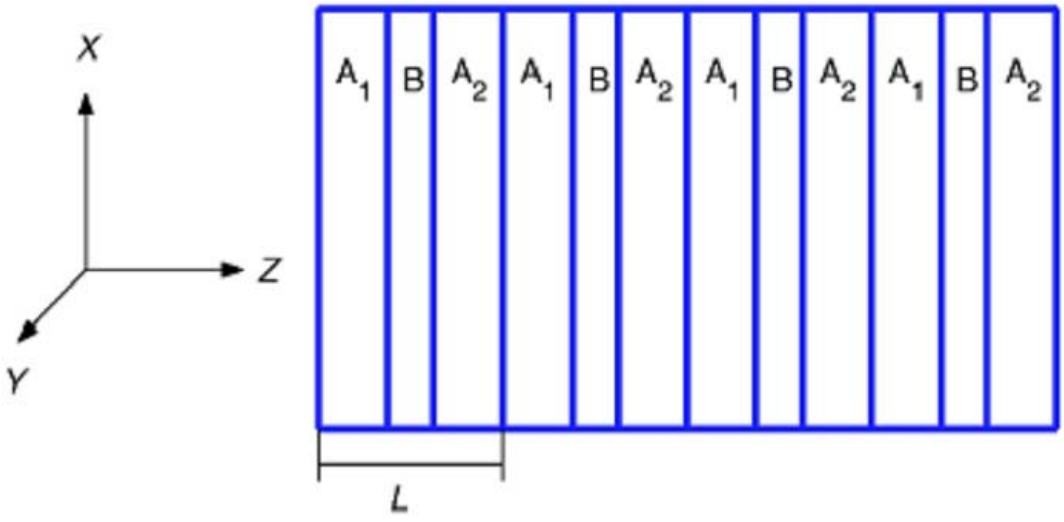

FIGURE 3: Degenerate band edge model Figotin's Theory

The theoretical basis for a slow wave and field enhancing periodic DBE structure

can be described using a transfer matrix method. The analysis of 1D anisotropic photonic crystals employs a four by four matrix, which returns values of the wave vector k for any given frequency [1][9]. Based on the degeneracy of k, the band edge in the dispersion curves shown in FIGURE 4 can be divided into three types. One is the regular band edge (RBE), which has degeneracy of order 2, middle section is the DBE, which has fourth order degeneracy and on the far right is the double band edge or sometimes call split band edge (SBE). Figotin [1] proved that periodic anisotropic dielectric structures could enhance fields as N^4, where N is the total number of periods, which in our experiments was a stack of dielectric disks. In the case of a regular band edge, the field enhancement is proportional to N^2 [1][9]. FIGURE 4 illustrates the different band edge representations. Interpretations of both RBE and DBE are as follows: RBE, one selected point of ω corresponds to two equal real k, while a DBE for one select frequency ω corresponds to four equal real k.

Figotin [1] showed that, approaching the band edge, the group velocity given equation (1) tends to zero and the field is necessarily enhanced. The dispersion diagrams shown in FIGURE 4 illustrate this point.

$$GroupVelocity = \frac{d\omega}{dk} \tag{1}$$

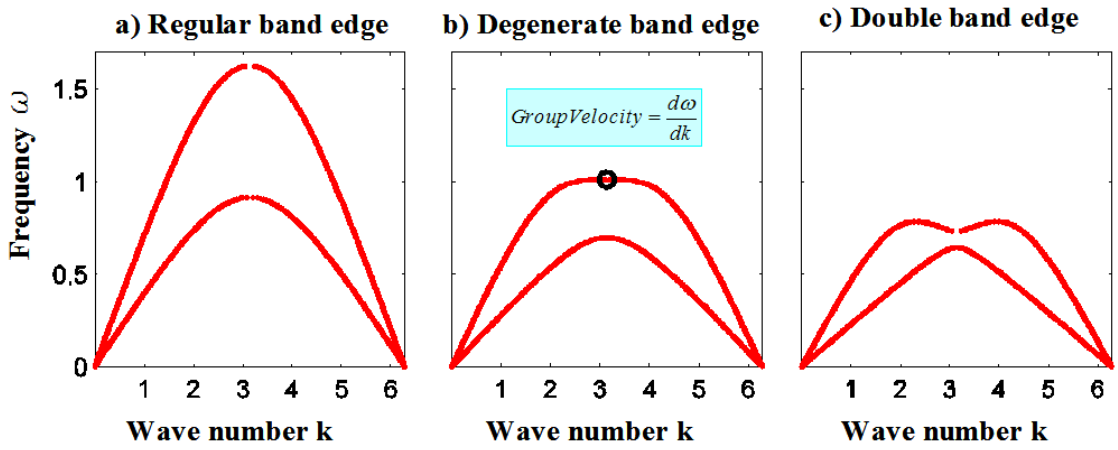

FIGURE 4: Dispersion Diagrams Obtained by Tuning A & B

A "gigantic" [1] transmission band-edge resonance resulting from periodic stacks of anisotropic layers is shown in FIGURE 5, to further understand this idea being discussed, there is an SPIE publication shown in APPENDIX B explaining the theory as well as application. Here it will suffice to briefly mention the salient points of degenerate band edge phenomena.

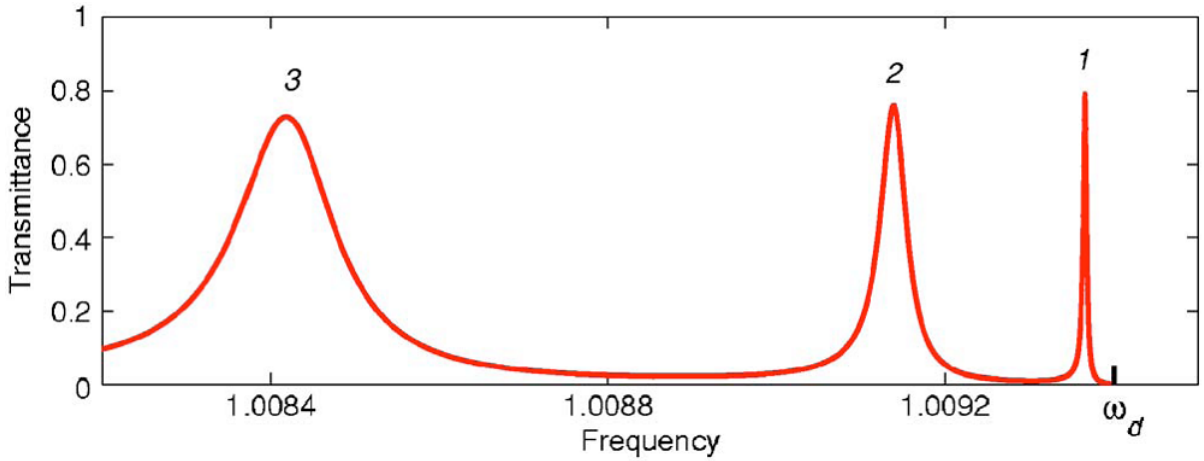

FIGURE 5: DBE frequency ω_D is located to right side of sharp transmission peak ω_d

Dielectric stack of 3 layers per unit cell (of dimension L), which comprise the DBE structure, shown in FIGURE 6 formed the device under test for experimental analysis.

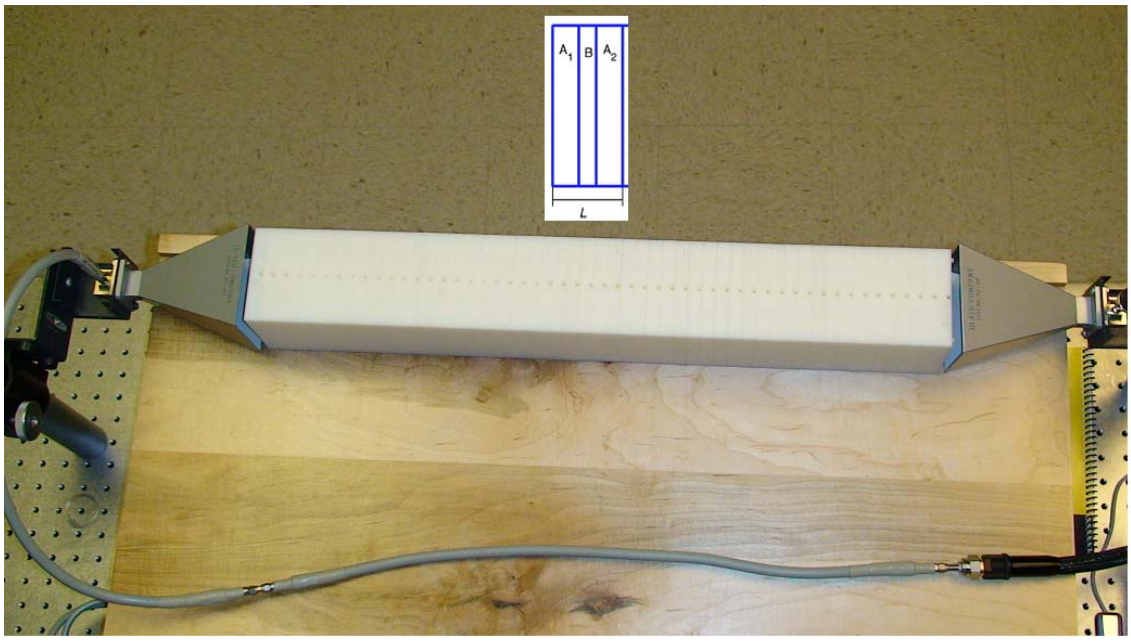

FIGURE 6: DBE structure between a transmitter and receiver antenna

2.2 DBE Transmission Experiment

Experiments were set up to quantify field enhancement and slow down behavior of the DBE structure using microwave generators, and a vector network analyzer along with a wide band spectrum analyzer and horn antennas. Two microwave horns used as transmitter and receiver were configured for maximum sensitivity in the frequency range between 8 and 12 GHz, as seen in FIGURE 6. By inserting the periodic object between the antennas as seen in FIGURE 6 and measuring the scattering (S) parameters, one can estimate transmission, reflection and absorption. These S parameters also provide enough information to extract impedance, which can further help to quantify field enhancements. Another test that was used to analyze the DBE performance was a time domain reflectometer measurement showing both pulse delay and enhancement.

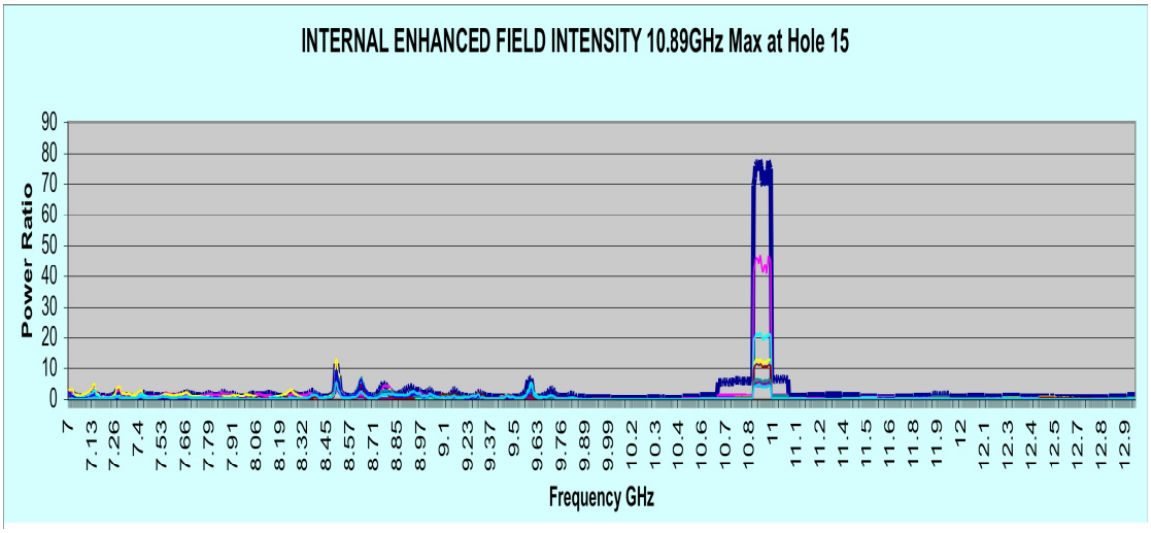

FIGURE 7: DBE experimental results of field measurements at 10.89 GHz.

It's helpful to further understand the detail presented in figure 7. Different colors corresponding to various test hole positions. Magenta color representing the maximum field strength was located at hole number 10, which associates when counting from the left side of the 52-section structure, as approaching central region. Central region is where the field strength is predicted to be gigantic. For complete analysis please refer to APENDIX B.

This result displayed in FIGURE 7, is exactly what was expected by Figotin's theory and a paper was published and this is seen in APPENDIX B [P4]. Although I will not be doing any further work with this DBE structure the knowledge gained will be applied towards negative index metastructures, which is now my central Doctoral Thesis/Dissertation.

CHAPTER 3: NEGATIVE INDEX METAMATERIALS

Understanding negative index metamaterials begins with an introduction to dispersion. When the medium dielectric constant depends on frequency, wave velocity will not be constant as frequency changes; this condition is referred to as dispersion. Dispersion is responsible for different frequencies traveling at different phase velocities. Different velocity could suggest a change in either amplitude or direction or both given the vector nature. The extent to which dispersion exist varies in accordance with resonant absorption, which is the energy absorbed at the systems natural frequency response. When the excitation frequency approaches the medium resonance frequency, the variation of permittivity or index above and below this frequency will typically be optimized. Near this resonance region it's common to observe index shifts into negative values and this behavior is sometimes thought of as anomalous dispersion, which was thought to suggest something abnormal. Today this anomalous behavior can introduce some interesting wave velocity phenomena. Here characteristic impedance will be used to further examine these phenomena given that impedance can efficiently and precisely model materials in space. Characteristic impedance and wave velocity have relationships that can be derived from first principles beginning with the wave equation (2).

$$\nabla^2 \vec{\mathrm{E}}_i + k^2 \vec{\mathrm{E}}_i = 0 \qquad \text{i=x,y,z,} \qquad (2)$$

Where k is the wave number of the medium and is sometimes defined as the spatial frequency that characterizes the variation of the wave in space. Another way in,

which to think about k is by comparison to the number of wavelengths in a distance of $2 \cdot \pi$.

In this case being presented k will be taken to be complex, expressed in equation (3).

$$k = \sqrt{-j\omega\mu(\sigma + j\omega\varepsilon)} \ \left[m^{-1}\right] \tag{3}$$

Here the Electric Field can be assumed an arbitrary polarization along the x-axis propagating in the z direction as described in equation (4).

$$\vec{\mathrm{E}} = \mathrm{E}_x(z)\hat{x} \tag{4}$$

Now a general solution can be assumed as follows in equation (5).

$$\vec{\mathrm{E}}_x(z) = \mathrm{E}^+_{x0} e^{-\gamma z} + \mathrm{E}^-_{x0} e^{+\gamma z} \tag{5}$$

Where E^+_{x0} and E^-_{x0} are complex constants in most general cases and γ is the propagation constant given in equation (6).

$$\gamma = jk = \sqrt{j\omega\mu(\sigma + j\omega\varepsilon)} \tag{6}$$

γ Can also be expressed in rectangular coordinates with a real and imaginary part shown in equation (7).

$$\gamma = \alpha + j\beta \tag{7}$$

Where α and β are typically cast as attenuation and phase constants and can further be expressed as follows. Attenuation constant is expressed in equation (8)

$$\alpha = \mathrm{Re}\left[\sqrt{j\omega\mu(\sigma + j\omega\varepsilon)}\right] \qquad \left[\frac{Np}{m}\right] \qquad (8)$$

And β is expressed in equation (9).

$$\beta = \mathrm{Im}\left[\sqrt{j\omega\mu(\sigma + j\omega\varepsilon)}\right] \qquad \left[m^{-1}\right] \qquad (9)$$

Using equations (6) through (9), equation (5) can now be redefined in the frequency domain shown in equation (10).

$$\vec{\mathrm{E}}_x(z) = \mathrm{E}^+_{x0} e^{-\alpha z} e^{-j\beta z}\hat{x} + \mathrm{E}^-_{x0} e^{\alpha z} e^{j\beta z}\hat{x} \quad (10)$$

To derive the magnetic field the curl of equation (10) is taken and displayed in equation (11).

$$\vec{\mathrm{H}}(z) = \frac{\vec{\nabla}\times\vec{\mathrm{E}}}{-j\omega\mu} = \frac{-1}{j\omega\mu}\frac{\partial}{\partial z}\left[\mathrm{E}^+_{x0} e^{-\gamma z} + \mathrm{E}^-_{x0} e^{+\gamma z}\right]\hat{y} \qquad (11)$$

Simplifying equation (11) results in equation (12).

$$\vec{\mathrm{H}}(z) = \frac{\gamma}{j\omega\mu}\left[\mathrm{E}^+_{x0} e^{-\gamma z} - \mathrm{E}^-_{x0} e^{+\gamma z}\right]\hat{y} \qquad (12)$$

Here is where a substitution can be made using the following variable definition.

$$\eta = \frac{j\omega\mu}{\gamma} = \sqrt{\frac{j\omega\mu}{\sigma + j\omega\varepsilon}} \qquad (13)$$

Equation (13) has defined what is referred to as wave impedance, which is the ratio of the electric field to the magnetic field.

To understand or gauge how fast a wave is traveling can be accomplished by comparison to some standard reference, such as the speed of light in a vacuum. The premise is that the speed of light is the fastest accepted velocity and therefore all other measured values of wave velocity will be considered either less than or equal to. With this basis of comparison comes a ratio between the speed of light to any associated wave phase velocity commonly referred to as the index of refraction seen in equation (14).

$$n = \frac{c}{V_{phase}} \tag{14}$$

Where c is the speed of light and n is the dimensionless index of refraction or velocity gauge. For example, if n=2 then this would be taken too mean that the traveling wave velocity in the specific medium is half as fast as that of light in space. Another way to describe this is that the wave is traveling slower in the specific medium compared to space. In either case what matters is to understand clearly how the specific medium differs from space. Equation (7) can be rewritten with respect to equation (6) as depicted in equation (15).

$$k = \beta - j\alpha \tag{15}$$

This result is taken into account in equation (10) and that clearly shows the only difference between a lossless and non-lossless medium is the decaying exponential α

coefficients along the respective directions of propagation. It is however important to emphasize that in a lossy medium $\beta \approx \omega\sqrt{\mu\varepsilon}$. Phase velocity is defined as follows.

$$V_{phase} \equiv \frac{dz}{dt} = \frac{\omega}{k} \tag{16}$$

Substitute β in equation (16) for k being cautious to remember this is an approximation only. So the phase velocity can be expressed as shown in equation (17).

$$V_{phase} = \frac{\omega}{\omega\sqrt{\mu\varepsilon}} = \frac{1}{\sqrt{\mu\varepsilon}} \tag{17}$$

Both the characteristic impedance and wave phase velocity are expressed in terms of permittivity and permeability. Permittivity and permeability can further be expressed by using indirect association to capacitance (C) and inductance (L) in the following equations (18) and (19).

$$C = \varepsilon \cdot GeometryFactor \tag{18}$$

$$L = \mu \cdot GeometryFactor \tag{19}$$

Where capacitance and inductance will be used interchangeably with permittivity and permeability. Primary reason for this substitution of variables is to begin using circuit analogs, which is the central basis upon which this metamaterial research began. One advantage that circuit analogies offer is quick transformations of material characteristics into well-understood electrical circuit analysis.

Circuit analysis involves impedance, both C and L have independent impedance definitions as follows in equations (20) and (21).

$$Z_C = \frac{1}{j\omega C} \tag{20}$$

$$Z_L = j\omega L \tag{21}$$

3.1 Backward Wave Dispersion Relationship

One other topic for discussion remains before special wave velocity effects can be comprehensively understood. Recall that phase velocity is defined in equation (16), which is essentially a dispersion relationship between the frequency and the wave vector. In a non-dispersive medium a graph of this relationship will show a straight line or a linear corresponding association between frequency and wavelength. In a dispersive medium waves of different frequency will travel at different velocities. This assertion can be demonstrated by using two different frequencies combined or superimposed in some process, which will result in the sum, difference and two original frequencies. For simplicity only the case of the difference and original frequency will be examined here.

Amplitude modulation is one common process of combining two frequencies. It consists of a carrier frequency being adjusted in amplitude at a frequency, which is typically well below the carrier frequency. Mathematically this process can be described as follows in equation (22).

$$E_y(x,t) = 2E_o \cos(\omega_o t - k_o x)\cos(\omega t - kx) \tag{22}$$

Equation (22) is a specific example of a modulated traveling wave in the x direction but to keep this general; this idea is graphically presented in FIGURE 8.

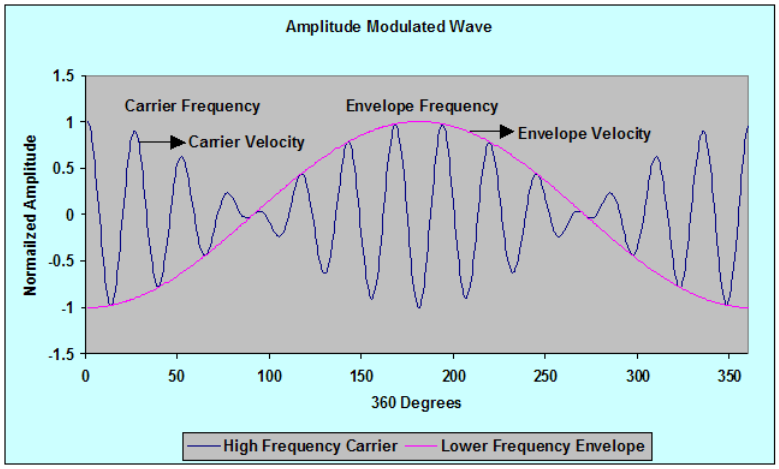

FIGURE 8: Amplitude modulation resulting in more than one frequency

Frequencies of interest will be the carrier and the lower frequency modulation, which is labeled envelope frequency in figure 8.

FIGURE 8 introduces an interesting realization that different frequencies can travel together in a group. Equation (22) will be used to explain this behavior. Deriving phase velocity begins with defining equation (23) the phase of the carrier, which is in the multiplicand of equation (22).

$$\varphi = (\omega t - kx) \tag{23}$$

$$V_{phase} = \frac{d\varphi/dt}{d\varphi/dx} = \frac{\omega}{k} \tag{24}$$

Now keeping in mind that if the medium were not dispersive then there would not be any difference in the velocity of these two frequencies, but it is the dispersive case being examined. So now the phase of the envelope will be calculated, in equation (25).

$$\varphi_{envelope} = (\omega_o t - k_o x) \tag{25}$$

$$V_{group} = \frac{\omega - \omega_o}{k - k_o} = \frac{\Delta\omega}{\Delta k} \tag{26}$$

When the variation above and below the carrier frequency approaches a very small change then equation (26) becomes equation (27).

$$V_{group} = \frac{d\omega}{dk} \tag{27}$$

Equation (27) represents the modulation propagation velocity. Clearly this dispersion relation between ω and k does not produce a straight line. Group velocity is typically associated with energy velocity, which corresponds to the transport of power in the direction of propagation. There is a product relationship between the group velocity, phase velocity and the speed of light as shown in equation (28).

$$c^2 = V_P \cdot V_G \tag{28}$$

This relationship is widely accepted and is considered to always hold true. For example if the group velocity is considered to be less than or equal to the speed of light then in some circumstances this implies that the phase velocity can be greater than the speed of light. This does not violate any law given that the phase velocity is not associated with the energy velocity. At this point it becomes apparent that the phase velocity can be different in amplitude or sign compared to the group velocity given a dispersive medium. There is also the case where the phase velocity can be opposite the direction of the group velocity. This backward phase wave phenomena can exist within certain types of dispersive media.

Within anomalous dispersion regions waves can have phase velocity and group velocity with opposite signs. Negative index metamaterials can exhibit both backward wave phenomena and negative refraction as will be seen in the sections that follow.

Backward wave phase velocity can be expressed by first beginning with a dispersion relation.

Equation (6) has a general dispersion relation, which can be substituted with another equivalent representation derived from a circuit analog. Think about the circuit analog as another way to envision material characteristics and their relationship to electromagnetic wave phenomena. One circuit that could be used to illustrate backward wave phenomena is seen in FIGURE 9.

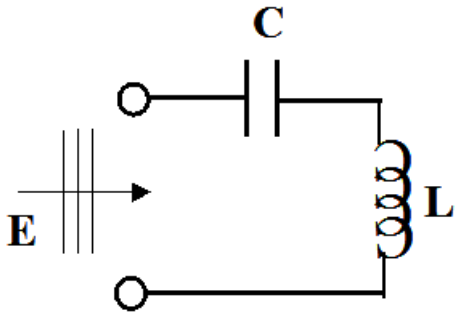

FIGURE 9: Series shunt resonant circuit

FIGURE 9 has a dispersion relation equivalent to $\sqrt{Z \cdot Y}$ where Y is defined as the shunt inductive impedance or admittance, the reciprocal of impedance and Z in this case is the series capacitive impedance looking in from the left. At first it simply appears that this product root is 1, but this is somewhat misleading, the salient point is that under specific conditions given the product root represents two different impedances. Equation (6) can now be written in terms of L and C shown in equation (29).

$$\gamma = jk = \left[\frac{-1}{\omega^2 \cdot C \cdot L}\right]^{\frac{1}{2}} \qquad (29)$$

Equation (29) is one of many ways in, which to represent total capacitive and inductive impedance relationship, the concept being employed is circuit equivalence.

This idea demonstrates more than one circuit topology will result in identical impedances. The choice of which circuit is based on the desired dispersive characteristic response. There are two fundamental circuit topologies that underlie all topological constructs of L and C. First is a series combination, which is two components, having one common node and no other element is connected to that node. Second is the parallel configuration, one terminal of each element is connected to a common node and the other terminal of each element is connected to the other common node. These definitions form the entire basis of approach in synthesizing a specific model response. From the ideal model being exhibited with a negative index, a similar dispersion relation was derived using the principles described and the result is presented in FIGURE 10.

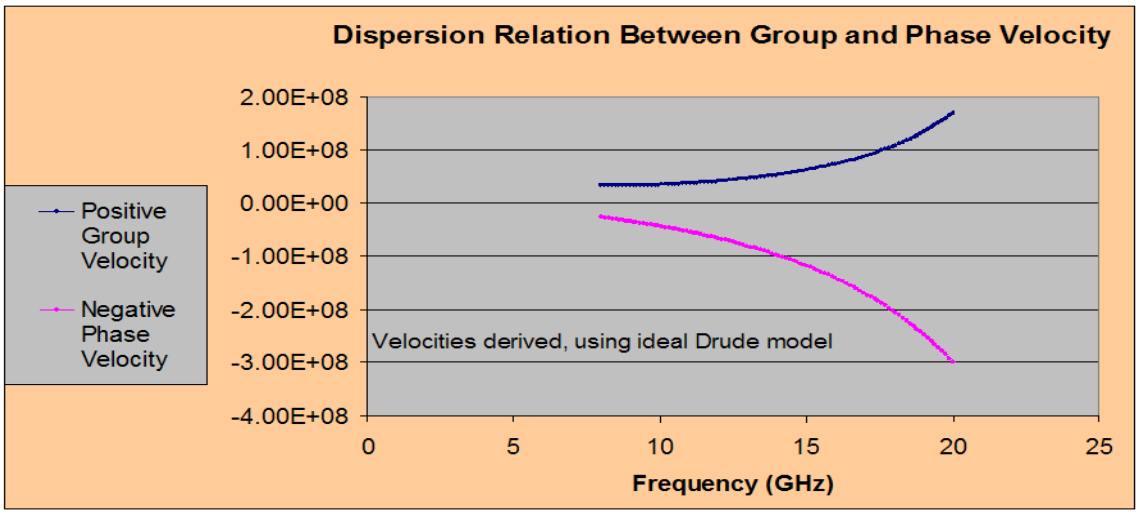

FIGURE 10: Dispersion relation dictates phase and group velocities

From equation (29) and FIGURE 10 the following results were also derived in equations (30) and (31). These expressions clearly show the difference in signs, which are required to demonstrate backward wave phenomena.

$$V_P = \frac{\omega}{k} = -\omega^2 \cdot \sqrt{C \cdot L} \qquad (30)$$

$$V_G = \frac{d\omega}{dk} = \omega^2 \cdot \sqrt{C \cdot L} \tag{31}$$

Negative phase velocity indirectly relates to negative index from equation (14) and impedance relates to negative index by capacitance and inductance materials. Before continuing on it is important to capture three essential salient points. First being, frequency dependent effective dielectric constant, relates to capacitance. Second point, effective permeability relates to inductance. Resonant frequency can be approximated as shown in equation (32).

$$f_o = \frac{1}{\sqrt{L \cdot C}} \tag{32}$$

Negative index materials present a new class of artificial materials, also typically periodic with a subwavelength period that can be best categorized using four cases of refraction based on Snell's Law. The point is to track the point of entry of a beam (or wave front normal (i.e. wavevector) compared to its point of emergence for these four possible cases of refraction within a slab of finite thickness. Case I, shown in FIGURE 11 below, illustrates an incident ray portrayed (see FIGURE 11) as it enters a region where the index of refraction is equal to the surrounding medium and therefore it undergoes a straight-line transmission projection throughout. Case II, when the slab medium has a positive index greater than one, then Snell's Law shows a departure from straight-line projection that appears to bend toward the normal, as expected. Here is a situation; a path between entry and exit points, which is displaced by an amount easily, determined using Snell's Law. Case III, the slab's index is negative and ray bending continues passing through the normal, as seen in FIGURE 11. Case IV, shows the

special case of an index of negative one and again the same reasoning applies. These negative and less-than-unity index values are potentially very useful, but, as we will show, are somewhat challenging to accomplish experimentally at microwave frequencies.

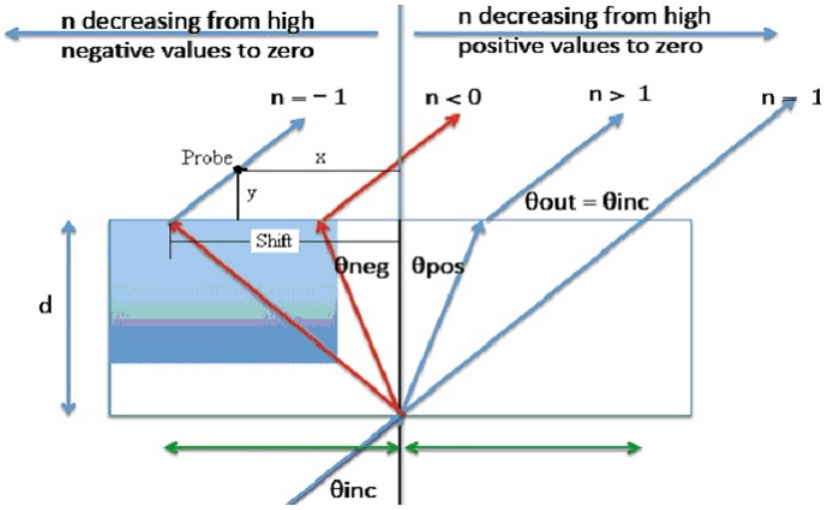

FIGURE 11: Four cases of refraction based on Snell's Law

FIGURE 12 is a simulation of the negative refraction Case III using an idealized material model based on the Drude conductivity and it was designed using CST in the microwave X-band, which is categorized as (8 – 12 GHz).

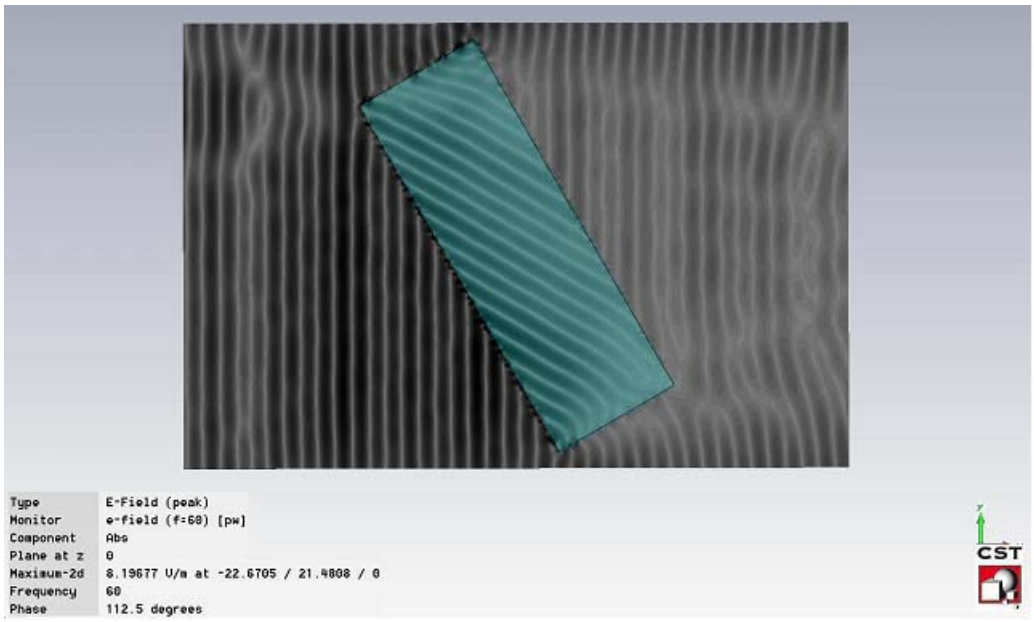

FIGURE 12: Plane wave entering and exiting from negative index medium

3.2 Negative Index Planar Lens

It's important to remember that Case III represents negative index metamaterials that exhibit a backward wave or negative phase velocity phenomenon and case IV is the basis upon which light can be focused to a point as seen below in FIGURE 13. This display of a planar medium demonstrating how light can be focused from a point source to an image is also a demonstration of a simple slab or "planar" lens. There is one special case of interest representing a possible non-diffraction limited planar lens giving the possibility of very high-resolution imaging.

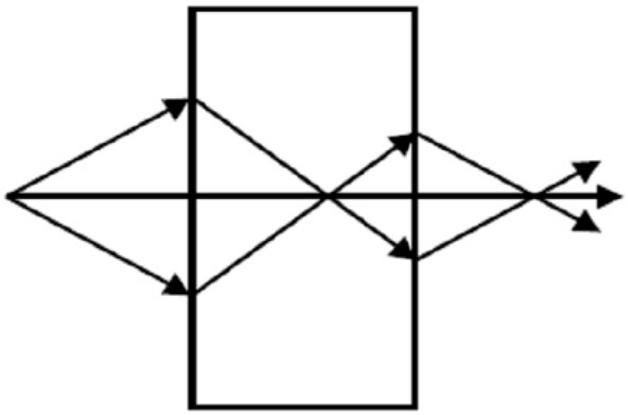

FIGURE 13: Negative refraction focuses light

A negative refractive index medium bends light to negative angle with respect to the surface normal. Light formerly diverging from a point source, depicted on the left side of the medium, converges back to a point within the negative index slab (if it is sufficiently wide) and again in an image plane behind the slab as shown above. This behavior, described in reference to FIGURE 13, was first introduced by Veselago [6].

The paper that is today considered to define the birth of metamaterials was written by Veselago [6], in which he just speculated about whether a negative index was a physically meaningful concept but he did not introduce or propose structures or metamaterials having those properties; that followed later. The important observation made by Veselago was that simultaneous negative permittivity and permeability in a material will support a propagating wave.

Achieving a negative index begins with understanding how both the real parts of permittivity and permeability can be less than zero simultaneously over a common frequency interval. It does not matter that the magnitudes be equal, only that they both are less than zero simultaneously over this interval.

Using electrical circuit theory to satisfy the above-mentioned criteria is one accepted way of investigating this possibility. Though circuits involve nodal and loop analysis, which is not descriptive of an object in space, they can be cast as black box impedances, which forms the underlying basis of design. Impedances can be used to represent material characteristics such as permittivity and permeability. Impedances also can be functions of frequency and geometry, which is exactly how various proposed metastructures, behaves, as abstracted resonant circuits. We have developed further, one particular configuration first introduced by Kong et al [10], using geometry and special resonant effects. So applying both circuit and antenna theory to an impedance model of some geometry and material does lead to a quantifiable method of yielding a desired ε and μ. It is important to keep in mind that this procedure results in an effective index but not necessarily an effective medium, which will be needed to affect a homogeneous or uniform distribution.

When the wavelength inside a periodically structured metamaterial becomes comparable to or smaller than the unit cell period of the metastructure its description as a uniform homogeneous effective medium [7] breaks down. Effective medium approximations are analytical models that attempt to describe the macroscopic properties of a medium based on the properties and the relative fractions of its components. Among the numerous effective medium approximations, Bruggeman's symmetrical theory [11] is used here as one that is widely accepted. Effective-medium approximations (EMA) are applied in the theory of inhomogeneous materials and was first proposed by Bruggeman [11], and then, in a different context, by Landauer [12]. These approximations have been the basis for studies of macroscopically inhomogeneous media, and have been

generalized by many authors to treat a wide variety of problems. As increasingly shrinking abstracted circuit structures comprising composite metamaterials are developed, the EMA will become even more important in predicting the bulk structure's performance.

Electromagnetic metamaterials are broadly defined as artificially effective homogeneous structures having properties not readily observable in nature. An effectively homogeneous structure is a structure whose structural average cell size is much smaller than the guided wavelength. Therefore, this average cell size should be as small as possible and a rule of thumb should be less than a tenth of a wavelength. This is challenging from a fabrication perspective, especially for optical metamaterials and we show that at least smaller than a quarter of wavelength will suffice for many purposes. This limit or effective-homogeneity condition ensures that refractive behavior from the metamaterial will dominate over scattering/diffraction effects when a wave propagates inside the meta medium. If the condition of effective-homogeneity is satisfied, the structure behaves as a real material in the sense that electromagnetic waves are essentially myopic to the lattice and only are primarily influenced by the effective well-defined constitutive parameters, which depend on the nature of the unit cell. The constitutive parameters are the permittivity ε and the permeability μ can be tensors and these define the refractive index.

We note that the DBE structure we described previously was composed of form birefringent elements to establish the anisotropy needed to realize the DBE enhanced resonance. This material characteristic property is based on sub-wavelength grating

structures that also need to satisfy the effective medium theory. The earlier work exploring the DBE effect was thus a metamaterial study as well.

Our interest is driven not only by producing a negative index metamaterial but if at all possible, a negative index of exactly -1, which will be a big step toward reaching the ideal perfect lens, according to Pendry [4]. Veselago showed that electromagnetic rays emanating from a point into a negative index slab (i.e. having both the permittivity and permeability negative simultaneously) can focus that light. Pendry extended this theory in his paper "Negative Refraction Makes a Perfect Lens"[4]. His contribution was that evanescent waves (i.e. normally non-propagating high spatial frequency components) are also enhanced through the transmission process within a slab having a negative index of unity as can be seen in FIGURE 14. The blue curve illustrates conceptually the amplification of a specific high spatial frequency that is evanescent. This component contributing to the sub-wavelength spatial resolution of a scatterer in the object plane is in principle perfectly reproduced in the image plane, allowing those sub-wavelength features to be recovered.

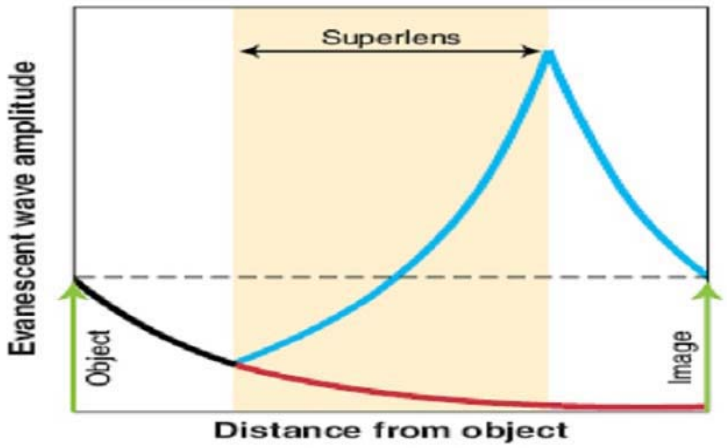

FIGURE 14: The principle of evanescent wave refocusing

3.3 Negative Refraction Makes a Perfect Lens

Pendry's theory describes a transfer function for this n = -1 slab showing that the exponentially decaying wave from the object on the left grows exponentially within the planar negative-index lens, (blue curve). On the other side of the lens, it decays again until it has reached its original value at the image plane. These components of the object are lost in the absence of the negative index lens, (red curve).

We want to test his claim perfect image reconstruction without any diffraction limit is possible. There are two very important facts to keep in mind with this claim. Both an index of –1 and relatively low losses are required for evanescent wave transmission and amplification for such a lens to be perfect. This leads to the possibility that a planar lens will produce sub-wavelength focusing, which means, low illuminating frequencies such as microwaves could image with higher resolution than currently realized in practice. Investigating the possibility of designing and making a perfect planar lens that can image without or with reduced resolution-limiting diffraction effects, became the goal of this research.

3.4 Pendry's Split Ring Resonator Model

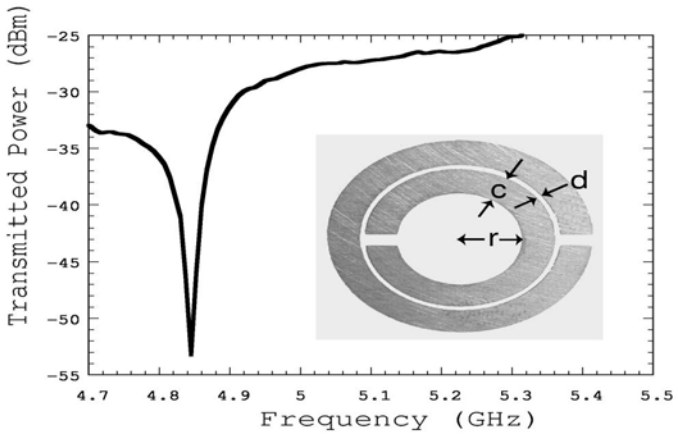

FIGURE 15: Pendry's split ring resonator model for producing a –1 index

Numerical analysis is required to obtain the correct response for any choice of abstracted LCR circuit we might want to investigate as a component of a negative index metamaterial. What matters here is to understand how the circuit model can affect simultaneously both permittivity and permeability being less than zero. Pendry's model as seen here in FIGURE 15 and in reference [13], which is entitled "Composite Medium with Simultaneously Negative Permeability and Permittivity ", provides one specific example to accomplish this task. The metamaterial medium discussed by Smith [13], composed of some construct of split ring resonators were initially used to study microwave propagation through the ionosphere, which exhibited a negative permittivity below the plasma frequency. So if the permeability could also be simultaneously in a negative region then a negative index metamaterial would result. At resonance, the model has an enhanced response, which resulted in observing a negative permeability. Below the resonant frequency, the permeability was positive and above, it was negative. Working backwards with this resonance result lead to the required constituent values of geometry and material properties from which a bulk material could be assembled. This design to produce a negative index material by using circular split rings was modified by Kong at MIT. Kong's design evolved from this split ring resonator model by Pendry and after much research was adopted by us as the most promising elemental structure from which to proceed.

3.5 Kong's S Split Ring Resonator

Kong and Chen exploring negative index properties [10][14][15][16] began first by attempting to verify negative refraction using an electrical design shown in FIGURE 16

that relates to micro-strip circuit theory. The results were conclusive that one could in fact achieve a negative index by using the appropriate mix of metal and dielectric materials. They demonstrated this behavior over a wide bandwidth shown in FIGURE (22). Using transmission line theory in conjunction with free space characterization, Kong and Chen formed a patterned metal S strip on both sides of a dielectric circuit board with the intention to characterize the effective impedance and refractive index by direct experimental measurement of transmission and reflection coefficients resulting from the model shown in FIGURE 16. By using this method they obtained both the index and impedance, which then could be related to the index by using equations (33) and (34), which come from the relationship between E and H fields.

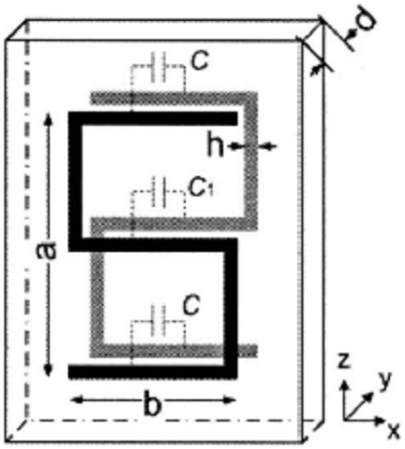

FIGURE 16: Kong's original S model

$$\varepsilon_{eff} = \frac{n_{eff}}{Z_{wave}} \tag{33}$$

$$\mu_{eff} = n_{eff} \cdot Z_{wave} \tag{34}$$

$$n_{eff} = \pm\left(\varepsilon_{eff} \cdot \mu_{eff}\right)^{\frac{1}{2}} \tag{35}$$

Equation (35) was obtained indirectly through power density measurements as a function of frequency in the far field at specific angles from the experimental S model. As reported the reflection and transmission coefficients were obtained and used with free space impedance to calculate the effective wave impedance. These power measurements were used to estimate the dominant track of emerging energy, this result when worked backwards through the existing geometry would approximate a refractive index. Once all the data was collected and plotted, the results revealed a negative index region shown in FIGURE 22. The fact that the metal strips were placed on a circuit board in exactly the same way most circuits are formed in microwave design lends itself to analysis by well-understood circuit analysis of both micro strip and antenna theory. In a 2005 paper published by Kong [16], the following theoretically derived and closed form solutions required in the design of a negative index metamaterial based on the S pattern are presented below.

3.6 Overview Of Kong's Actual S Patterned Model Structure

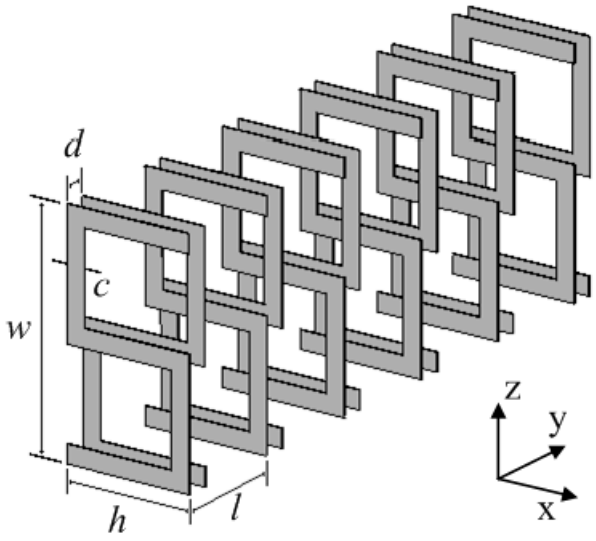

FIGURE 17: Three-dimensional plot of S shaped resonator

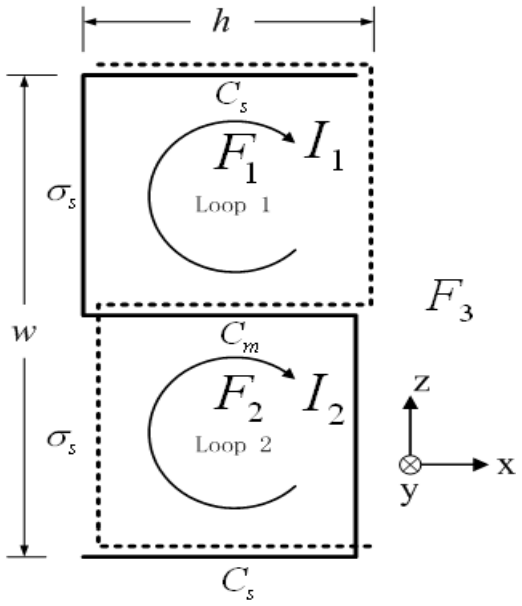

FIGURE 18: Two-dimensional view of S shaped resonator

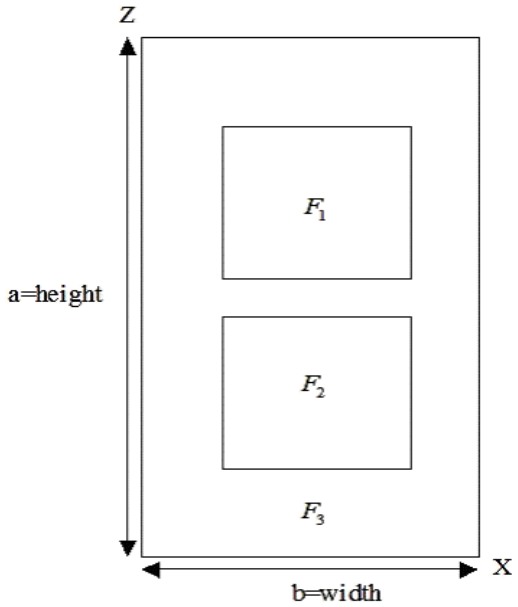

FIGURE 19: Fractional area depictions

Beginning with FIGURE 17, the physical dimensions are shown along the respective axes that represent the patterned S height (w), width (h), line width (c) front to back pattern spacing (d) and period (l). FIGURE 18, represents two imaginary clock wise loops of current I1 and I2 circulating in the upper and lower areas of the S pattern. Also

shown is the C_m (mutual capacitance between the center metallic strips) and C_S (series capacitance in the top and bottom metallic strips). Fractional area depiction shown in FIGURE 19 is intended to be a general perspective of unit cell volume occupancy, designated as F_1 (upper fractional volume), F_2 (lower fractional volume) and finally F_3 (surrounding fractional volume). The frontal two-dimensional area displayed in FIGURE 19 is described as the product of the unit volume height (a) and unit volume width (b) that will be referred to as the unit area S.

3.7 Kong's Closed Form Solutions

With these definitions one can write the generalized fractional volume equation:

$$F_1 + F_2 + F_3 = 1 \tag{36}$$

When a time-varying external field H_0 is applied in the y direction, currents will flow in the split ring, denoted by I1 and I2 shown in FIGURE 15. The induced currents, result in three magnetic fields H1, H2 and H3 in the corresponding fractional volumes. One point that needs to be made clear is that these induced currents represents total current. Here is where Maxwell's equation for total current must be satisfied. Using loop analysis the following equations result.

$$\mathrm{H}_1 - \mathrm{H}_2 = J_1 - J_2 \tag{37}$$

$$\mathrm{H}_1 - \mathrm{H}_3 = J_1 \tag{38}$$

$$\mathrm{H}_1 \cdot F_1 + \mathrm{H}_2 \cdot F_2 + \mathrm{H}_3 \cdot F_3 = \mathrm{H}_0 \tag{39}$$

$$J_1 = \mathrm{I}_1 / l \tag{40}$$

$$J_2 = \mathrm{I}_2 / l \tag{41}$$

From the requirements of equations (36) through (39) and the definitions of (40) and (41), the individual magnetic fields can now be calculated.

$$\mathrm{H}_1 = \mathrm{H}_0 + (1 - F_1) \cdot J_1 - F_2 \cdot J_2 \qquad (42)$$

$$\mathrm{H}_2 = \mathrm{H}_0 - F_1 \cdot J_1 + (1 - F_2) \cdot J_2 \qquad (43)$$

$$\mathrm{H}_3 = \mathrm{H}_0 - F_1 \cdot J_1 - F_2 \cdot J_2 \qquad (44)$$

Before continuing with this derivation it will be helpful to understand the required conditions for equations (39) through (44) to be valid. The point being made here is the basis upon which I designed a new modified Kong's model to affect a backward wave phenomenon, having established that the present design would not have demonstrated the required characteristics. Given the premise that the separable spacing between the front and back patterned metal is sufficiently reduced along the y direction, then the magnetic fringing can be neglected. On closely examining this premise, it becomes evident that the closer the spacing, the larger will be the resulting permittivity. This association is unavoidable given the realization of the magnetic fringing effect being dominant in the event of greater separable distance along y. After further examination of equations (39) through (44), it also becomes evident that there is field cancellation between the center metallic strips, due to the opposing current directions. This follows because the backside metal pattern is a simple mirror image of the front. With these observations in mind it was decided to remove the backside metal pattern all together and simply form a unit cell by the combination of two same oriented patterns again separated along y. This modified design change allowed the permittivity to become closer in magnitude to the permeability

thus allowing for a design with both a negative index that is also closer to unity. There are two additional steps before the required capacitance and inductance can be calculated. First is the electromotive force around each loop.

$$emf1 = -\frac{\partial}{\partial t}(\mu_0 \mathrm{H}_1 F_1 S) \tag{45}$$

$$emf1 = \sigma_S \mathrm{I}_1 + \frac{1}{C_S}\int \mathrm{I}_1 dt + \frac{1}{C_m}\int (\mathrm{I}_1 + \mathrm{I}_2)dt \tag{46}$$

$$emf2 = -\frac{\partial}{\partial t}(\mu_0 \mathrm{H}_2 F_2 S) \tag{47}$$

$$emf2 = \sigma_S \mathrm{I}_2 + \frac{1}{C_S}\int \mathrm{I}_2 dt + \frac{1}{C_m}\int (\mathrm{I}_1 + \mathrm{I}_2)dt \tag{48}$$

The contribution of σ_S, quantifies the metallic resistance of the strips.

$$C_S = C_m = \varepsilon_0 \cdot \frac{hc}{d} \tag{49}$$

In equation (49) the capacitance represents an air dielectric and when the dielectric is different it can be represented as follows.

$$C_S = C_m = \varepsilon_0 \varepsilon_r \cdot \frac{hc}{d} \tag{50}$$

The last step toward deriving the permeability is made with a replacement of time derivatives and integrals based on the assumption of harmonic time dependencies that will allow equations (46) and (48) to become equations (51) and (52).

$$i\omega\mu_0 \mathrm{H}_1 F_1 S - \sigma_S J_1 l + \frac{J_1 l}{i\omega C_S} + \frac{(J_1 + J_2)l}{i\omega C_m} = 0 \tag{51}$$

$$i\omega\mu_0 \mathrm{H}_2 F_2 S - \sigma_S J_2 l + \frac{J_2 l}{i\omega C_S} + \frac{(J_1 + J_2)l}{i\omega C_m} = 0 \tag{52}$$

Applying equations (40) and (41), which represent J_1 and J_2 now allows one to determine the permeability:

$$\mu_{eff} = 1 - \frac{(\omega\mu_0 S)^2 F_2 F_1 (F_1 + F_2) - \mu_0 S\left[(F_1^{\,2} + F_2^{\,2}) \cdot \frac{1}{C_S} + (F_1 - F_2)^2 \cdot \frac{l}{C_m} \right] + iA(\sigma)}{(\omega\mu_0 S)^2 F_1 F_2 - \mu_0 S(F_1 + F_2)(\frac{l}{C_S} + \frac{l}{C_m}) + \frac{1}{\varpi^2}\frac{l}{C_S}(\frac{l}{C_S} + \frac{2 \cdot l}{C_m}) - \mathrm{B}(\sigma) + iC(\sigma)} \tag{53}$$

$$A(\sigma) = \omega\mu_0 S(F_1^{\,2} + F_2^{\,2})\sigma_S l \tag{54}$$

$$B(\sigma) = (\sigma_S l)^2 \tag{55}$$

$$C(\sigma) = \left[\omega\mu_0 S(F_1 + F_2) - \frac{2}{\omega}(\frac{l}{C_S} + \frac{l}{C_m}) \right](\sigma_S l) \tag{56}$$

Calculating the resonant frequency would require two equations if F_1 and F_2 were different, but in our case symmetry was used to aid the resulting backward wave and negative index requiring $F_1 = F_2$. This condition can further simplify the math by inspection.

$$\omega_{m0}^{1} = \sqrt{\frac{(m+1)(p+1) + \sqrt{(m-1)^2(p^2 + 2p) + (m+1)^2}}{2mp} \frac{l}{\mu_0 S F_1 C_S}} \tag{57}$$

$$m = \frac{F_1}{F_2} \tag{58}$$

$$p^{'} = \frac{C_m}{C_s} \tag{59}$$

In addition to the double magnetic resonance for the case where $F_1 \neq F_2$ it can also be shown hereafter that the S-shaped resonator also exhibits an electrical plasma behavior, which overlaps with the two magnetic resonance's but in our case, one overlap. This is the primary point to realize when attempting a negative index metamaterial.

The conclusion in this paper makes it clear that this particular modified S-split ring resonator demonstrates a plasma behavior for both magnetic and electric fields. Two more equations will now be introduced to quantify the plasma behavior.

$$\omega_{mp} = \sqrt{\frac{1}{\mu_0 FS(1-2F)}\left(\frac{1}{C_S} + \frac{2l}{C_m}\right)} = \omega_{m0}\sqrt{\frac{1}{(1-2F)}} \tag{60}$$

Here is a similar plasma expression for the electric permittivity again made possible by Kong's modified S-split ring resonator.

$$\varepsilon_{eff} = 1 - \frac{\omega_{\varepsilon p}^2 - \omega_{\varepsilon 0}^2}{\omega^2 - \omega_{\varepsilon 0}^2 + i\gamma\omega} \tag{61}$$

The choice of this S shape simplifies the task of impedance quantification in comparison to other designs, such as rings or curved forms. Capacitance and inductance become standard expressions for this choice of geometry as follows.

$$L = \mu_o \cdot \frac{FS}{l} \tag{62}$$

Equation (62) is derived by taking the inductance per unit length enclosed by the loop areas shown in FIGURE 18 as opposed to the capacitance per unit length.

$$L = \mu_o \cdot \frac{SLength \cdot SHeight}{2} \tag{63}$$

$$C = \varepsilon_o \cdot \frac{Area}{BoardThickness} \tag{64}$$

With the above-calculated parameters in equation (63) and equation (64) we can approximately calculate the resonant frequency shown in equation (65).

$$f_o = \frac{1}{\sqrt{L \cdot C}} \tag{65}$$

The above mathematical model forms the basis of their microwave design and is commonly used in many other microwave strip line designs. From this basic circuit theory came the built model seen in FIGURE 20. As can be seen from the figure below, there is a stack of double sided copper S patterned circuit boards arranged as a prism configuration.

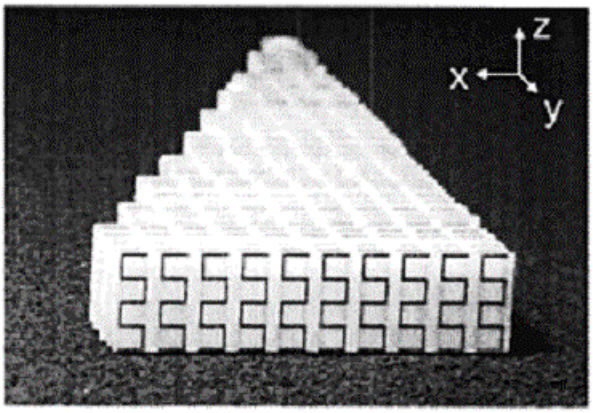

FIGURE 20: Kong's Experimental Prism Meta Structure

Kong's experimental setup, shown in FIGURE 21, uses this metastructure in the following way. Incident light is normal to the non angled surface and the emerging refracted ray is measured for a large number of angles at various distances around the

output area as shown below to map out the transmission projection, which indirectly will be used to help decide the range of index values.

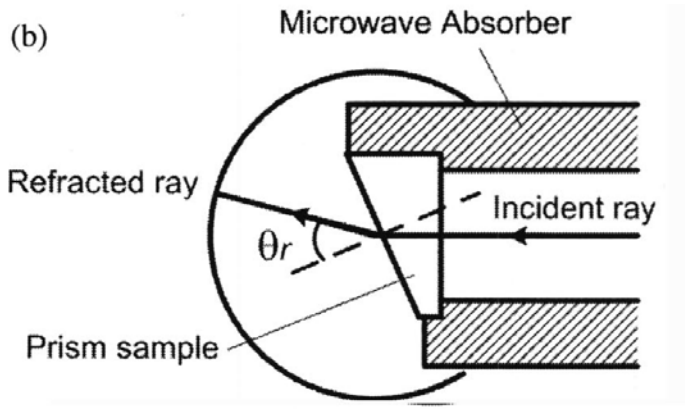

FIGURE 21: Kong's Experimental Setup

Plotted results of this experimental data are shown in FIGURE 22.

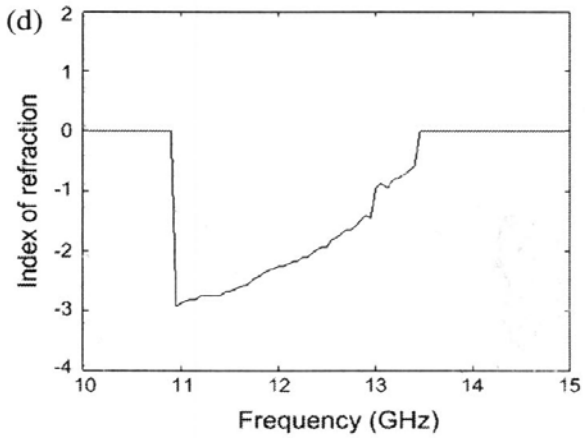

FIGURE 22: Kong's Negative Index of Refraction Response

The above FIGURE 22 represents experimental data confirming a negative index over approximately 2.5 GHz bandwidth between 11 and 13.5 GHz. It was from this experimental result that their model was verified to produce a negative index of refraction. After realizing the simplicity of their design and for the reasons stated above, we adopted this as a candidate for our metamaterial imaging research. There are several

aspects to the design that have been changed to support our specific imaging goals. These changes resulted in more flexibility in obtaining a backward wave as will be seen in the experimental results.

Recently, there have been advances in establishing better criteria for defining effective media [17]. This paper provided a descriptive explanation of the electromagnetic behavior of metamaterials based on a general theory of effective media, from which the effective parameters are derived in terms of average permittivity and permeability. According to their derivations, they could justify the validity of an effective medium theory for both homogeneous media and metamaterials. Their approach is in part based on the Drude conductivity model and this compliments the knowledge gained during the early investigation of how best to affect a negative index, which was also based on the Drude conductivity model, but from a different perspective. This was the primary reason to use this reference so that further insight could be gained into the applied use of the Drude conductivity model. This model is central to this dissertation and therefore any references that relate either directly or indirectly will be considered helpful.

CHAPTER 4: METASTRUCTURES' THEORY AND MODELS

In the section that follows, there are illustrations, Figures 23 through 28, of the meta structures we have modeled and fabricated, to provide additional insight about how the actual physical structures' properties and observe behavior in experiments, compare to the simulations obtained using Computer Simulation Technology (CST). These results do make clear that the simulation tool we are using and practical structures are consistent.

Figures 25 and 26 emphasize the fact that the actual experimental data, acquired several times, consistently agrees with CST in respect to the designed peak resonance for this metamaterial at 10 GHz as well as the resonance frequency profile as well. Between 14 and 15 GHz there is an exaggerated amplitude response from CST, though similar in shape, and this is believed to be caused in part to the actual permittivity of the board being lower than the simulated value. The effect of a lower permittivity would be seen in the higher end of the frequency response in conjunction with some distributed inductance. Other than that these diagrams indicate excellent consistency, thereby giving confidence in our ability to model new metamaterial structure designed to have the properties we require and the expectation that the associated fabricated structures will behave accordingly.

Not only did our experiments instill a higher confidence in the predictive capability of CST, but also the circuit response calculated using Mathcad and simulated by Spice as well both agree with CST simulation results.

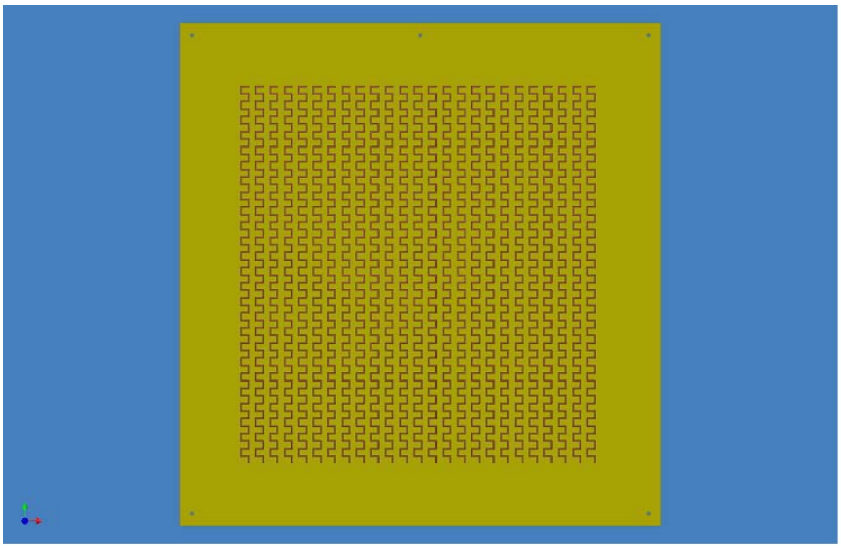

FIGURE 23: Two-sided designs: based on Kong's S pattern [10]

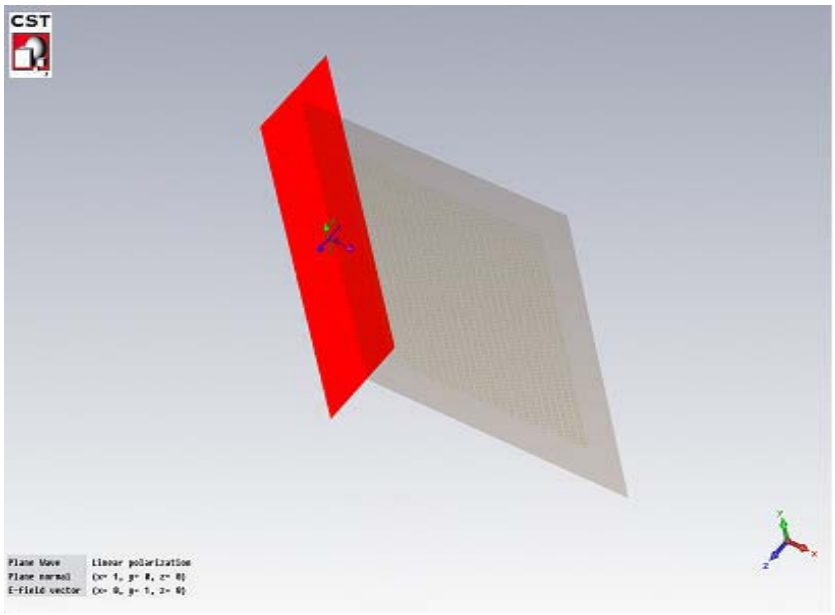

FIGURE 24: Plane wave illumination (red wavefront) incident along the edge

FIGURE 24 also shows the E field (green) and H field (blue) orientation. The board is illuminated from the edge rather than the flat surface and this is the orientation in which all simulations will be carried out here and later.

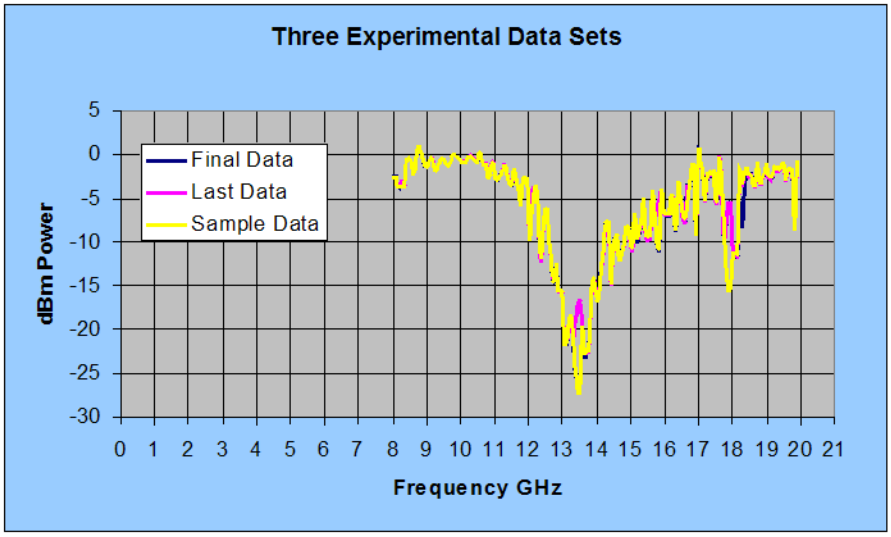

FIGURE 25: Three experimental measured transmission responses from 8 to 12 GHz

These transmission spectrum results were obtained from three consecutive measurements. The differences between these experimental measurements involved varying locations of input and output probe coordinates to show that the response was independent of location.

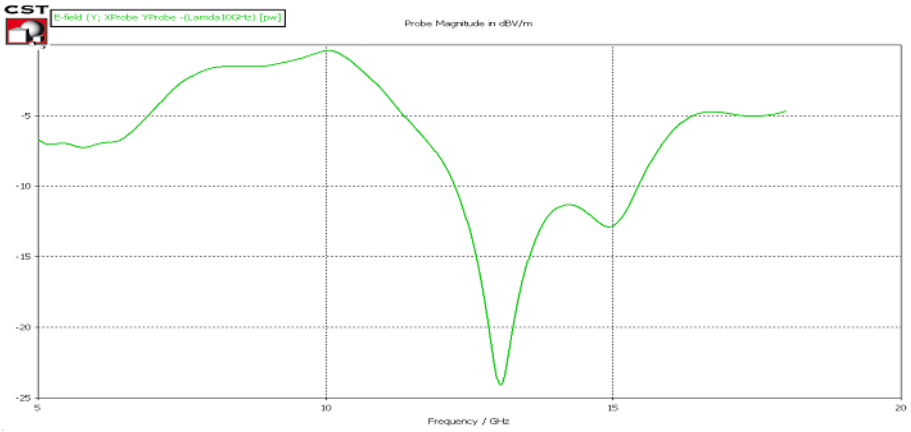

FIGURE 26: Simulated Transmission Results 5 to 20 GHz

It is important to note the good consistency between the simulated data above in FIGURE 26 and the measured data plotted in FIGURE 25.

4.1 Basic Theory of New Model Design

As explained, Kong and Chen's 2004 paper provided a useful theoretical basis upon which to begin our first attempts at metamaterial design [10]. Smith's paper [13], which was the first to build and test the split ring resonators (SRR) also provided important practical information. Having a passive material or composite structure in space illuminated by a plane wave excitation represents an excitation incident on an impedance structure. Impedance is obviously a frequency sensitive characteristic response to an energy stimulus, and as stated earlier, impedance can be represented by some combination of resistance, inductance and capacitance. Maxwell's equations (66) and (67) along with constitutive relations can be expressed as follows.

$$\nabla \times \vec{E} = -\frac{\partial \vec{B}}{\partial t} \tag{66}$$

$$\vec{D} = \hat{\varepsilon}\,\vec{E} \tag{67}$$

$$\vec{J} = \sigma \vec{E} \tag{68}$$

$$\vec{B} = \mu \vec{H} \tag{69}$$

Material relations shown in Equations (67), (68) and (69) directly relate to, capacitance (C), resistance (R), and inductance (L), and, the constant, "Constant", is any numerical scaling factor.

$$\vec{L} = \mu \times \text{Constant} \tag{70}$$

$$C = \varepsilon \times \text{Constant} \tag{71}$$

$$R = \sigma^{-1} \times \text{Constant} \tag{72}$$

Applying Maxwell's equations with these relations yields the following results that quantify impedance (Z) shown in equations (73) and (74), in terms of E and H as well as permeability (μ) and permittivity (ε), when harmonic time dependence is assumed.

$$Z = \frac{E}{H} \tag{73}$$

$$Z = \left[\frac{\mu}{\varepsilon}\right]^{-\frac{1}{2}} \tag{74}$$

Impedance can also be separated by L, C and R as shown below in equations (75), (76) and (77).

$$Z_R = R \tag{75}$$

$$Z_c = \frac{1}{j \times \omega \times C} \tag{76}$$

$$Z_L = j \times \omega \times L \tag{77}$$

The total impedance is some combination of the above sub-impedances. In this dissertation, we have discussed negative index and while not seen in nature is established to be consistent with Maxwell's equations. In equations (76) and (77), it can be seen that there is a frequency factor that appears as a denominator and numerator, respectively. Frequency can be isolated on one side of each equation to demonstrate how inductive and capacitive impedance depends on frequency. In our case, with the models being discussed, resistance can be made small enough to be neglected. In this case it can be seen that permeability relates directly to the inductance per unit length (L`) and permittivity relates directly to the capacitance per unit length (C`) as follows.

$$f_o = \frac{1}{\left[\mu \times \varepsilon\right]^{\frac{1}{2}}} \qquad (78)$$

$$f_o = \frac{1}{\left[L' \times C'\right]^{\frac{1}{2}}} \qquad (79)$$

Applying the above equations (78) through (79), to any material will yield an approximate understanding of how the permeability, permittivity and conductivity affect the wave behavior in a manor consistent with Maxwell's equations.

The model we adopt here still consists of a dielectric sheet having a periodic metal strip pattern on both sides, similar to Kong's original design. Our design of the model shown in the FIGURE 28 has the following specifications: the first and most important is the resonant frequency, second is the total impedance and finally are the physical limitations, such as trace width and length. These factors decide the extent of field fringing contributions, which in turn will affect both the design frequency and impedance. The resonant frequency is decided by the aggregate inductance and capacitance and the impedance depends on material properties such as board dielectric and geometry.

There is an element to this design that introduces a field cancellation in the central part of the S pattern shown in FIGURE 27; this helps produce the simultaneous negative permittivity and permeability. By controlling this effect, one can achieve tunability for both the permittivity and permeability to become negative over some common bandwidth.

The S Pattern is well understood mathematically from a circuit point of view, as seen in FIGURE 27.

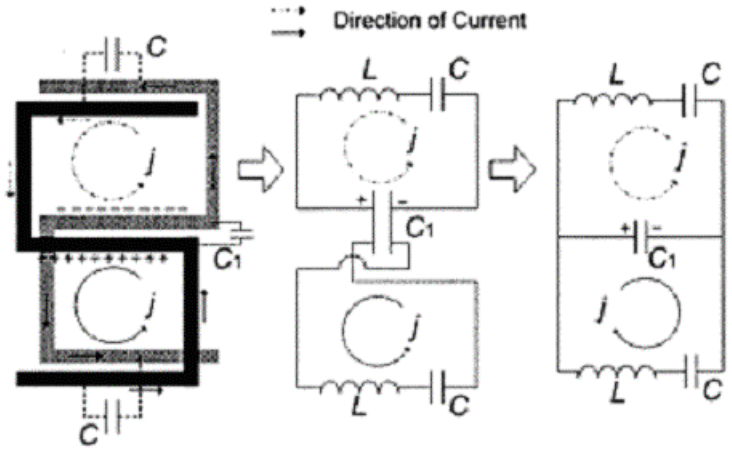

FIGURE 27: S model circuit equivalence

The original S pattern is described by closed form expressions as was shown in section (3.7), similar to equations (1) through (30) derived from circuit theory, and is why this specific pattern was chosen. Our next step was to express a circuit transfer function in terms of Z for the case of two metal S patterns separated by some dielectric. The reason for using two S patterns is to produce the required capacitance and inductive effect that can be developed by the charging current between the elements, otherwise the effect would not be as pronounced. The S model can be configured in one of two ways shown below in FIGURE 28. The first way is to place them back-to-back with one copy being mirrored. Mirrored means the bottom pattern is reversed so that the projected appearance is of two square patterns versus a single S. The second way is to have two patterns oriented or aligned in matching correspondence above and below.

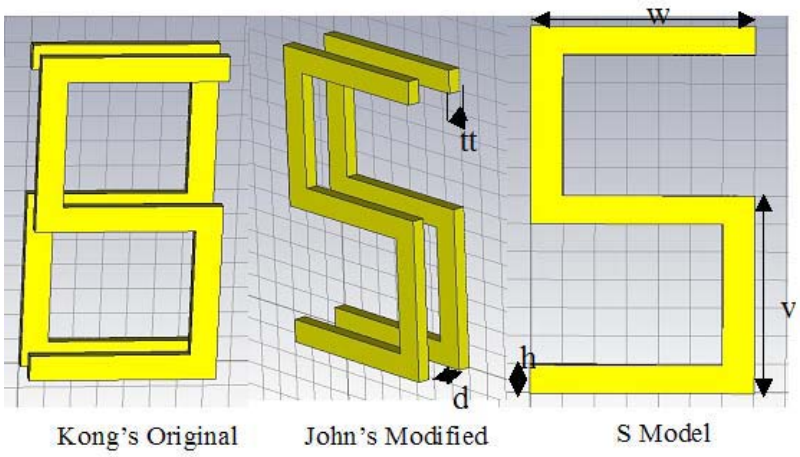

FIGURE 28: S models: different configurations

Thus deriving the microwave circuit equivalence for the S model shown in FIGURE 28 is the objective. One common practice to obtaining a circuit that clearly represents the abstract microwave S model is to use Spice, shown in FIGURE 29. Another way is to apply basic circuit theory using currents and voltages that relate to E and H fields. Both approaches resulted in the same circuit shown in FIGURE 29.

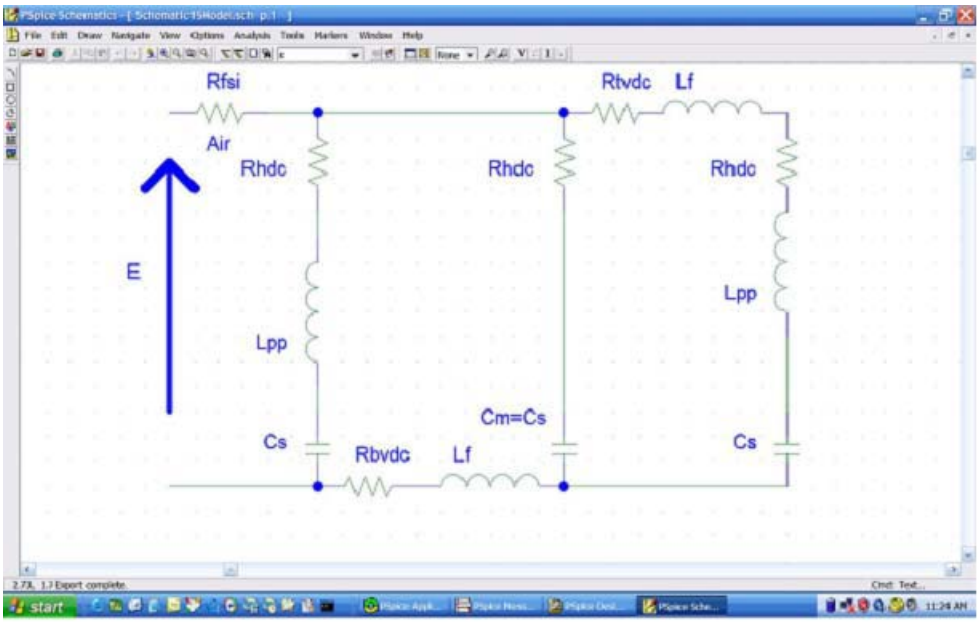

FIGURE 29: Electrical circuit equivalent of the paired S

$$Z_{Total} = \frac{1}{\frac{1}{\left[R_{tvdc} + j\omega L_f + R_{hdc} + j\omega L_{pp} + \frac{1}{j\omega C_s}\right]} + \frac{1}{\left[R_{hdc} + \frac{1}{j\omega C_s}\right]} + \frac{1}{\left[R_{bvdc} + j\omega L_f + R_{hdc} + j\omega L_{pp} + \frac{1}{j\omega C_s}\right]}} \left(R_{fsi}\right) + \left(\frac{1}{\frac{1}{\left[R_{tvdc} + j\omega L_f + R_{hdc} + j\omega L_{pp} + \frac{1}{j\omega C_s}\right]} + \frac{1}{\left[R_{hdc} + \frac{1}{j\omega C_s}\right]} + \frac{1}{\left[R_{bvdc} + j\omega L_f + R_{hdc} + j\omega L_{pp} + \frac{1}{j\omega C_s}\right]}} \right) \quad (80)$$

Equation (80) was derived from combining the impedance representation of each parameter contribution that results from the geometry and material properties of the paired S structure. The S pattern model is represented as a combination of resistance, capacitance and inductance in a series-parallel combination similar to that proposed in Kong's paper.

Definitions of Symbols in eq (80)

Top vertical dc resistance	R_{tvdc}
Horizontal dc resistance	R_{hdc}
Maximum fringing inductance due to vertical side	L_f
Parallel plate inductance	L_{pp}
Bottom vertical dc resistance.	R_{bvdc}
Series capacitance	C_S
Free space impedance	R_{fsi}

This impedance is derived from the combined effect of the R, C and L in parallel and series combinations according to basic circuit theory rules.

The above impedance expression was investigated using Mathcad, and results are shown in FIGURE 30. They illustrate that there is agreement between the analytical model of our design and CST numerical analysis. In FIGURE 31 we see the equivalent CST result and they are almost identical except for one noticeable response in the frequency of the first peak that may be from an unaccounted fringing term. In principle, CST can precisely model all fringing whereas in Mathcad, fringing is only included for close proximity to the edges, and similarly for the inductance. In cases such as these we can estimate the L, C and possibly R-value related to this fringing contribution by adjusting the geometrical area of the capacitance and inductance.

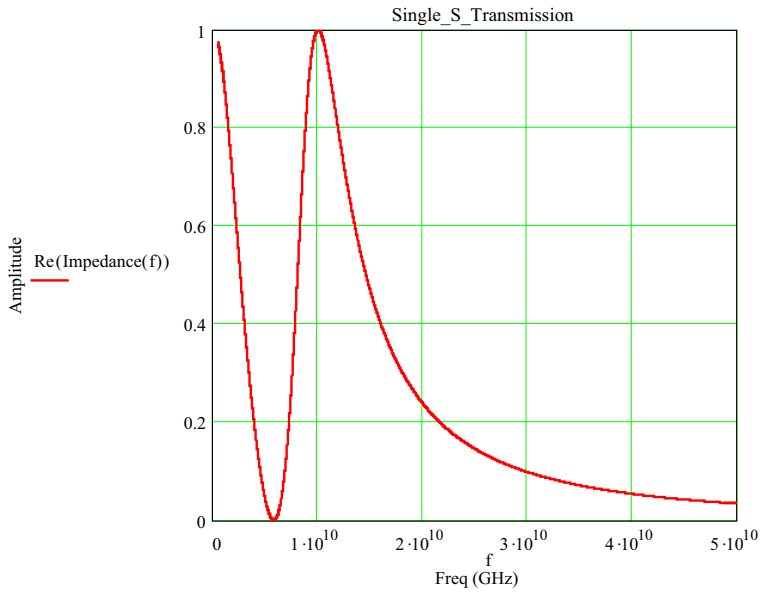

FIGURE 30: Theoretical impedance response of single S

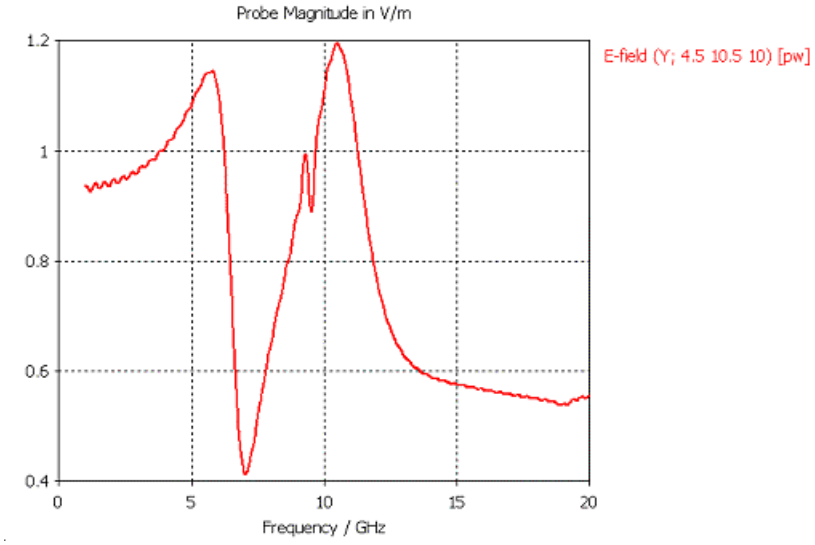

FIGURE 31: CST simulation results for single S

The above simulation using a normal incidence plane wave into the front face of the metastructure shown in FIGURE 23 is consistent with the impedance model that was introduced in equation (80). The resonant response for this single element is very similar

but not identical. As for the smaller feature at approximately 9.3 GHz, this may be due to the finite fringing effect between the horizontal metal strips that is not easily expressed analytically but is seen in the numerical simulation. We next determine the permittivity as a function of frequency from equation (80) followed by repeating a similar procedure to obtain the permeability. There are variable symbols shown in FIGURE 34 that require some further comments for sake of consistency. Resonant impedance is defined as Z_R, which is simply the impedance expression evaluated at the resonant frequency. Both definitions of series inductance being L_S and L_{pp} are equal. Reason for the change of variable was to highlight the fact that the series inductance is formed by two parallel plates. Series capacitance C_S is identically the same as in equation (80). From FIGURE 32, it is evident that the permittivity is negative between 10 and 18 GHz, which is consistent with our design criteria. The permittivity range is approximately between –5 and a maximum of 5.725. The largest imaginary value near 14 GHz is seen as –10.956.

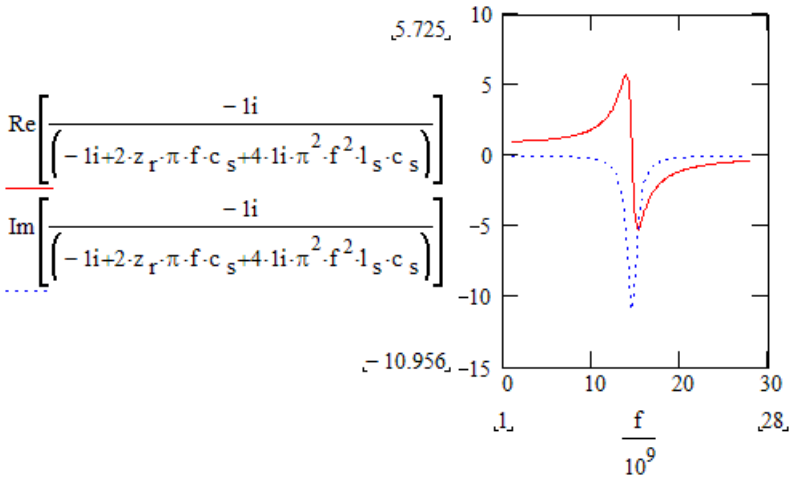

FIGURE 32: Permittivity derived from equations (75) through (79) frequency (GHz)

It was then decided to proceed with a design resonant at 10 GHz and having a narrow bandwidth, the latter being dependent on resistance. 80 sheets having metal patterns on both sides were fabricated and assembled as illustrated in FIGURE 33.

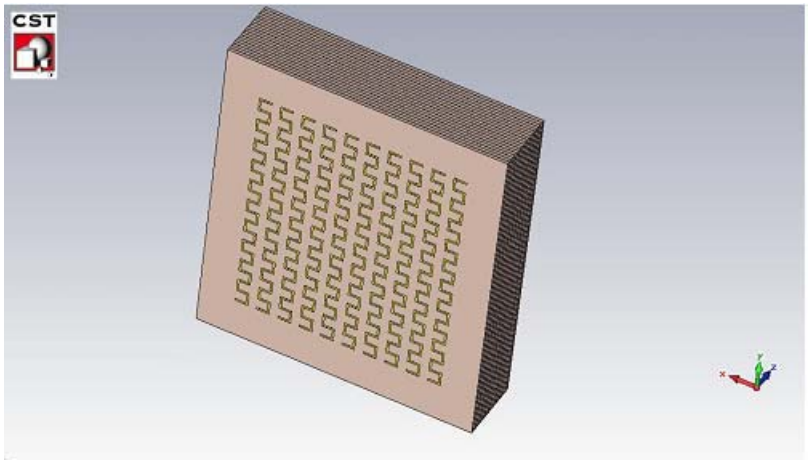

FIGURE 33: Stack of forty original metal S pattern sheets

These sheets were assembled into a rectangular volume for experimental investigation. At that time it was unclear how best to illuminate the structure and characterize its effective index. Kong's original paper [10] presented two cases, i) with the electric field along the y-axis and parallel to the front face of the volume as shown in FIGURE 34. The front face contains the S patterns described earlier and seen in figure 23. Data collected from the transmission experimental trials did in fact show a resonance at 10 GHz but loss was strongly evident and as further experiments would show, unacceptable to our goal of imaging with negative index structures.

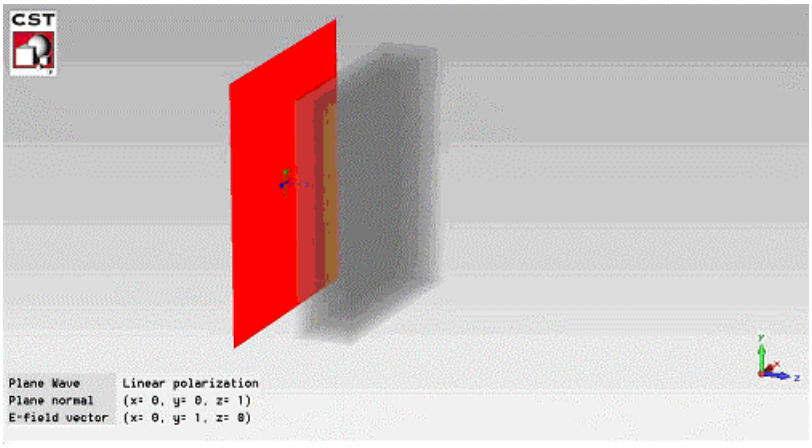

FIGURE 34: Simulation view of plane wave (red) illuminating front face of stack

Following these experiments and more simulations using CST, it became evident that the geometrical size of each S, comprising the metamaterial volume affected the resonance in a predictable way with changes in height and width as expected from its electrical circuit equivalence. Circuit theory became the guiding basis of both future designs and simulations. Our goal is imaging using artificial metastructures modeled as an impedance defined by its scattering or S parameters, no pun. Using the impedance model as the representation of a circuit element in a network provided some additional insight for key design parameters such as resistance, capacitance and inductance. At this point it was also clear that the model we were using was not consistent with the results presented in Kong's paper due to errors in that paper.

Once this was recognized, good progress was made. The first realization was that conductivity could be used to adjust the resonant frequencies while reducing the elemental “S” dimensions, thereby favoring an effective medium approximation. In essence, since a smaller feature size is needed for an improved effective medium while preserving the resonant frequency, then varying conductivity can achieve that. However,

there is a value beyond which any further change in conductivity will not preserve the resonant frequency because the capacitive effect is a function of high conductivity, a decreasing capacitance will shift the resonant frequency higher. Although conductivity can help in achieving an effective medium there is also another trade off that transitions a negative index back into positive values, arising from the inductance or magnetic effect decreasing directly as a function of the conductivity. On-going research continues to determine the optimal conductivity for our metamaterials. Some additional modeling in the sections that follow will further help understanding the role of conductivity.

4.2 Applications Using Varied Range Of Conductivity

Conductivity typically relates to possible loss factors such as absorption, but it is also needed in all of the models applied to developing effective constituent parameters. A question that will be addressed later in this dissertation is, "How is conductivity related to index?". The answer to this question will involve variable conductivity in order to observe how this essential parameter in the mix of constitutive parameters modifies the effective index, whether negative or positive. Conductivity can be also thought of as an initializing "event" that literally spawns a sequence of electromagnetic responses which when organized systematically can lead to the desired responses. Spark gap transmitters are one example of how control of conductivity leads to propagating waves. Metals such as copper have fixed conductivities on the order of 5.8×10^7 *Siemens*/*Meter* or inverse ohms per meter are another way to understand the dimensionality. Other metals such as Al (Aluminum) 3.817×10^7 S/M, Tin 8.77×10^6 S/M and Hg (Liquid Mercury) 1.04×10^6 S/M, illustrate the range of possible conductivities. One last material to think

about is graphite with $7.143 \times 10^4 \, S/M$, which is used in many current conduction-related applications, such as electrical resistors, high power transmitters, electrical motors, arc welding, high temperature furnaces and super carbon super conductivity. The point being made here is that the conductivity of carbon graphite is orders of magnitude below copper yet still provides comparable current handling functions. So the required magnitude of conductivity needed to affect certain material responses is not strictly specified. We now introduce some equations relating to conductivity, which are introduced to allow further insight into this fundamentally important constitutive parameter. Lets begin first with how permittivity is defined in many electrical domains.

4.3 Permittivity & Maxwell's Equations

The electric field flux density $\vec{D}$ can be described by equation (81) relating electric flux to charge (Q) and radial distance (r) from the point charge. The electric field $\vec{\mathrm{E}}$ has a similar expression seen in equation (82).

$$\vec{D} = \frac{Q}{4\pi r^2}\hat{r} \tag{81}$$

$$\vec{\mathrm{E}} = \frac{Q}{4\pi \varepsilon_0 r^2}\hat{r} \tag{82}$$

$$\vec{D} = \varepsilon_0 \vec{\mathrm{E}} \tag{83}$$

Equation (83) is the relationship between the electric field intensity and electric field flux in free space, but lets assert that the medium material is polarization sensitive and represent this as $\vec{\mathrm{P}}$, then equation (83) becomes equation (84), which is a very basic and general description of permittivity.

$$\vec{D} = \varepsilon_0 \vec{\mathrm{E}} + \vec{\mathrm{P}} \qquad (84)$$

It is well known, as shown in equation (85) that the polarization P can also be expressed as follows.

$$\vec{\mathrm{P}} = \chi_0 \varepsilon_0 \, \vec{\mathrm{E}} \qquad (85)$$

$$\vec{D} = \varepsilon_0 \vec{\mathrm{E}} + \chi_0 \varepsilon_0 \, \vec{\mathrm{E}} \qquad (86)$$

$$\vec{D} = (1 + \chi_e) \varepsilon_0 \vec{\mathrm{E}} \qquad (87)$$

$$\varepsilon_r = (1 + \chi_e) \qquad (88)$$

where χ_e is the electrical susceptibility.

Equation (88) can now be taken as an implied definition of the relative permittivity or dielectric constant in terms of a related concept, the susceptibility. Thus equation (83) can be rewritten to represent any medium in the following manor.

$$\vec{D} = \varepsilon_r \varepsilon_0 \vec{\mathrm{E}} = \varepsilon \, \vec{\mathrm{E}} \qquad (89)$$

Now the much better known expression for permittivity is shown in equation (90)

$$\varepsilon = \varepsilon_r \varepsilon_0 \qquad (90)$$

Recall that the conductivity is a constitutive parameter, relating total current to the electric field as seen in equation (91).

$$\vec{J} = \sigma \, \vec{\mathrm{E}} \qquad (91)$$

Equation (91) is commonly known as Ohm's law for linear, isotropic homogeneous materials. We define conductive resistance here as equation (92).

$$R = \frac{length}{\sigma\, CrossSectionalArea} = \frac{length}{\sigma A} \qquad (92)$$

Capacitance relates to the ratio between charge, Q and potential, V, that results from performing the necessary integration over conductive surfaces. For the case of rectangular geometry, such as the case with the meta models being studied in this research then we can write the following equations (93) through (96).

Potential difference or the voltage (V) between two charged surfaces, referred to as s+ and s- separated by some linear distance is given by

$$V = -\int_{S-}^{S+} \vec{\mathrm{E}} \bullet d\vec{\ell} \qquad (93)$$

$$Q = \oint_{S+} \vec{D} \bullet d\vec{s} = \oint_{S+} \varepsilon\, \vec{\mathrm{E}} \bullet d\vec{s} \qquad (94)$$

$$C = \frac{\oint_{S+} \varepsilon \vec{\mathrm{E}} \bullet d\vec{s}}{\int_{S-}^{S+} \vec{\mathrm{E}} \bullet d\vec{\ell}} \qquad (95)$$

$$I = \sigma \int_S \vec{J} \bullet d\vec{\ell} = \sigma \int_S \vec{\mathrm{E}} \bullet d\vec{\ell} \qquad (96)$$

Forming a relationship between inverse resistance with current and voltage allows one to write:

$$\frac{1}{R} = \frac{\sigma \int_{S} \vec{E} \bullet d\vec{\ell}}{\int_{S+}^{S-} \vec{E} \bullet d\vec{\ell}} \tag{97}$$

$$RC = \frac{\varepsilon}{\sigma} \tag{98}$$

This general result shown in equation (98) can be used to indirectly measure the value of capacitance at some prescribed location how ever small, by direct current measurement, given some conductivity and permittivity. The primary reason it is worth following these detailed steps from equations (81) through (98) is to avoid confusion about assumptions underlying any of these specific formulas. For example, in many instances these formulae do not allow for the real possibility of fringing contributions, which detract from having reliable results, which are needed to design real structures, when using them.

A second helpful finding was that our impedance model contradicted Kong's model for the structure illuminated on the front face, but was in agreement when illuminated from the side, as seen in FIGURE 23. We identified the error in Kong's paper. We also realized that if all of the mirrored metal patterns were removed from the backs of the boards, it would still be possible to get an observable backward wave motion, corresponding to a negative index.

CHAPTER 5: IMAGING EXPERIMENTS

In this chapter, Figures 35 through 41 illustrate some of our simulations of imaging with a planar negative index volume in which conductivity was used as a parameter to tune the index values and associated bandwidth. We designed a structure first based on the Drude model in order to realize a homogenized –1 index. This corresponded to an ideal case but one with physical meaning (i.e. it is not just specifying that n = -1), which would allow us to better understand the imaging capabilities of a finite sized negative index slab. It would not be possible to transform this model into a realistic equivalent patterned structure, using available materials, that we could make, but we hoped to approximate it. Thus this approach has one significant benefit and that is producing a model with exactly –1 index to test out the imaging simulations. FIGURE 35 a single slit placed in front of a metamaterial and illuminated by a plane wave. The single slit acts as an object to be imaged as can be seen in FIGURE 36; an image is formed on the emerging side. This was our first real evidence of being able to simulate imaging with an idealized negative one-index structure.

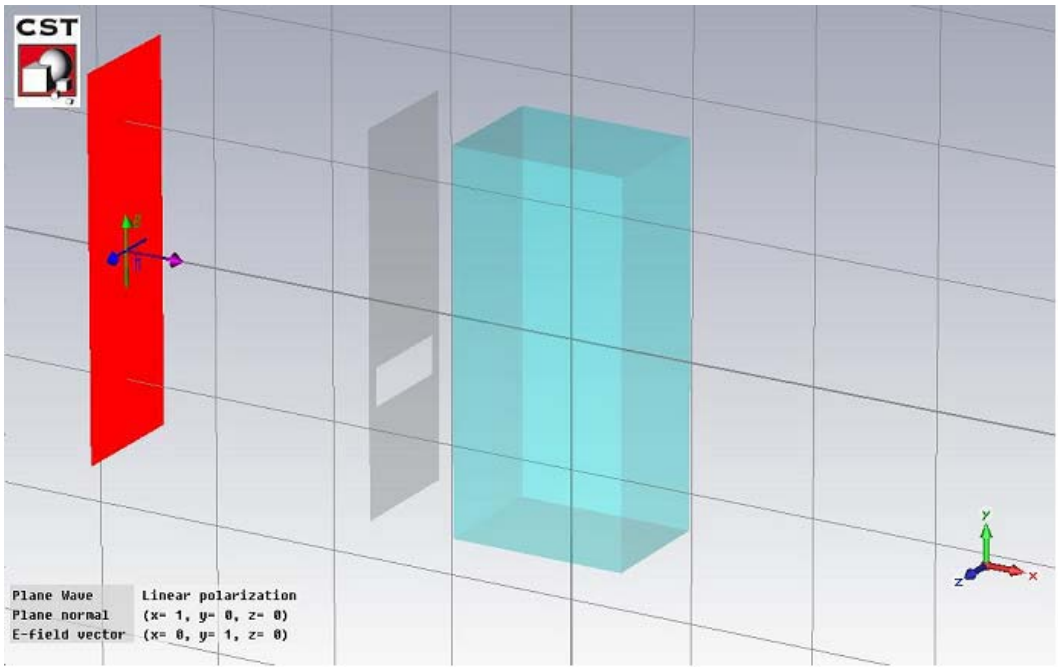

FIGURE 35: Single slit plane wave illumination setup

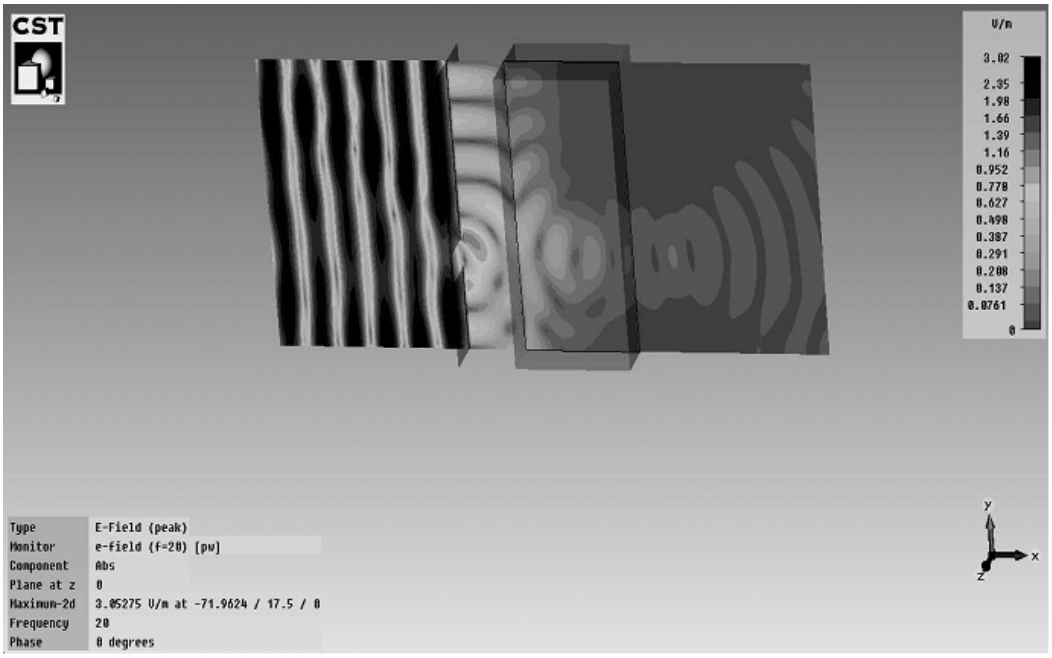

FIGURE 36: Single slit plane wave 20 GHz frequency simulation

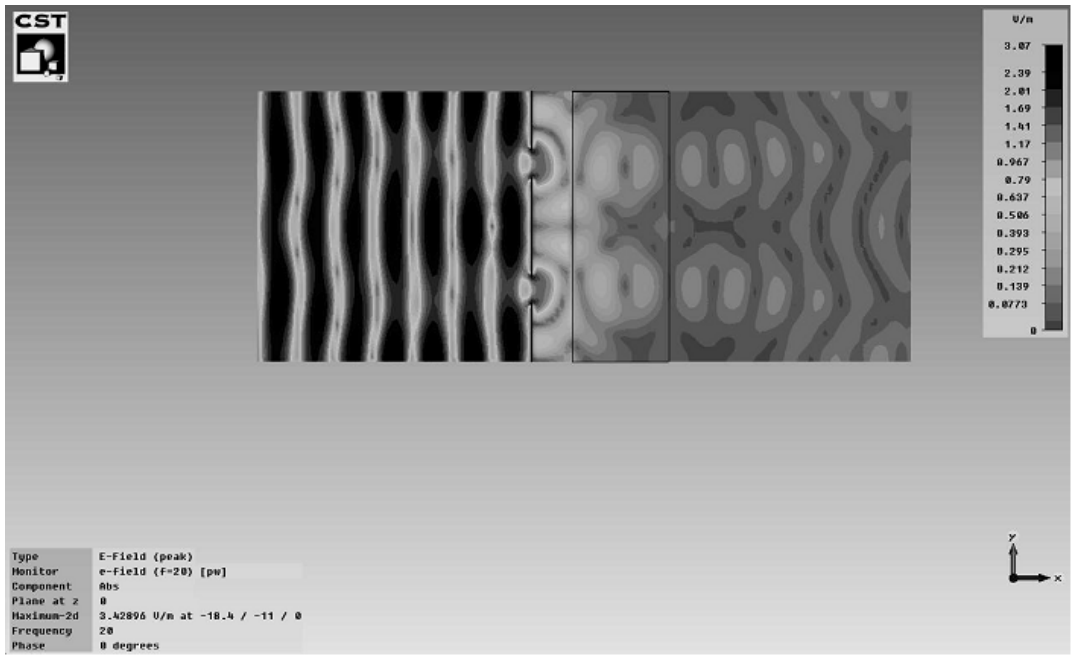

FIGURE 37: Double slit plane wave illumination setup

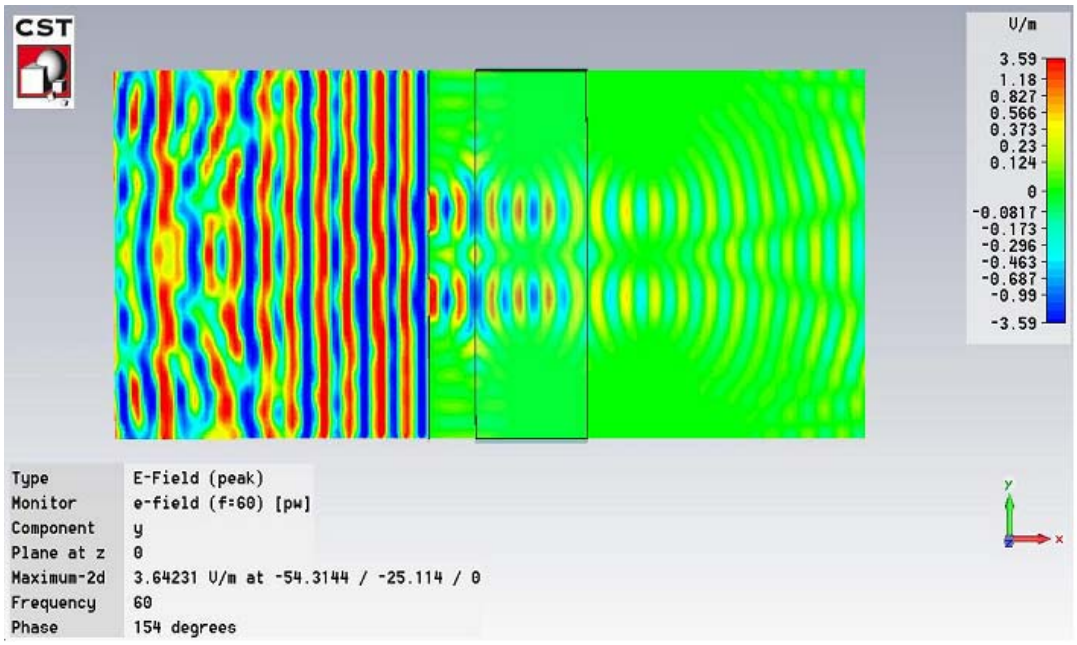

FIGURE 38: 5mm double slit spacing simulation using a wavelength of 5 mm

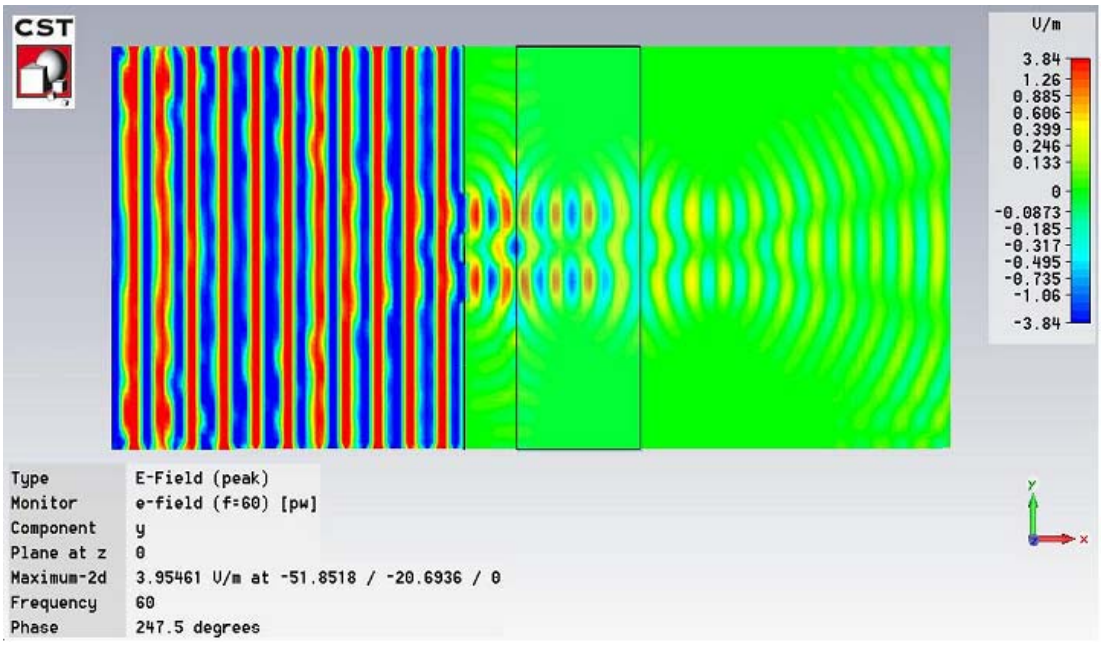

FIGURE 39: 2.5mm double slit spacing simulation using a wavelength of 5mm

Figures 37, 38 and 39 are included to demonstrate how the image formation follows directly from object size and various slit spacing. FIGURE 37 represents imaging of two objects spaced two wavelengths, which is 3 cm at 20 GHz. FIGURE 38 displays the imaging of two objects spaced by one wavelength that is 5 mm at 60 GHz. Finally FIGURE 39 clearly demonstrates the image resolution is well resolved given the two objects are separated by a half wavelength of 2.5 mm. These three figures are an example of highly resolvable microwave imaging. One last point regarding FIGURE 39, and that is the object size is less than one half of a wavelength. Close examination of these figures will show one to one correspondence between objects and images down to the smallest detail.

A concern when trying to validate Pendry's prediction about a n = -1 lens amplifying evanescent waves is to know whether our simulation tool, notably CST, is capable of

modeling situations in which evanescent waves are generated and coupled into propagating waves this was done and will be discussed at length in the sections that follow. Here we simply illustrate two of the numerical examples that confirm that CST should be able to replicate Pendry's prediction.

Figures 40 and 41 demonstrate that CST can show evanescent waves coupled into propagating waves with a decreasing thickness of the gap between two high index regions in which total internal reflection is taking place. As expected, the surfaces need to be placed very close together, within a wavelength, in order to couple the evanescent waves.

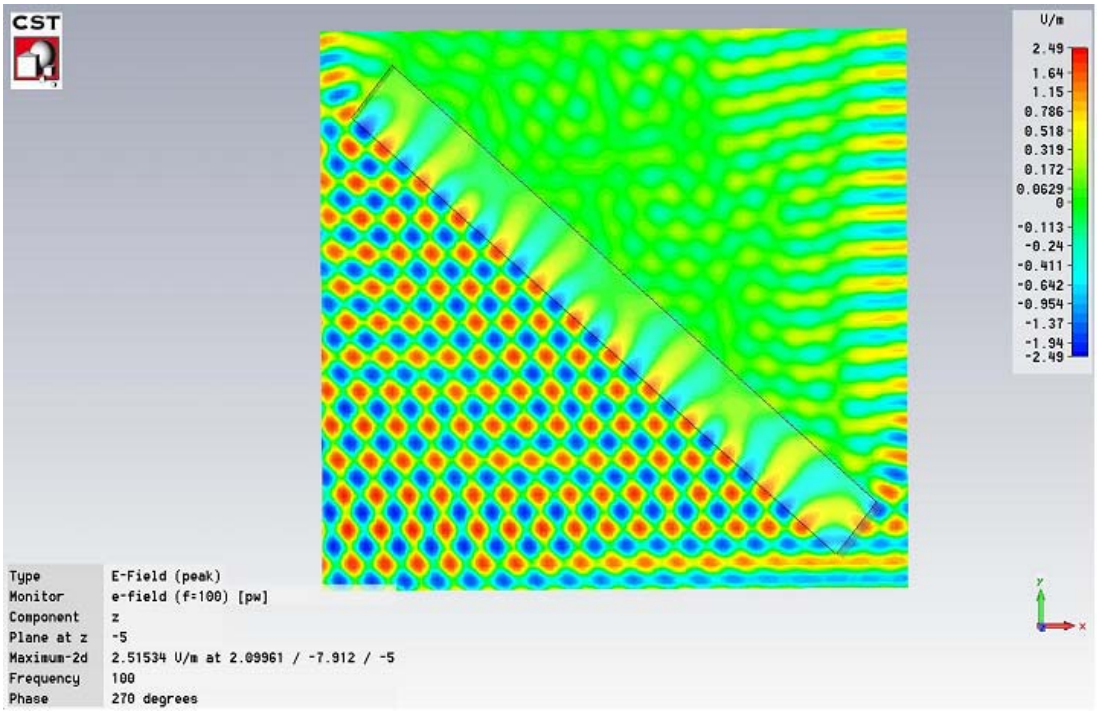

FIGURE 40: Weakly coupled evanescent waves

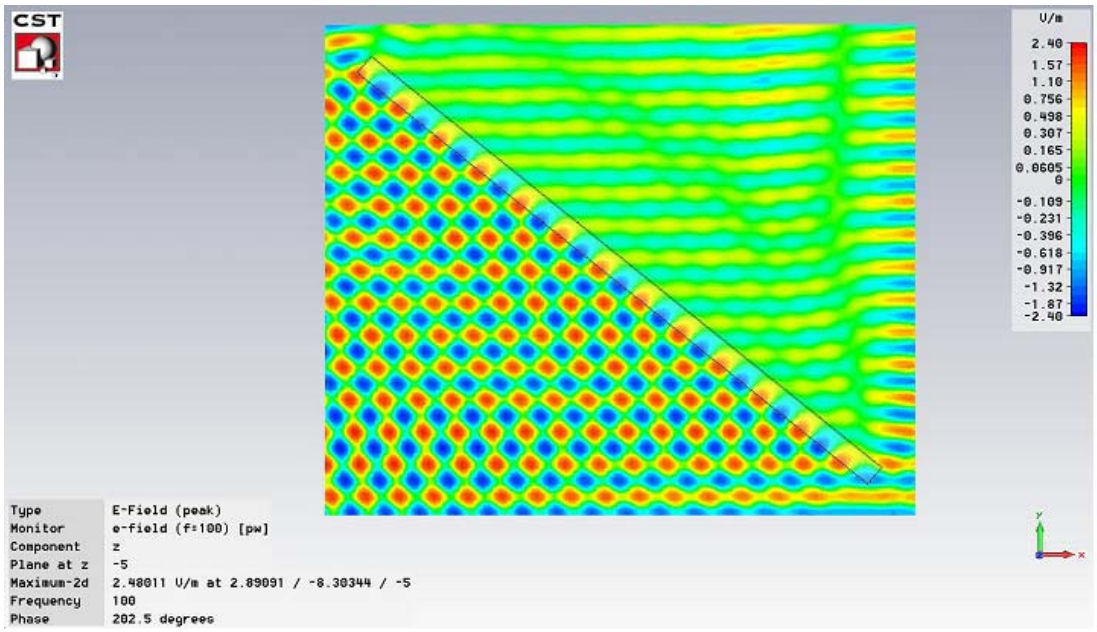

FIGURE 41: Evanescent waves coupled into propagating waves

This transformation of non-propagating evanescent fields was realized with a smaller gap between the two high index media. Some helpful details related to Figures 40 and 41 are as follows. Total internal reflection provided the basis to demonstrate how a medium with an index of 1 when surrounded by and index of approximately 2 could be used to investigate evanescence. The specific conditions leading to the results shown in Figures 40 and 41 was an electric field aligned with the z axis at a frequency of 100 GHz propagating in the y direction from a higher index medium of n=2 into a block of air, at an angle approaching 40 degrees. When the thickness of the air block was greater than or equal to one wavelength, which is 3mm then there was not any observable evanescent coupling, in fact is was as if there were a complete disconnect. When the thickness was adjusted to three quarter wavelength, half wavelength and then one third the degree of coupling continued to increase proportionately. For the case of FIGURE 41 the thickness was one half wavelength. Now the last point here is that evanescent contribution can be

indirectly associated to a perfect image as the index approaches exactly –1. An index of exactly -1 is the requirement for evanescent amplification, which provides the necessary contribution for a perfect image. Therefore having exactly a –1 index is the central priority.

5.1 Resolution And Perfect Images

Imaging systems in general typically experience resolution limitations decided by the spatial wavelength (λ) and their numerical aperture. Object feature sizes, which are smaller than λ or encoded by spatial frequencies beyond the high spatial frequency cut-off of the lens become unresolvable. We are particularly interested in trying to image features associated with sub wavelength components and testing Pendry's "perfect" imaging claims. Sub wavelength contributions relate to such high spatial frequency components that they are evanescent waves. As discussed above, evanescent waves decay exponentially away from the object space in the direction of the propagating wave. This fact prevents in most cases the collection of all the required information needed to form a perfect image. It is apparent from Pendry's analysis that evanescent contributions to the image formation are ALL included if one has exactly a –1-index medium with very low loss. As an aside, having an n = -1 index medium is also going to ensure that there will not be any unwanted reflections from the negative index medium when the background is composed of air. This point perfect impedance match assists with the evanescent coupling into the medium. Proceeding with the idea or insight gained from section 5.1 indicating that evanescent waves can be transformed into propagating waves and given the fact that there is a –1 index, absent of reflections, it's plausible to accept how our simulations of evanescent field can also successfully describe their amplification

as predicted by Pendry. Upon entry into the resonant negative index region we expect that field enhancement will result. This enhancement or amplification phenomena is essential for high resolution imaging since it supports the evanescent wave transfer through the negative index region to the image plane. In other words, evanescent waves emerging from this region being amplified in comparison to the input wave will from the point of exit be decreasing to a level that is theoretically equal in both amplitude and position comparable to the object field from the region.

There is one other inherent and possibly unavoidable issue that could limit evanescent amplification, which is the loss associated with the imaginary part of complex permittivity $\varepsilon^{"}$. Pendry [18] explains how lens thickness and absorption will limit the imaging resolution. Absorption exists in both metal and dielectrics. and is typically linked with conduction loss σ and polarization loss respectively. These losses can be expressed using equations (6) and (13), which are complex representations of the propagation constant γ and wave impedance η. Total loss for conductors can be defined as an effective conductivity due in part to frequency dependence as seen in equation (99).

$$\sigma_{eff} = \sigma_{metal} + \omega\varepsilon^{"} \tag{99}$$

Equation (90) defines the real part of the permittivity, which can now be further expanded to include the imaginary part as show in equation (100).

$$\varepsilon_{eff} = \varepsilon^{'} - j\left(\varepsilon^{"} + \frac{\sigma}{\omega}\right) \tag{100}$$

Equations (99) and (100) are general expressions that can be applied reliably to quantify loss but in some instances this process may become too cumbersome for straightforward evaluation. Another way to specify loss is by using the idea of loss angle

and loss tangent of the medium. An alternative to equation (100) is shown in equation (101).

$$\varepsilon_{eff} = \varepsilon_r \varepsilon_o \left(1 - j \tan\phi\right) \qquad (101)$$

Where ϕ is the loss angle and $\tan\phi$ is the loss tangent of the material that characterizes absorption. By substituting equation (101) into (100) the loss tangent can be expressed as seen in equation (102).

$$\tan\phi = \frac{\varepsilon''}{\varepsilon'} + \frac{\sigma}{\omega\varepsilon'} \qquad (102)$$

There are two terms in Equation (102) referred to as alternating electric loss tangent plus static electric loss tangent respectively. These terms can be minimized for specific cases such as when $\sigma = 0$, and then the imaginary part of the permittivity can be defined as equation (103).

$$\varepsilon'' = \varepsilon' \tan\phi \qquad (103)$$

The primary reason to recast these definitions is to simplify the evaluation of many commonly used materials, given that there are many tables of precisely determined loss tangents. One other point to consider with loss tangents is the frequency used for the absorption measurement, which in many instances is microwave X-Band, which is 8 to 12 GHz.

Equations (99) through (103) will now help is discussing the references introduced regarding the relationship between loss and resolution. One additional point before continuing on relates to the phase velocity. The cases being investigated with respect to resolution involve low loss metamaterials and this allows the loss tangent to be less than

unity in many cases. Without further derivation it will be shown how the phase velocity can be approximated given a low loss metamaterial seen in equation (104).

$$V_{phase} = \frac{1}{\sqrt{\mu\varepsilon}}\left[1 - \frac{1}{8}\left(\frac{\sigma}{\omega\varepsilon}\right)^2\right] \qquad (104)$$

Close inspection of equation (104) shows that there are cases where the parenthetical coefficient could be negative for a wide range of specific frequencies and conductivities. Here phase velocity depends strongly on conductivity and frequency and the index depends on the phase velocity as seen in equation (14). By varying conductivity you can vary the index directly as evidenced by equation (104).

Pendry [18] claims there is a resolution limit given by the following equation (105)

$$\Delta = \frac{2\pi d}{\ln\left(\left|\varepsilon''\right|\right)} \qquad (105)$$

Thickness is d and ε'' is the imaginary part of the permittivity shown in equation (105), but for sake of consistency the more general equation for ε'' will be introduced here in (106).

$$\varepsilon'' = \frac{\varepsilon'\omega\tan\phi - \sigma}{\omega} \qquad (106)$$

Substituting equation (106) into (105) results in (107)

$$\Delta = \frac{2\pi d}{\ln\left(\left|\frac{\varepsilon'\omega\tan\phi - \sigma}{\omega}\right|\right)} \qquad (107)$$

Resolution from a qualitative point of view, talks about a spot size, in other words the smaller the better. Any system that can resolve very small points independent of

wavelength will be very attractive to many imaging applications. Here is why the importance of resolution is stressed. So defining resolution correctly becomes paramount to the objective of super resolving. To test out this expression it becomes necessary to clearly understand what exactly is being affected by thickness and loss tangent, which directly relates to conductivity. To begin answering these questions, dimensional analysis was first applied to equation (107) and the result was simply circular area over capacitance. This analysis now shows an association with spot size given that circular area can be operated on to produce a diameter. Upon further investigation it becomes evident that thickness, conductivity and to a limited extent frequency dominate the resolution estimation. It's important as well to clearly describe in a brief statement what equation (107) is saying. System imaging resolution is limited to spot size diameters that directly follow conductivity and thickness, and inversely frequency. In other words, it describes the smallest resolvable diameter. To see this statement by mathematical example, a function of conductivity, thickness and frequency was written in Mathcad, shown in equation (108). This function is based on the idea that equation (107) can be operated on to use circular area to calculate the diameter, divide by π, take square root and the multiply by two.

$$SpotSizeDiameter = 2 \cdot \sqrt{\frac{2 \cdot d}{\ln\left(\left|-\frac{\sigma}{\omega}\right|\right)}} \qquad (108)$$

For a trial examination lets introduce a table to further illustrate the spot size diameter dependence for various thickness and conductivities at three different frequency data sets shown in FIGURE 42.

Frequency	Sigma	Thickness mm	Thickness mm	Thickness mm
Spot Size Table		50	60	70
			Spot Size Diameters	
8 GHz	5.00E+06	7.36	8.07	8.71
	5.00E+07	8.88	9.73	10.50
	5.00E+08	12.01	13.16	14.21
8.5 GHz	5.00E+06	7.33	8.03	8.68
	5.00E+07	8.83	9.67	10.44
	5.00E+08	11.88	13.02	14.06
9 GHz	5.00E+06	7.31	8.00	8.64
	5.00E+07	8.78	9.61	10.38
	5.00E+08	11.76	12.89	13.92

FIGURE 42: Spot size diameters in (mm) shown in gray

FIGURE 42 consists of the variable parameters highlighted in light turquoise and the spot size diameters in the light gray section. This table clearly shows that the spot size only varies negligibly over frequency and strongly with conductivity and lens thickness. This table shows the resolution limits that results for loss or added lens thickness. Purpose of the table is to provide an approximate reference for comparison to any simulated or actual experimental data related to the imaging resolution. Whether this table is precisely correct or not is serves at least as a guide to continue on with high resolution imaging using negative index metamaterials. There is one other figure being introduced, which is a graph of the table being shown in FIGURE 43. The plot shown in FIGURE 43 will just serve to emphasize the dependence relationships.

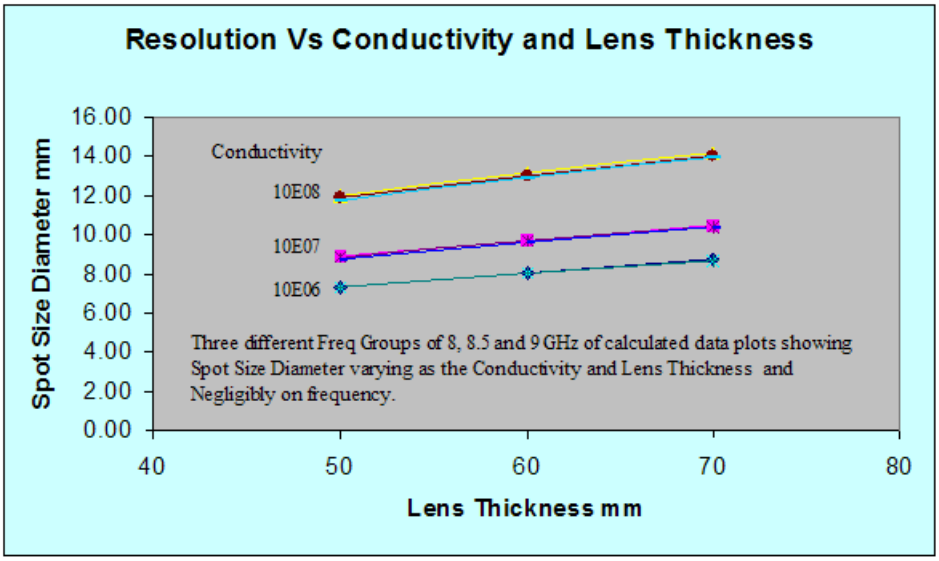

FIGURE 43: This is a graph of the tabulated data in figure 44

Based on the preceding discussion on how loss effects resolution it will suffice to conclude that reduced thickness and lower loss contribute to improved image resolution as learned from the calculated values in both figures 42 and 43.

5.2 Simulations Demonstrate Perfect Image As Index Approaches –1

Additional CST simulations clearly demonstrate how the image formation continues to near perfect one to one correspondence with the object as the index approaches a negative one. The simulations encompassed a range of imaging scenarios using index values between (-.5 and –1.5). The conclusion is that in order for the image to become perfect, the index must in fact be exactly –1. Index values that deviate from –1 will result in distortion and imperfection. Seven simulations are presented here and others are shown in Appendix A.

In section 5.1 it was demonstrated that CST could both model and simulate evanescent behavior. The primary reason for that exercise was to verify that one could

simulate the important coupling of the non-propagating or evanescent waves into the negative index medium. Examination of Pendry's theory [4] it becomes clear that if the medium did effectively exhibit a –1 index and the medium were placed sufficiently close to the scattering object, as demonstrated by the CST simulation shown in section 5.1, then the resulting image formation would be in perfect one to one correspondence. If the object is not sufficiently close to the negative index medium then neither the numerical accuracy of the simulations nor attempts to achieve a perfect image with a real metamaterial, will succeed. Now with this basis clearly in mind, it stands evident that if the image observed were approximately characterized as being not perfect but to some extent super resolved then the conclusion would be that evanescent waves were coupled into propagating waves, thereby providing the higher frequency contributions needed for the high resolution image formation. One other point of significance, working in the microwave X-Band, which is centered at 10 GHz, with a spatial wavelength of 3 cm does in fact lessen the difficulty of coupling evanescent fields into the metamaterial by many orders of magnitude in comparison to visible light imaging. So for the evanescent case being discussed, it would be safe to estimate that when the medium is within a distance less than one wavelength or 3 cm for 10 GHz, the degree of coupling will be sufficient to transform at least a set of decaying exponential waves from the object that are in proximity to the negative index lens into contributing high spatial frequency waves in the image domain. The number of evanescent wave's contributing will increase exponentially with approaching an index that is exactly –1.

To further aid the process of understanding the images that follow, specifically Figures 44 through 50, there will be a brief description preceding the figure pointing out

salient aspects germane to supporting the central idea being proposed. The purpose of these seven figures is to show how the image formation changes as the index approaches –1 from values above and below. Central idea is that the simulated results clearly show the image becomes perfect as the index nears –1.

Figures 44 and 45 provide a comparable reference presented in two different contrasting formats to allow as much detail as possible for analysis and review. Basic scheme shown here is, a plane wave traveling from left to right into a double slit mask that results in two half spherical sources or objects for imaging by the planar meta lens. The mask is positioned in front of the lens by approximately one half of lens thickness. Planar lens has an ideal –1 index with some loss but minimal. In accordance with the theory offered from Veselago [6], rays at all angles from the objects will focus once inside the lens and again on the emerging back side at a location similar to the objects position. Notice in FIGURE 44 how the image formed inside the lens is in one to one correspondence with the outside entry area. At this moment direct the attention to the middle of the planar lens where there is what appears to be, three dark wholes or spaces. Here is where the slit images are forming and if very close examination is made it might become obvious that the two images are located below and above the center whole or space. This is an observable estimation from this point of view. There will undoubtedly be viewing differences depending on the operating system and resolution setting being used. So this discussion is based on what is being observed in the existing files. Another thought to keep in mind is that as the index increases or decreases the image will shift accordingly. For example, -1 changes to –1.1, an increase of -.1, then the center image will begin to move to the right and vice versa. As mentioned there should also be a

second refocusing of the objects in exiting space and again this is visible, but with a noticeable loss of resolution due in part to the existing loss in the model. It's important to keep this image formation in reference as the index changes about –1. What matters is to learn how the changing index effects the image location and formation.

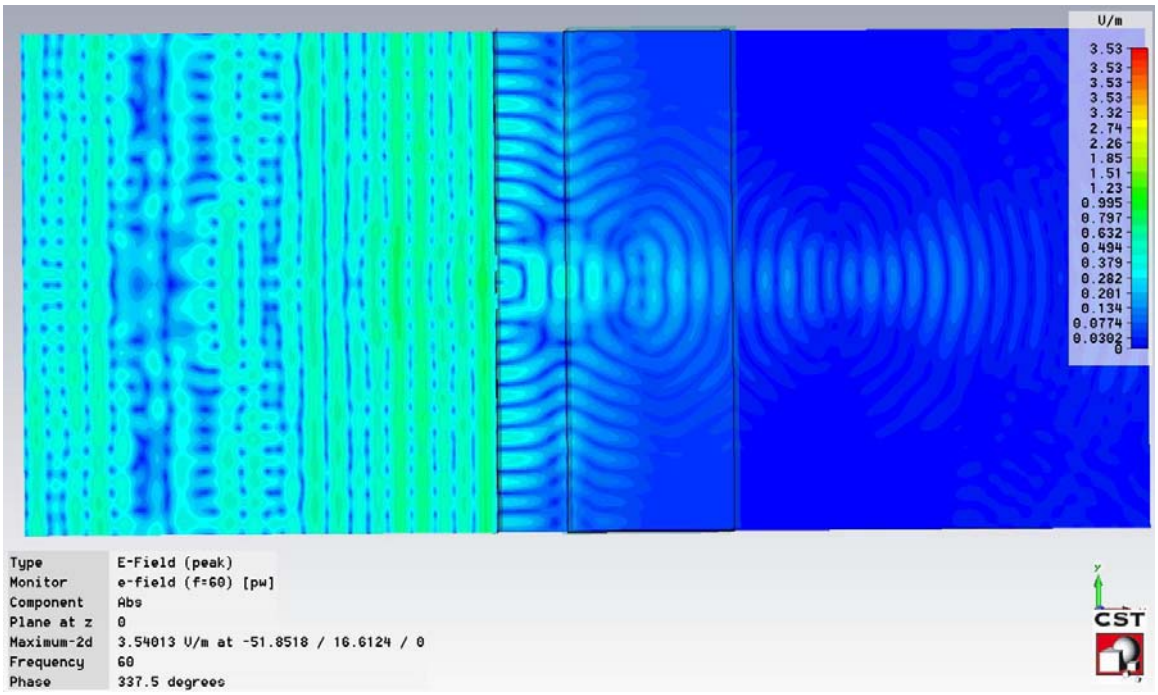

FIGURE 44: Double slit illuminations into –1 index region: two images observed

Some added comments about FIGURE 46 will be helpful in view of some absent observable signs of surface waves. There is more than one perspective view of simulated data and in this case shown here the emphasis is on images inside the meat structure and out to right in image space. There are two sets of images though it might be difficult depending on the viewing system. To further help this illustration it would help to offer some guidance. First beginning with the right side of the meta lens count to the fifth ring and it's expected that you will see a thin line that is somewhat shaded in the center, this is the imaged object pair with some what reduced contrast, but if close examination is made

either by expanding the figure or just one to one correspondence it should be obvious. The following figures will help to further reinforce this description.

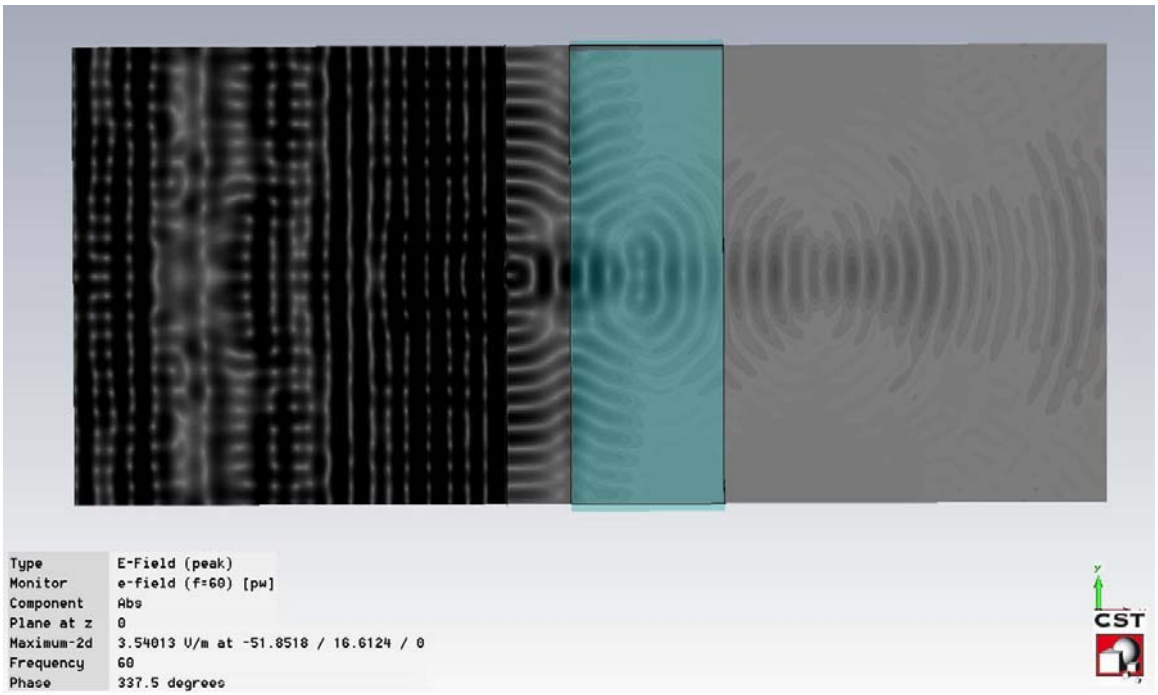

FIGURE 45: Double slit illumination into –1 index region: each image observed

Figures 46 and 47 demonstrate two noticeable changes in the imaging performance, which is reduced image contrast inside and out, image shifted right on the inside and left on the outside, in other words the second image on the right side of the lens moves toward the back side of the lens. In FIGURE 47 the images on the inside and outside are moving toward each other, thus further distorting the resulting image formation. Also pay particular attention to double images being formed both inside and out as well.

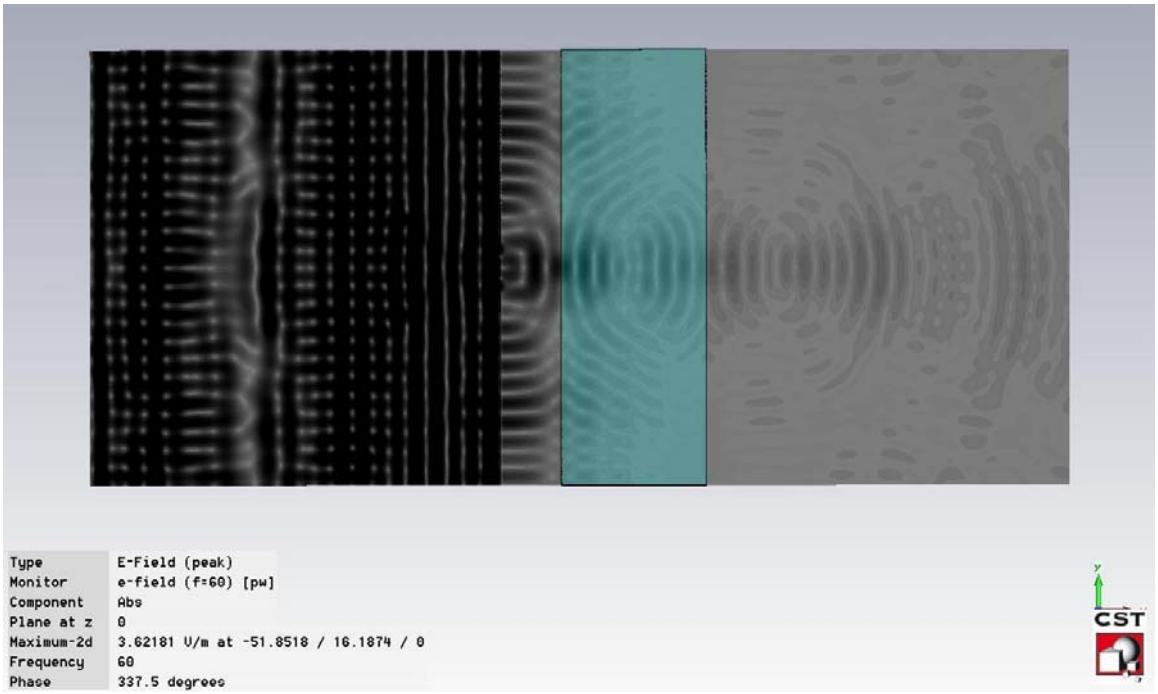

FIGURE 46: Double slit illuminations into –1.1 index region, imperfect images

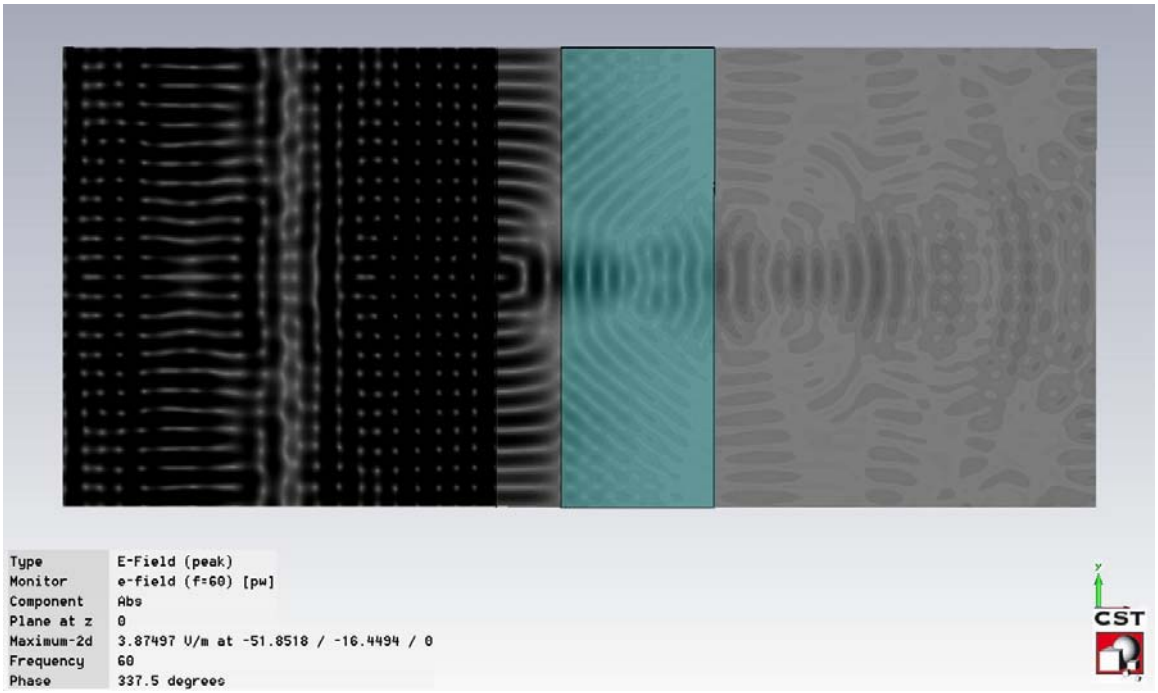

FIGURE 47: Double slit illuminations into –1.2 index region, imperfect images

In FIGURE 48 the first focusing point or region is approaching the exiting side, which may result in an absent second focus, and here is where distortion dominates.

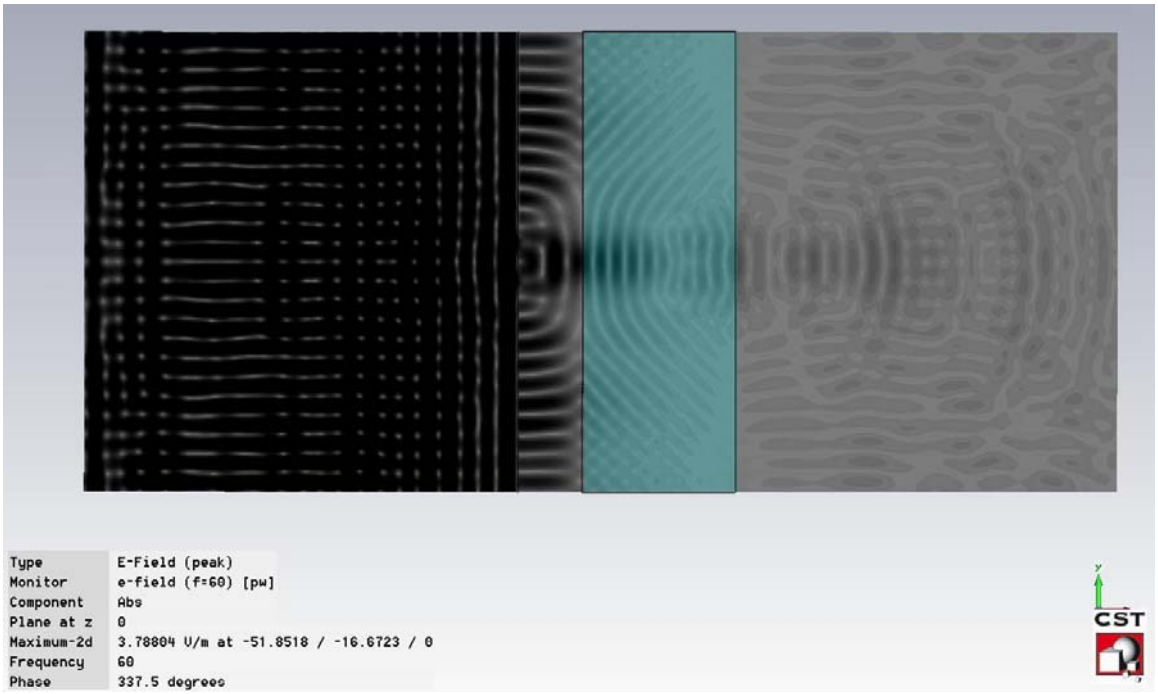

FIGURE 48: Double slit illuminations into –1.3 index region, imperfect images

In these last two figures 49 and 50 the index is smaller than –1 and it is clear that the internal image has shifted towards the left, while the external image moves to the right. So the images move apart as the index decreases below the –1. Another interesting observation is the absence of double images unlike the case when the index was increasing above -1. Last point is the reduction in observable detail in both regions, inside and outside, and contrast is significantly reduced.

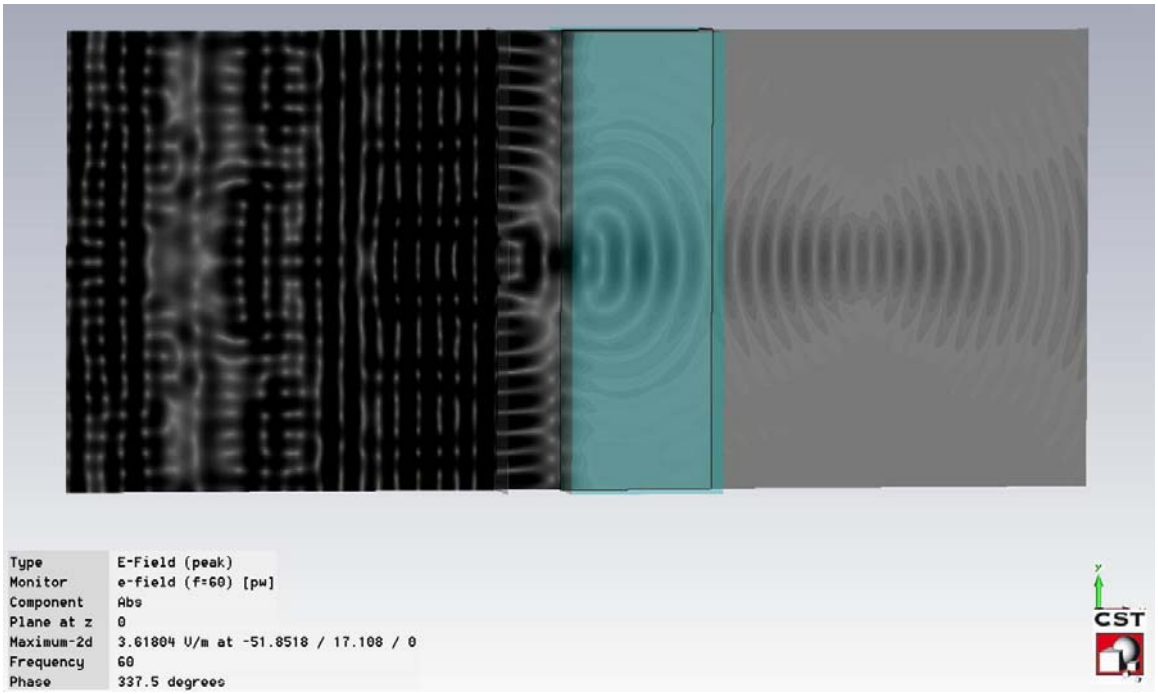

FIGURE 49: Double slit illumination into – 0.8 index region, imperfect images

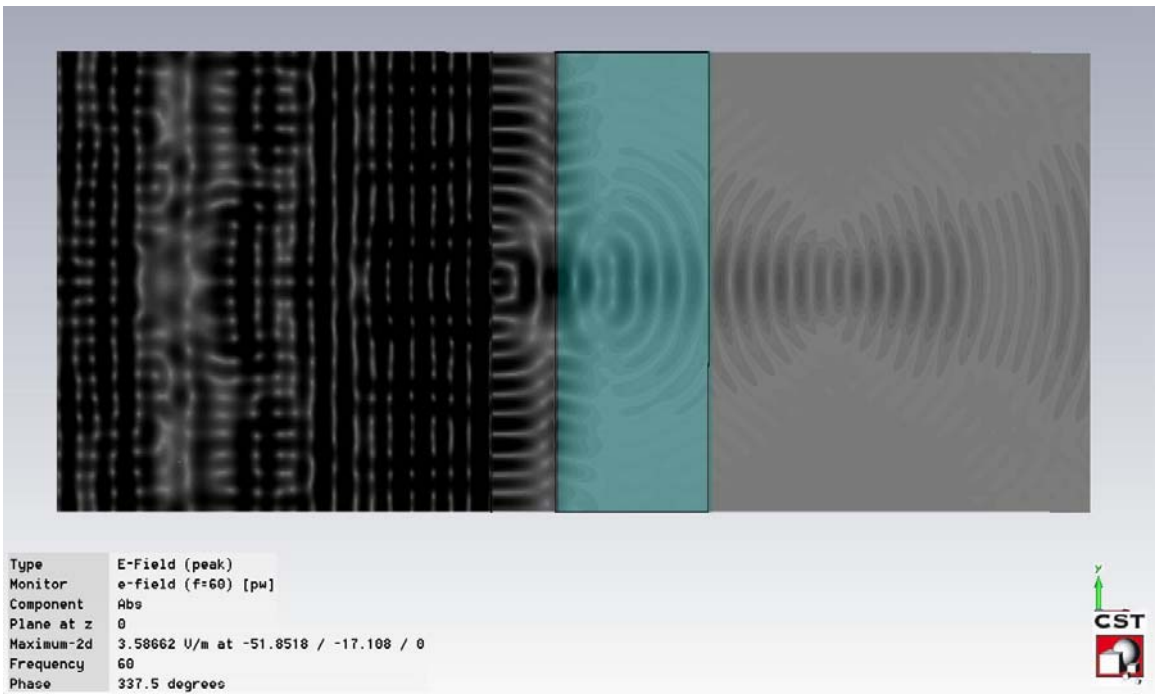

FIGURE 50: Double slit illumination into – 0.9 index region, imperfect images

Brief summary, Figures 44 through 50 have demonstrated that image formation approaches perfection as the index approaches –1 from either side of the scale. For

indices smaller than –1 the images move away from each other where as the when the index is above –1, they move toward each other. There is also much less detail in the imaging spaces for indices less than –1 when compared to the index values above –1.

CHAPTER 6: IMAGING EXPERIMENTS II

6.1 Microwave Experimental Test Setup

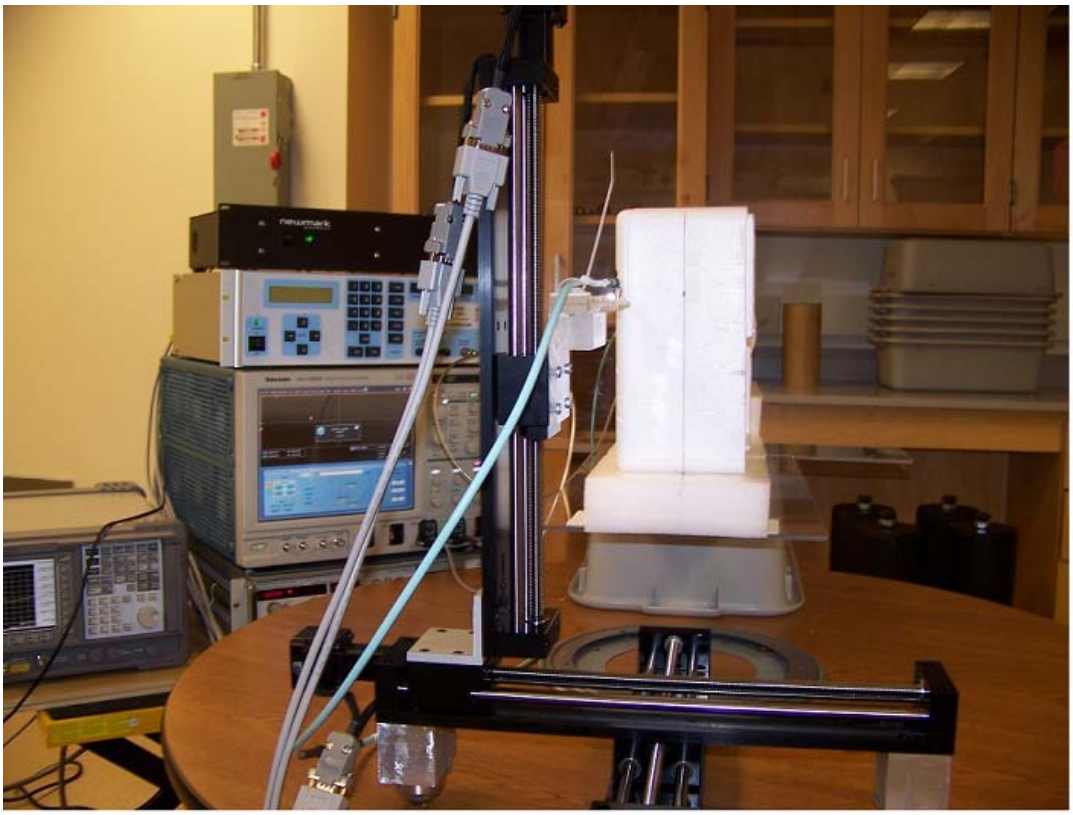

FIGURE 51: Computer controlled 3-axis microwave field measurement

FIGURE 51 is a photo looking straight ahead into the plane wave transmitter. The vertical line inscribed on the back face of the Styrofoam enclosure represents a central plane reference that aligns with the x and y coordinate plane. Propagation from the transmitter is along the x-axis, which is parallel or coincident with a perpendicular view.

directly into the plane of the photo. There are some additional details about the equipment seen in FIGURE 51 that would help to further understand what exactly is involved with this experimental test set. This setup begins with a microwave signal generator in which the output is connected to both a collimator and spectrum analyzer. Purpose of the collimator is to provide a reasonable plane wave formation for use as the excitation. Spectrum analyzers simply quantify the output from the generator in terms of frequency and power given that the generator can only provide a coarse indicator of power and frequency. Next there is the three axis translation stages that provides x, y and z placement of the field intensity measuring probe used to sample field radiation. In this specific photo there is also a real-time scope intended to measure both transient and continuous field variations resulting from the applied excitation. What's unique as well about the above seen test setup is that it can produce short burst of energy pulses by the incorporation of a picosecond pulse generator and a microwave mixer. One last capability is that all the mentioned components have the computer interface provision to allow computer control. Computer controlled test systems have the inherent option of synchronizing a coordinated effort to excite and capture the scattered response of any object placed between the transmitter and receiver, where the receiver in this case is the spectrum analyzer. Last point about the specific system being described is that it is referred to as a real time acquisition test system in that any event from inception will be captured and immediately processed for display given that at the time of this design the scope was deemed the fastest available in the world as was and still is today the picosecond generator.

CST provided both the numerical and experimental guidance early on, by designing the test set to mimic CST, which in turn helped in verifying theory and the simulation analysis. CST is setup-using standard x, y and z right hand coordinate systems. There are five aspects of the CST setup that were adjusted to mimic as closely as is possible the real experimental situation within the physical computer constraints on memory and processor performance. From an experimental point of view, power, frequency, polarization, coordinate alignment and background all clearly influence the measured results. These are the parameters that can be adjusted in CST in order to better replicate the experiment. Realistically our operational frequency range is between 7.5 and 12.5 GHz, with our interest being between 8 and 10 GHz. Input power can vary from one milliwatt to as high as 10 milliwatts. This can vary further depending on the background medium characteristics and the field measurement (x, y and z) position. Variations of input power can be measured for a prescribed area or plane and then compared later on to the actual measured values and the differences would provide the data for analysis. Polarization can be very closely maintained in terms of antenna placement and orientation. Coordinate alignment requires precise mapping from source to target position. In other words if the propagation is along x then placing the probe correctly in the y and z plane for a specific x value presents another element of ambiguity. Background structures can introduce unwanted reflections that under some circumstances could interfere with deciding if the device under test is responsible for the measured image field. Consequently, all of these concerns must be taken under consideration when interpreting the measured field intensities. To further help eliminate these aspects of uncertainty; the computer controlled test set can repeat the measurements more than once

under different circumstances to verify whether the results are solely due to the device under test. Here is another view of the test set seen in FIGURE 52, from a side profile to show how the test is aligned with the device-testing region.

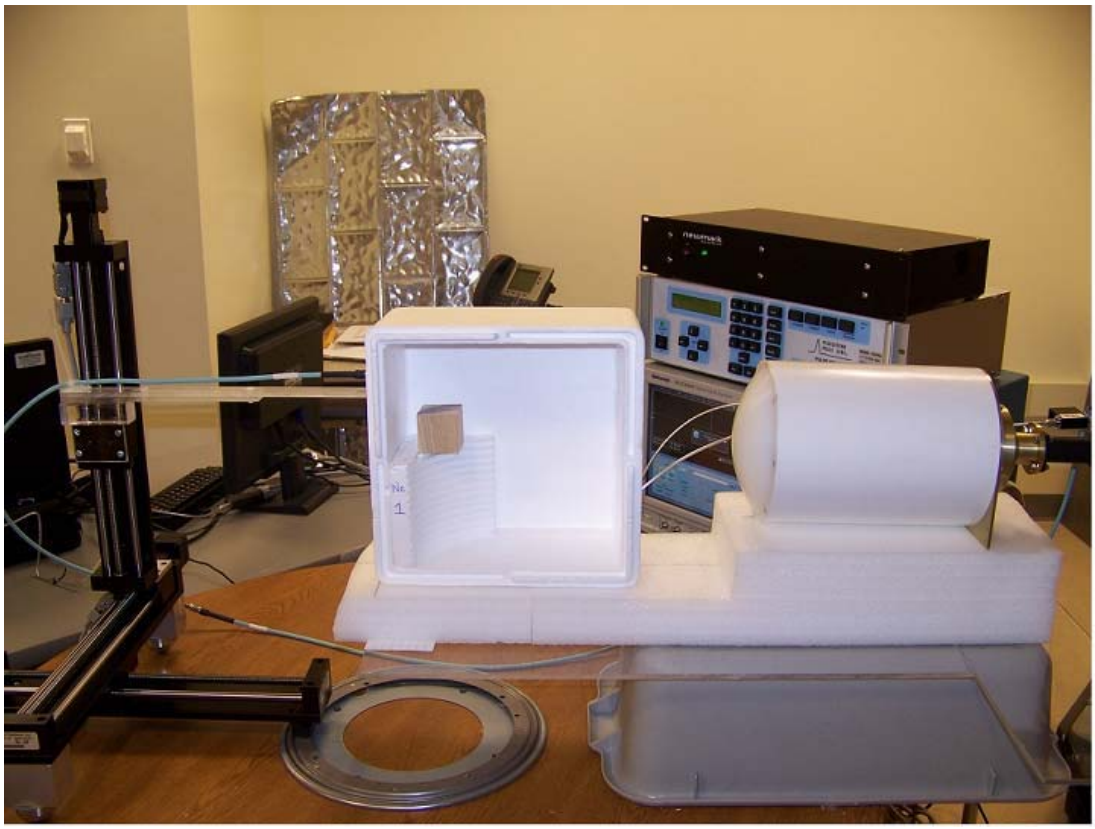

FIGURE 52: Side view of receiver on left and plane wave transmitter on right

6.2 Image resolution differences between Drude, Real and Typical Lens

In this chapter, Figures 53 and 54 show a comparison between an ideal Drude model negative index medium and one designed using the metamaterial constructs described earlier. Here a typical positive converging planar convex lens will be depicted as both a focusing lens and an imaging system at three different frequencies. Primary reason for this introduction is to provide a direct one to one correspondence with respect to

FIGURES 35 through 39 that present imaging performance using the planar meta lens. Lens. Using this 60 mm diameter, dielectric lens of $\varepsilon = 3$ and $\sigma = 0$ with an approximate thickness of 15 mm is comparable to the ideal Drude model microwave meta lens with an approximate thickness of 20 mm and equivalent 60 mm diameter. Objective here is to observe basic relationships of focused waves along with imaging formation. The object mask being used here is also equivalent in size, shape and 16 mm slit width compared to the double slit used with the meta lens. Points to hold clearly in mind given this positive converging lens is that with a symmetrical object placed outside of the focus approximately 35 mm at 60 GHz to the left of the lens ought to result in an inverted image on the right side of the lens. Having a symmetrical object shape allows for two possible placements here. First above the axis, single slit, second below the axis, double slit. With a positive converging lens it's expected that the image may be inverted and magnified to some extent depending on actual resulting parameters. Now with conventional thin lenses used at optical frequencies, assuming in a vacuum and a possible spectral width of approximately 400 to 800 nm there an estimated seven orders of magnitude difference between the wavelength and the dimensions being used here. This type of relationship allows for a helpful paraxial region to minimize convergence errors due to in part to the geometrical nature of construction. This will not be the case here however; the difference between dimensions and wavelength at microwave frequencies is at best a facto of 12 if using 60 GHz. So keeping the object close to the axis will now offer noticeable significant help with image resolution. This makes for a fare comparison between the types of lenses being evaluated. Another point to consider is how a conventional thick lens forms a waist and not a focal point. This reality will be observed

in all cases without exception. Remember that lens being symmetrical about the axis will help when comparing specific circumstances such as object above and below the axis. Three frequencies were chosen, which is one more than the meta lens circumstance just to offer a midway point of examination to further help the analysis by showing the response at an additional frequency. Chosen frequencies begin at 20 GHz for FIGURES 53 through 55, 40 GHz for FIGURES 56 through 58 and 60 GHz in FIGURES 59 through 61. The following FIGURES are divided into three frequency categories and present three different situations. First being a clear demonstration of plane wave focusing to the predicted focal region. Second a single slit mask with the object located above the axis on the left will be shown following the lens focusing. Third is a double slit with both objects placed equally above and below the axis. Analysis will consist of a brief commentary based on observable results without any speculation. The same impartial critique will be applied to the following criteria. There are four aspects in review here that will be used as a minimum gauge of performance. One is clearly focusing, waist size, image location and distinguishable resolution if possible. Each brief response to the FIGURES will be with reference to the four specified responses

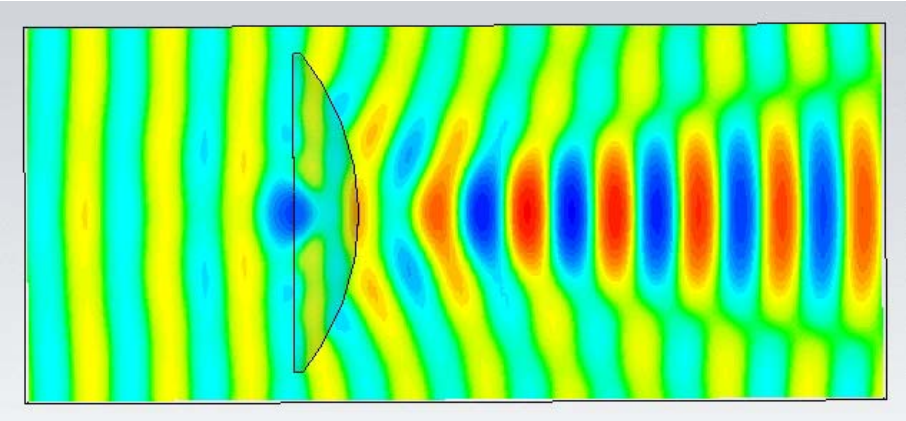

FIGURE 53: 20 GHz plane wave being focused by a planar convex lens

Figure 53 shows at 20 GHz a clear extended focal region, with a waist size that is not easily seen here due to the view being truncated for this longer wavelength.

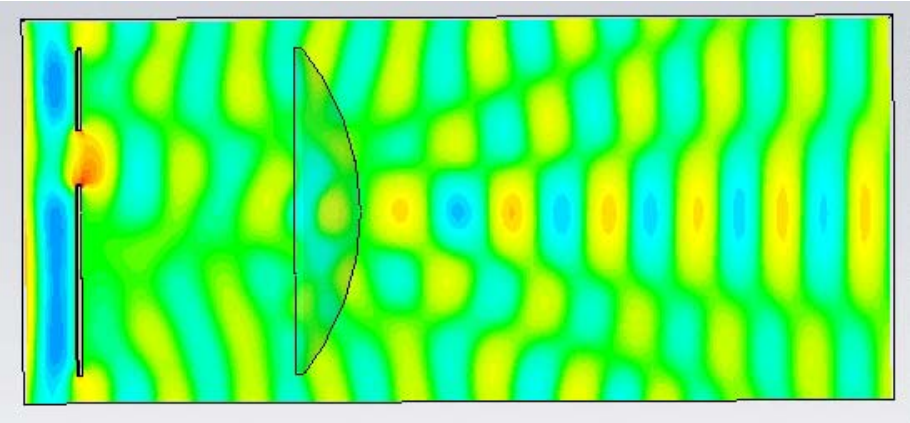

FIGURE 54: 20 GHz plane wave passing through a single slit object

Figure 54 depicts at 20 GHz plane wave transmitted into a single slit placed above the axis and to the left of the lens focus, being used an object. Focus appears to be diverging immediately in front of the lens. Waist size, image location and resolution are not observable.

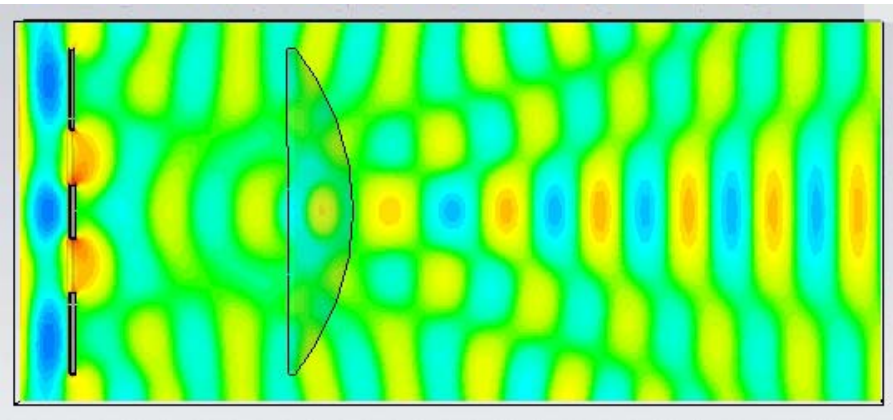

FIGURE 55: 20 GHz plane wave passing through a double slit object

There is not much more to add in regard to FIGURE 55 given it follows FIGURE 54.

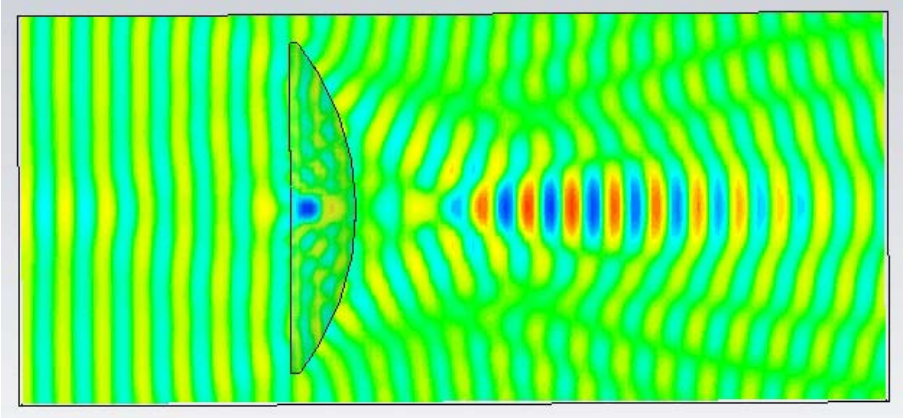

FIGURE 56: 40 GHz plane wave being focused by a planar convex lens

Figure 56 shows at 40 GHz, a clear extended focal region, with a waist size that is almost twice the lens thickness. Imaging is simply the focused formation and resolution is estimated as being close to 8 mm, which is roughly the central spot size.

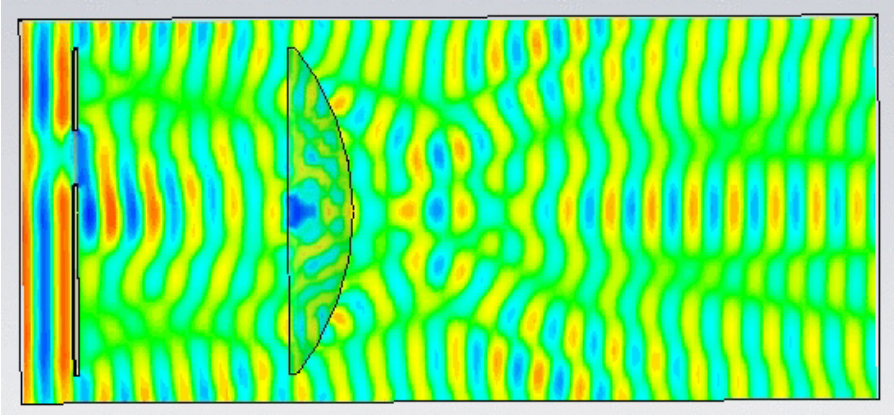

FIGURE 57: 40 GHz plane wave passing through a single slit object

Figure 57 depicts at 40 GHz a plane wave transmitted into a single slit placed above the axis and to the left of the focus, being used an object. Focus appears to be converged into a region more than twice the lens thickness. Waist size again estimated to approximately 6 mm, image location and resolution is not easily discernable.

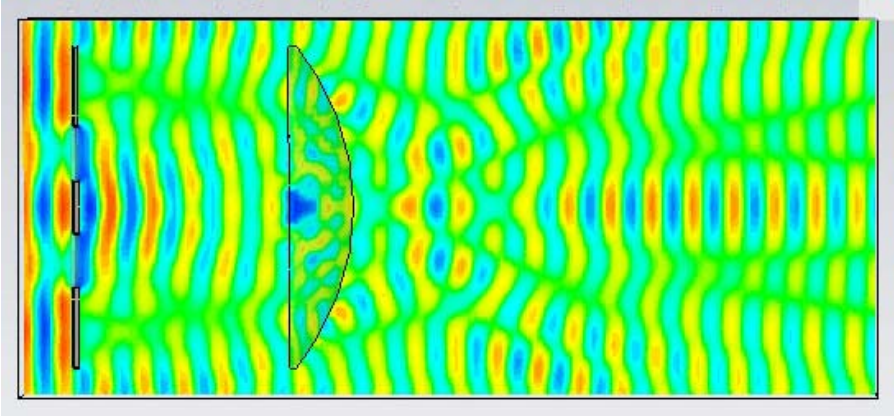

FIGURE 58: 40 GHz plane wave passing through a double slit object

Figure 58 depicts at 40 GHz a plane wave transmitted into a double slit placed above the axis and to the left of the focus, being used an object. Focus appears to be converged into a region more than twice the lens thickness. Waist size again estimated to approximately 6 mm, image location and resolution is not easily discernable.

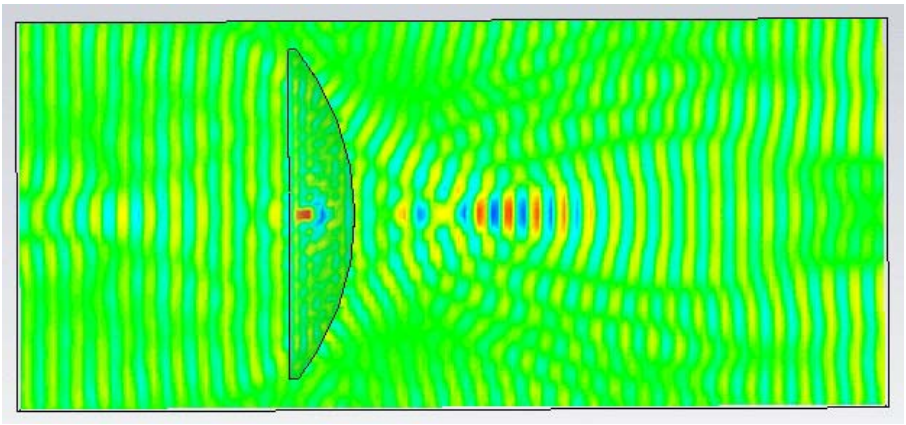

FIGURE 59: 60 GHz plane wave being focused by a planar convex lens

Figure 59 shows at 60 GHz, a clear focal region with minimal extent, waist size that is close to the lens thickness. Imaging is simply the focused formation and resolution is estimated as being 3 mm, which is roughly the central spot size relational to wavelength.

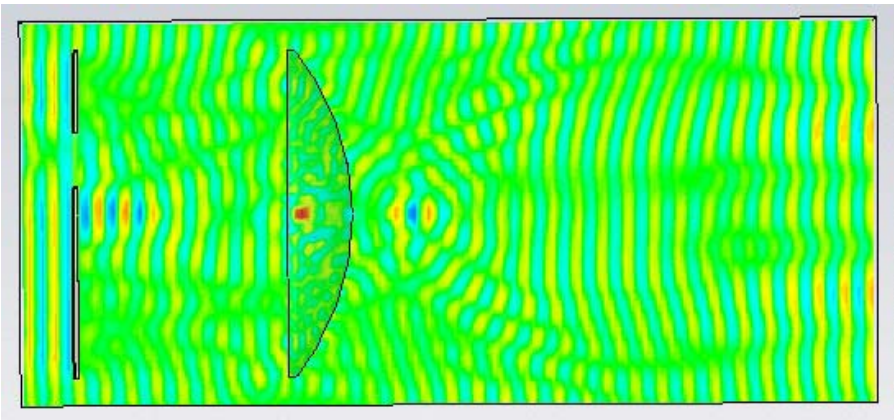

FIGURE 60: 60 GHz plane wave passing through a single slit object

Figure 60 depicts at 60 GHz a plane wave transmitted into a single slit placed above the axis and to the left of the focus, being used an object. Focus appears to be converged into a narrow region less than half the lens thickness. Waist size again estimated to approximately less than lens thickness, image location and resolution is now becoming somewhat discernable, approximately to the right of the focus on the right side and below the axis is being thought. Resolution as expected given the shortened wavelength has become improved but not easily quantifiable. Here it is worth noting that resolution size of the image may not be clear given the nature of magnification. This circumstance is difficult to qualify in view of the observable graphic image FIGURE 60.

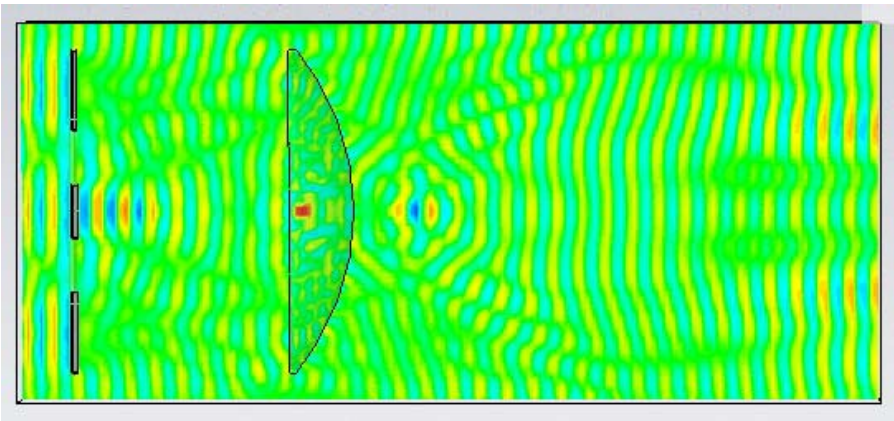

FIGURE 61: 60 GHz plane wave passing through a double slit object

Figure 61 is basically similar to FIGURE 60 in respect to focusing and waist size and somewhat different in respect to imaging in the following way. It appears that there is a symmetrical formation above and below the axis comparable to the input objects location and sizes but there is still not any clear distinguishable line that could be drawn to suggest precisely where the image formation begins and ends.

In brief summary regarding these three displayed categories of conventional dielectric lens the following becomes clear. Higher frequency or shorter wavelength improves spot size and reduces the observable waist. Image formation and resolution is undetermined due mostly to graphical ambiguity and the limited extent of analysis. Even so, this is an equivalent comparison to the ideal planar meta lens. Given a choice, it would seem that if a –1 index could be realized then the planar lens would be chosen based on the following parameters. Low frequency high resolution, focus point not waist, strictly planar geometry and the possibility of perfect imaging with low material loss.

6.3 Image Resolution Estimation

A few words about Figures 62 and 63 will help explain the subtle aspects in common between ideal and actual simulation model. FIGURE 62 does exhibit a –1 index as can be seen from the wavelength (i.e. spacing between wave fronts) within the negative index material. Closer examination of the left side of the negative index structure illustrates that there is a buildup or enhancement of fields close to the input surface, which is also seen in FIGURE 63, and expected because of the index mismatch at the boundary. Both models have continuous backward waves except that in FIGURE 63 the internal wavelength demonstrates a -.5 index. Both models have the same volume but differ in

the real negative parts of their permeability by almost 40% and are within 12% of their target permittivity being -.79. These values result from a recursive process of holding either the permeability or permittivity fixed while adjusting associated geometrical and material parameters.

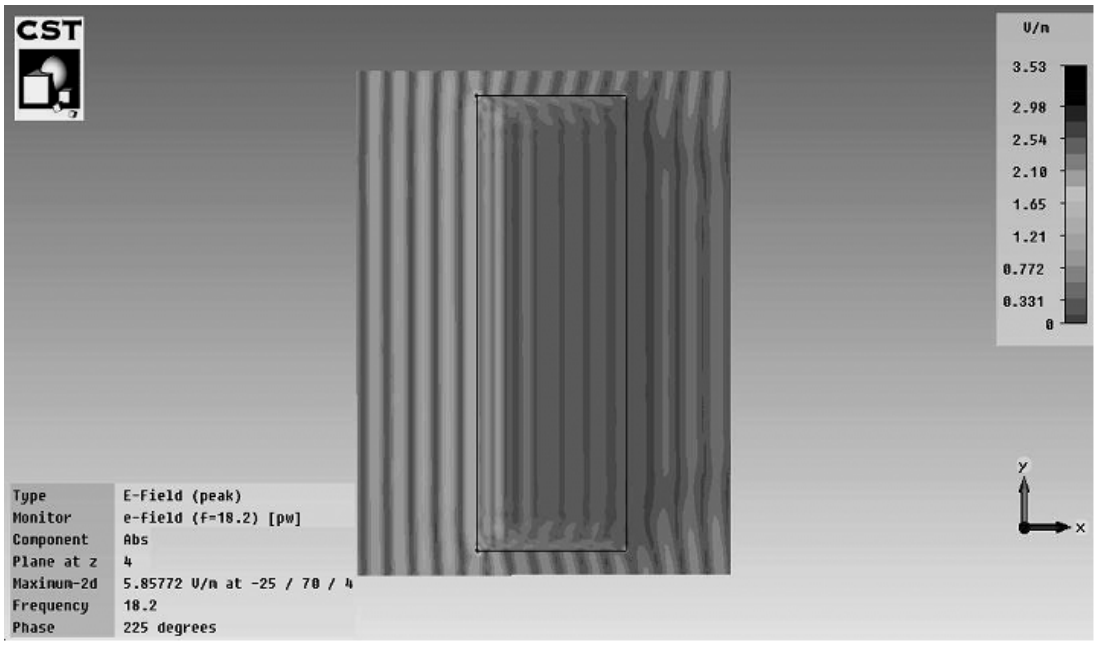

FIGURE 62: Ideal Drude model having a –1 index

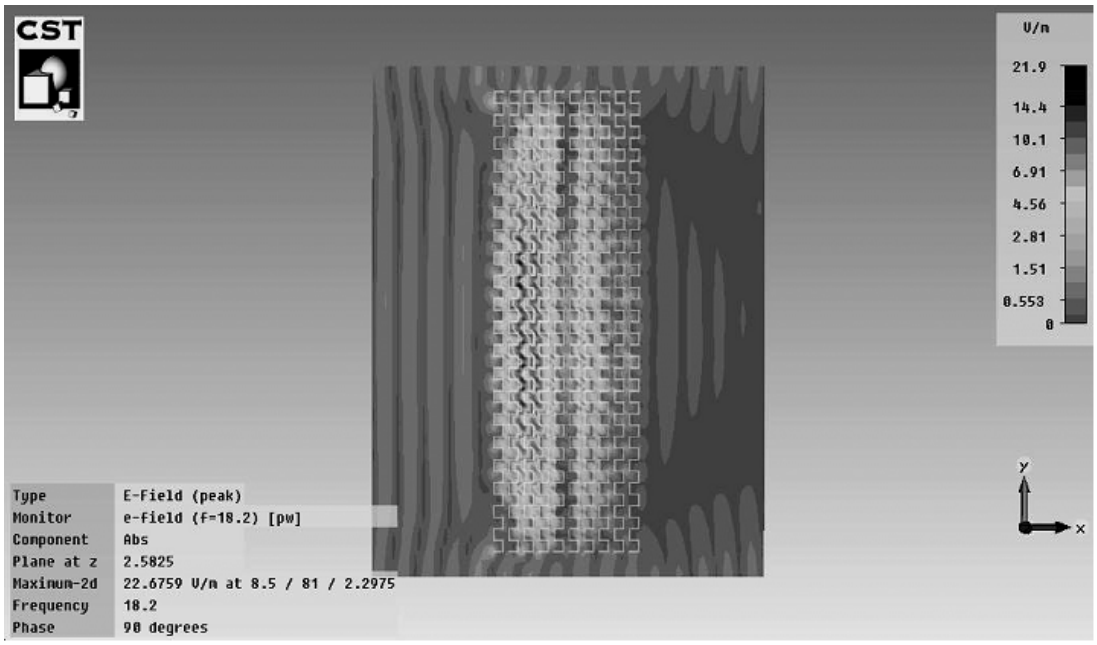

FIGURE 63: Designed model having -.5 index

In FIGURE 63, internal wavelength is estimated by choosing the first discernable peak in volts per meter away from the left side compressional edge effect, which can produce a index result lower than expected. The next location moving left to right where there is a repeat of the field peak occurs to the right side of what appears to be a gap between the wavefronts.

CHAPTER 7: FINAL EXPERIMENTS

A final round of simulations was conducted in order to attempt to quantify the improvement in resolution possible with lower loss metamaterials having an index approaching = -1. Actual resulting values of permittivity and permeability used in the ideal Drude model design were different for different frequencies. To further understand the details FIGURE 64 has been included here and will be explained.

Frequency GHz	Permittivity Real Part	Permittivity Imaginary Part	Permeability Real Part	Permeability Imaginary Part
10	-0.99491776	0.31596	-0.99491776	0.31596
20	-1.0005136	0.159	-1.0005136	0.159
60	-0.9997491	0.053	-0.9997491	0.053

Frequency GHz	Loss Tangent Tan	Dimensionless		Lens Thickness 20
10	$\tan\phi = \frac{\varepsilon''}{\varepsilon'}$	-0.317573987		
20		-0.15891838		
60		-0.053013301		

Frequency GHz	Resolution Limit mm	Spot Diameter mm
10	$\Delta = \frac{2\pi d}{\ln\left(\lvert\varepsilon''\rvert\right)}$	11.78439874
20		9.327960796
60		7.380295685

FIGURE 64: Depicts permittivity, permeability, loss and resolution limit

Designing an ideal negative index metamaterial using the Drude conductivity model involves minimizing loss for each frequency and thickness. Three frequencies were investigated along with a fixed thickness in an attempt to optimize the imaging performance. As can be seen in FIGURE 64 each frequency associates to both the real

and imaginary parts of permittivity and permeability. With these constitutive parameters also comes the reality of loss expressed as the imaginary parts of permittivity and permeability. Loss introduces two issues, one reduced transported energy and two, limited resolution. From the table it can be seen that these issues were minimized at 60 GHz. For example, the spot diameter limit at 60 GHz is 7.38 mm approximately. This suggests that diameters less than 7.38 mm may not be easily resolved if at all given the real loss. The conclusion here is that the real loss is responsible for the absolute ideal characteristic responses being reduced.

Not exactly realizing n = -1 does not affect the potential for high resolution imaging, since some evanescent waves may be captured by the negative index structure and that information conveyed to the image plane. Computational image reconstruction methods might be necessary to improve the appearance of the resulting image if the anisotropy of the metamaterial, dispersion and background noise affect image quality.

We have established that a conducting medium such as metal is both helpful as well as problematic (i.e. attenuating) in the design of negative index metamaterials. Metal is helpful because of the needed magnetic effects produced by induced current variations. Resonance control from a magnetic and electric energy density prospective involves metal in all of our models so far.

7.1 Conductive liquid model simulations and applications

We note that conductivity is fixed in solid materials but can be variable in some liquids. The possibility of simulating variable conductivity fluids can be accomplished by using CST. We have demonstrated using CST that with liquids or ionic liquids in the

proposed S structures, it is possible to realize a backward wave phenomena but the losses, while diminished still remain an ongoing issue of further research work. A significant advantage of using a liquid in our metamaterial is that a variable conductivity allows one to tune the index value and possibly get closer to -1 in a real structure in which the many elemental circuit elements do couple together and experience fringing effects.

Indeed, using controllable ionic liquids is a means of achieving a tunable micro-fluidic metamaterial giving flexibility in diverse applications. Frequency tuning and reduced loss structures present an attractive alternative to otherwise rigid metamaterial structures that may not work experimentally without the ability to provide some tunability.

Though low loss and tunability help in producing some approximate meta model candidates for imaging, effective medium approximations still must be considered. To accomplish this, the resonator sizes have been reduced but remain comparable in size to the internal wavelength. Nevertheless, simultaneously the conductivity and geometry can help scale the resonant frequency lower while reducing the unit cell period. Further investigation has lead to equation (98), $RC = \frac{\varepsilon}{\sigma}$, a general result showing how the product of resistance and capacitance relates to inverse conductivity, which is also directly related to current. In electromagnetics it is seldom possible to make direct measurements of capacitance. In many cases capacitance is indirectly measured by current and in some special case electrostatic differences. Recall that Ohm's equation (68) expresses total current density as a product of conductivity and electric field. Imagine that the magnitude of the electric field is normalized to one. This shows that the

total current density is proportional to conductivity (σ) Equation (98) relates inverse conductivity to effective capacitance, the capacitance of the unit cell. One way to interpret equation (98) is as follows, capacitance inversely follows conductivity and this would suggest that as current rises capacitance would decrease. If the capacitance decreases then the resonant frequency will shift to higher values. Therefore when total current rises so does the resonant frequency. With these thoughts in mind adjustments were made to the new design by decreasing the metal thickness by a very small amount while the effect was throughout cumulative. This experimental trial resulted in a lower frequency shift while the periodic width of the elements in the structure was preserved. This translates into better alignment with the effective medium approximation due to the fact that the internal wavelength was comparatively longer than the unit cell by approximately four periods, which is an improvement over the previous example of approximately 10 percent. Qualitatively speaking and as stated earlier, when the elemental unit sizes are reduced there is an observable tendency for the resonant frequency to shift higher, simultaneously moving away from sub wavelength scale structures and compliance with an effective medium theory. However in the case just described the cell size was preserved while the frequency was shifted lower. Also worth noting was that this incrementally small change also demonstrated a noticeable improvement in the backward wave phenomena. The new model demonstrates that even when reduced in length by several periods (or another way of stating this is that when a number of sections are systematically removed from the negative index structure) the simulations still demonstrated smooth continuous backward wave phenomena even down to the single unit cell consisting of just two metal S patterns. Clearly it has been

conductivity that has proved to be a most essential parameter for more convincing demonstrations of a negative index material.

The use of conducting liquids also demonstrates that the effective bulk index can be also changed from negative to positive over a specific range of conductivity. The conductivity that led to the index variability was several orders of magnitude below that of most conductive metals, which was in the range between 800 and 800000. In this range the index would vary from negative to positive. It's further helpful to remember that lower conductivity associates with lower losses and therefore improved resolution if we follow Pendry's resolution equation that shows how losses quickly diminish resolution.

7.2 Final S model designs for experimental testing

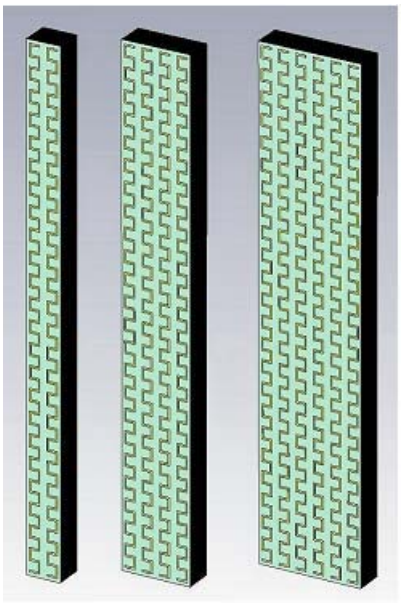

FIGURE 65: Final three experimental models

Three basic models consisting of an equal number of stacked circuit boards having matched height and different widths along the direction of transmission have been

constructed for experimental tests and these are shown in the above FIGURE 65. One design for use as a holding platform to support the various experimental models is illustrated below.

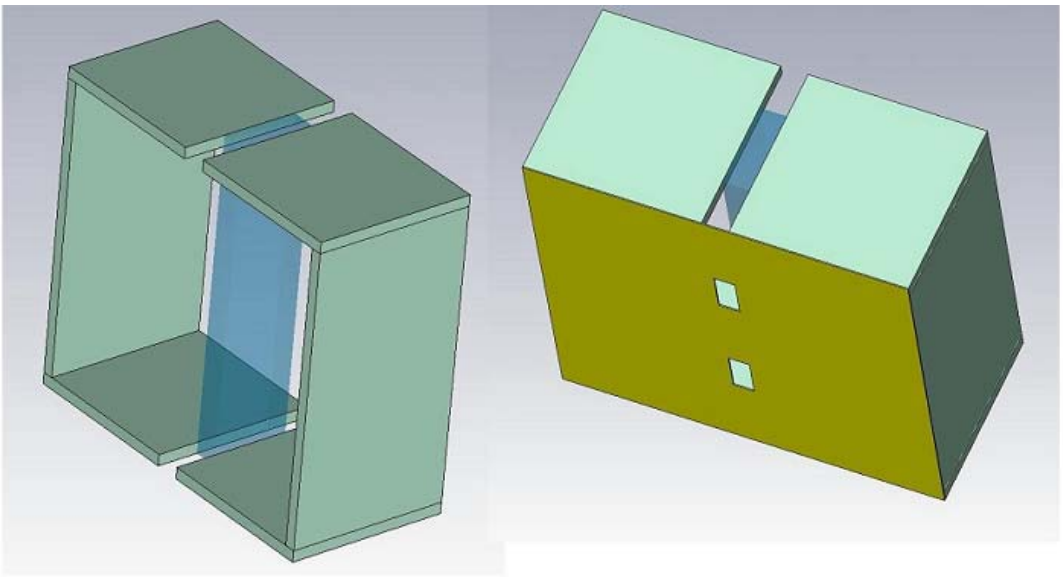

FIGURE 66: Variable size test holder with and without mask

This test platform allows the negative index structures to be placed in the blue central region as well as allow for a double slit mask to be placed in front of the structure.

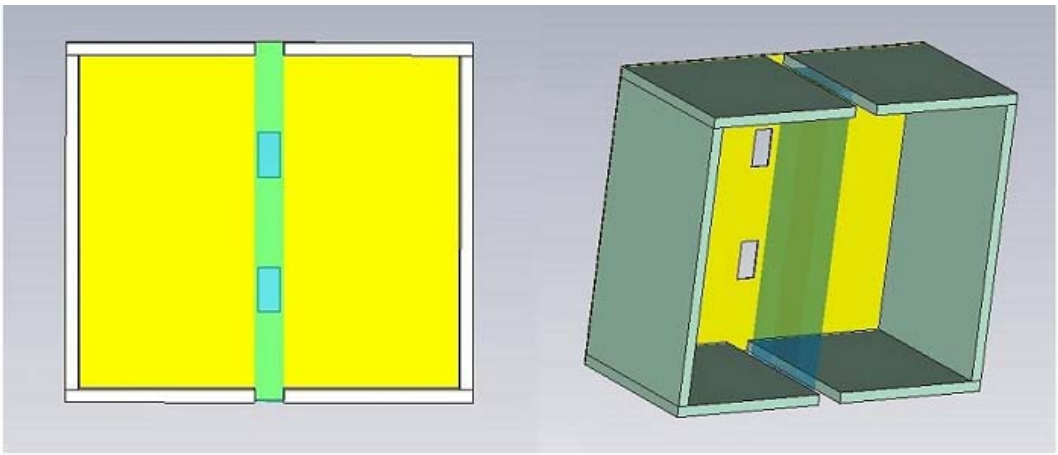

FIGURE 67: Test platforms depicting double slit illumination

These design submissions have evolved from extensive simulation experiments of microwave based abstracted circuits derived from first principles as outlined in the basic theory of John's model design. Simulated results have demonstrated backward wave phenomena and negative refraction that was compared to the ideal Drude model cases used as reference standards. The Drude model has clearly demonstrated negative refraction, backward wave phenomena, total internal reflection leading to evanescent analysis and finally numerous imaging results. Conductivity has provided the needed guidance to understand the subtle intricacies involved in both estimation and calculation of Resistance, Capacitance and Inductance. Conductivity has also provided the basis upon which the Drude model was used and resulted in successful imaging and demonstration of negative index materials. Conductivity has also provided the means, by which to introduce index variability from negative to positive, which led to, a design submitted for patent provision. Applying conductivity theory in conjunction with certain geometrical shapes has resulted in periodic cell size reduction leading the design closer to effective medium theory approximations. One measure of an effective medium is homogeneity. It was suggested that if the volume structure did in fact have a small enough unit cell size then the removal of repeating sections would not introduce and noticeable behavioral change from intended design task. This new design has achieved equivalent performance at lower frequencies while preserving unit cell size at or below the comparable internal wavelength. The central point here being that effective conductivity can further aid the process of effective medium approximations as has been demonstrated by simulations. CST has provided a platform upon which the reality of the actual experiment can be closely approximated as was shown with three actual

consecutive experiments. The CST results were in excellent agreement with the measured data.

7.3 Final Imaging Experiments

Based on the modified version of Kong's S model a new S model design was fabricated with three different lens thickness or widths, using low permittivity circuit boards with S patterned copper traces. These different thicknesses will be referred to as 2S, 4S and 6S throughout this discussion, all other dimensions are equal. CST provided the primary guidance during design and test. Each experimental result will be displayed along with CST simulated results. With any real experiment there will be circumstance aspects that are not included in the ideal simulated case due mostly to computer memory limitations and available material libraries for the x-band frequency range being used.

In all experimental setup cases there will be a collimated plane wave excitation positioned approximately 1 meter away from the model under test, which will be held by a test platform designed to support the 2S, 4S or 6S models as shown in figure 68.

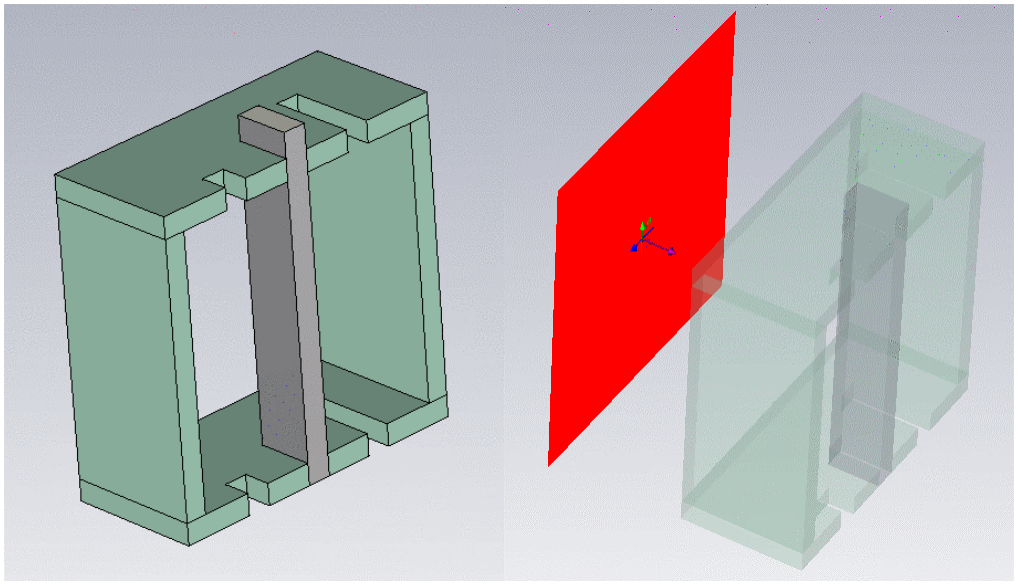

FIGURE 68: Test fixture used to investigate the model characteristics

For the case where a mask is required in front of the test model, a sliding Styrofoam backing board was cut to fit within the supporting walls of the test platform. On the backing was placed an aluminum sheet with the prescribed cut outs or slits and this formed the mask as seen in figure 69.

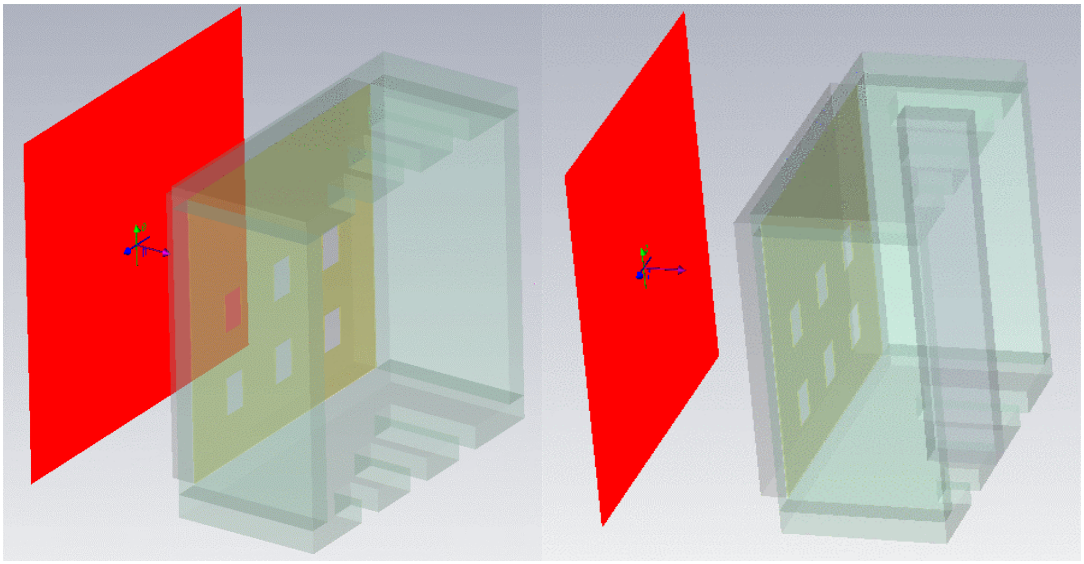

FIGURE 69: Modified test fixture with a movable mask for use as imaging objects

There are two frequency categories, which are 8.5 GHz and 8.0 GHz. In accordance with CST all three models demonstrate a smooth continues backward wave phenomena at 8.0 GHz and at 8.5 GHz while beyond 8.5 GHz CST shows positive going waves. The main objective for these final experiments is imaging using negative indices as closely associated with -1 and these two frequencies provide the closest possible association and this is why they were chosen.

It must also be made clear that CST has shown approximately a -.8 index based on the comparison between internal and external wavelengths. At 8.0 GHz is where the index is believed to be closest to -.8 and reduced at or above 8.5 GHz. The models also

demonstrate improved effective medium characteristics in two ways. First is the ratio of the unit cell period to the internal wavelength, which approximates a factor of 4 at 8.0 GHz and close to 3 at 8.5 GHz. The second way to estimate the effective medium approximation is by homogeneity, which is clearly demonstrated by decreasing the thickness and or removing sections and still being able to observe the continuous backward wave phenomena.

Some additional comments about the test structure seen in the above FIGURES 68 and 69 are as follows. The backing board can be positioned in units of millimeters. This allows for precise object placement in front of the designated model. Also as can be clearly seen the structures are surrounded on both the left and right side by the background air, which minimizes any inter action between fixture and device under test. The entire test platform is made from styrofoam and has an index closely approaching that of air and therefore provides a good matching impedance to lessen the degree of unwanted reflections. Styrofoam is almost completely transparent at microwave frequencies, which is the reason to choose as the support backing underlying the metal foils being used as the double slit mask.

Further explanation about the purpose of these experiments will help in view of the fact that none of these models were shown to demonstrate a -1. Earlier several figures were introduced to show how the imaging performance of an approximate ideal model, even with negligible loss was affected when the index was other than -1. There were two cases to show that an index above and below -1 would have less than the perfect image. In fact as the index neared -1 the image approached the best possible representation,

almost perfect. It was suggested that the factor preventing ultimate perfection was due to a very small loss. With this in mind the idea was to investigate any imaging possibilities by performing an exhaustive battery of experimental test at two different frequencies, with and with out objects, along with characterizing the background measurements to eliminate any possible noise contributions. Each experimental test has a duration of approximately 10.3 hours and collects within the limits of the available test equipment exactly ten thousand measurements needed to perform the equivalent comparison to CST to further show consistency. Shown below in FIGURE 70 is a table outline of the tests that were performed to evaluate the 2S, 4S and 6S models.

Freq GHz 8	Freq GHz 8.5
Background	Background
Mask	
2S	2S
4S	4S
6S	6S
2S Objects	2S Objects
4S Objects	4S Objects
6S Objects	6S Objects

FIGURE 70: Outline of fifteen experiments included in this final experiments section

In the 8 GHz column there were eight different measurement test and seven in the 8.5 GHz column. Transmission power is the quantifying parameter to assess performance and behavior. Where it lists the model 2S, 4S or 6S, this is taken to mean testing without objects and with the word objects means the imaging characterization test. This type of test is conducted with a young's double slit as a mask behind the test structure as seen in above FIGURE 69. So whatever is placed between transmitter and receiver becomes the

measured parameter. CST has simulated all the above listed measurement parameters to provide the necessary comparison to help in the analysis process.

As with all experimental test there is a degree of realistic expectations given the differences between real and simulation. Objective of these experiments is to compare actual measured data with CST simulation results and to employ graphic analysis of the measured data by visually comparing how the measured data varies with and without objects. These differences between the real physical setup and ideal case simulations require a brief discussion.

7.4 Differences between physical experiment and CST simulated experiment

Source excitation is a generator that can provide a stable continuous GHz frequency in the range of 8 GHz to 12 GHz within plus or minus 20 MHz. CST idealistically will have zero percent deviation about the select frequency and the generator can deviate by as much as two percent. Case example, 8.5 GHz, could deviate to as low as 8.48 GHz and as high as 8.52 GHz. Actual measured data to verify this possibility shows the lowest deviation was 8.4915 GHz, which is closer to a 10 MHz deviation than what the manufacturer suggest. So 100 sample data points were taken and the range was 8.491 to 8.4915 GHz, which is within 1%.

Power is set to 10 dBm (10 mw) and this value can vary by as much as -.2 mw given the unknown impedance mismatch. Using direct measurement of power by a spectrum analyzer will have loss associated with the cable and connectors. Typical deviations of standard non-impedance matched cables can introduce approximately 3 percent variation. Using another method by which to verify the indicated power was by using low loss

match cables and the actual measured value was 9.85 mW and this result shows that the generator is within two percent. One important point to remember here is that regardless of the actual absolute power or shift from indicated value, as long as the power remains constant then this becomes a reliable relative reference.

CST provides a uniform plane wave in accordance with theoretical models, which is perfect. The generator on the other hand produces waves based on the type of antenna construction being used for the transmitter. Typical dipole antennas can be configured to launch spherical waves, so when measured far enough away resembles an ideal plane wave. The difficulty with this measurement is that when the wave has traveled any distance, amplitude will go as the inverse of the radius squared. To minimize the geometrical loss and still have a reasonably good plane wave formation, a microwave collimator was used. To test out this approximated plane wave a series of measurements probing the space, titled background measurement between the transmitter and receiver were collected and the results are shown in FIGURE 71. It will help to further explain these images being introduced here by emphasizing exactly what is being shown with respect to the launched waves. The figure on the left is the actual measure plane wave response at 8.0 GHz at the select location from the transmitter. Where the select location is the area the test probe samples. This area in all cases is prescribed as 10 by 10 cm or 100 mm square. Possible reasons for two different waveform responses associate to the microwave collimator having a cutoff closer to 7.7 GHz versus 7.5 GHz. Also the collimator is more closely aligned for the central region of the microwave x-band (8 to 12 GHz). These two images are to be understood as being the specific excitation related to

8.0 and 8.5 GHz respectively and will be clearly displayed with the corresponding measurement throughout this section of final experiments.

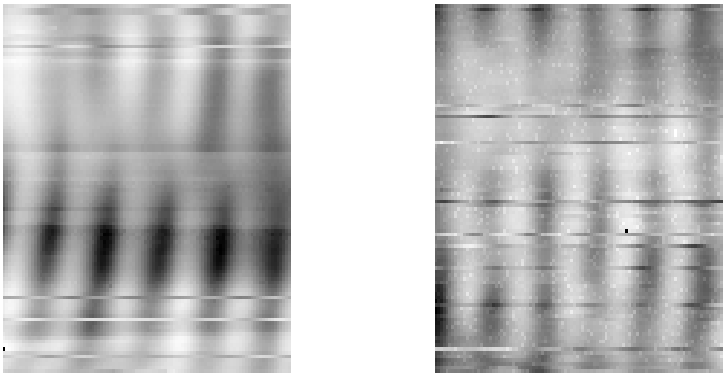

FIGURE 71: Background measurement of source radiation at 8.0 GHz and 8.5 GHz

The collimated source field measurements were taken at 8.0 GHz and 8.5 shown from left to right respectively. One possibility to explain the different appearance of these waves is the x-band response of the microwave architecture. The frequency cutoff is at approximately 7.5 GHz, which is a safe guard band. For this experimental setup it's understood that there will be variation of measured response depending on the frequency being used. So input and output association throughout the experiments will clearly show which source frequency is being used for the excitation. Last thought here is that when field measurements are being collected it's difficult to understand how the background contribution is effecting this power measurement. One way to minimize these types of uncertainties is to design and build an anechoic enclosure around all experimental components. Being consistent is another way to reduce the background uncertainty.

One other sample measurement was taken of the object mask to provide a relative reference to compare with the object measurements, taken at 8.0 GHz. This choice is arbitrary but yet favors the CST simulation that shows 8.0 GHz being the frequency with

which to expect the closest approximation to -0.8 index. The result of this field measurement through a double slit mask is shown in FIGURE 72.

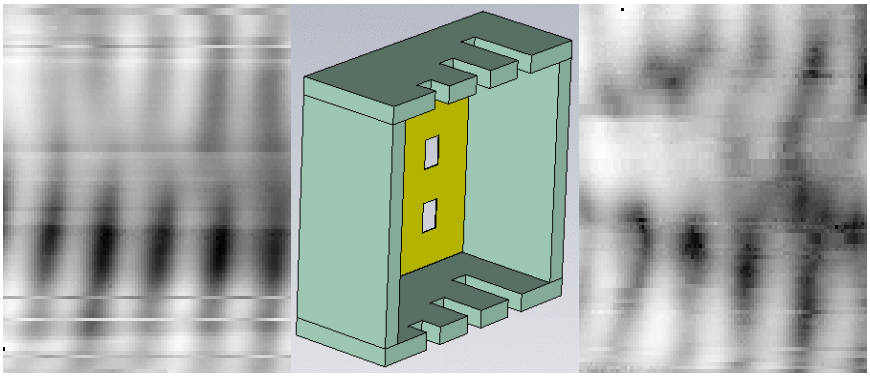

FIGURE 72: Sample measurement of the mask illuminated at 8.0 GHz

CST can also set the background conditions so that possible interference will not become part of the collected data. The background contributions will be observed during the plane wave evaluation and stored for future comparison. The underlying assertion in the actual experiment is that once the background has been measured then differences that appear in the measurement must be directly associated with the introduction of the test structure.

CST can also depict visually and mathematically how the wave is behaving internal to the structure when in reality this would not be possible with the actual experiment. Using direct measurement of the emerging field data is what remains to decide how the test structure affected the wave transition between entry and exit. Two possibilities exist to help in the analysis given this reality, one is refraction but that would not help in the imaging analysis, so what remains is to be able to quantify the space precisely before and after the introduction of the test structure, with and without object waves. While it is correct that the simulation can demonstrate backward wave phenomena this can only be

taken to reflect a negative index and if the index is within an acceptable range for our imaging task, which is in our case -.65 to -.85, then this is helpful. This range of index while not exhibiting a -1 may still show some imaging behavior but CST did not demonstrate this. Recall that the objective is to approach CST simulated results; the importance of this is central to establishing reliable guidance in the pursuit of -1.

Last salient point of difference is between the measured field data and CST calculations of the grid values for the region being explored. With the actual experiment there are three degrees of freedom that must be minimized to obtain reliable results. First is that however the probe is being used to sample the data it must be consistently followed. Second the spectrum analyzer must have enough sample time to obtain a steady state average at the prescribed position. Third the probe settling time into position must be long enough to dampen any residual oscillatory movement resulting from the transition between locations. Spectrum analyzers have ranges of reliable signal measurements that must be followed as well. For example if there were three scales from which to choose for use in the measurement, the choice is made by re-evaluating the signal closest to the central or middle of the scale. All these factors taken into account will further help in the interpretation of real measured results.

7.5 Collection and processing of signal data

All data measurements have an x, y and z spatial coordinate to uniquely identify the measurement. In these experiments the excitation waves are traveling from source to receiver. This setup is in part decided by the physical constraints of all the required equipment. Each point in space has a defined uniform separable spacing, which is 1mm

and was decided upon by comparing the measurements over decreasing incremental values along x, y and z. To a first approximation there is a quarter wavelength minimum antenna probe length that translates into 7.5 mm at 10 GHz and this antenna wire is then matched by 6 mm sleeve for optimal flat response. This now leaves 1.5 mm of sensitive probe, so 1mm was chosen for the separable space; any smaller and there is not any observable difference in power density. Collected data is organized into a grid or matrix of values for use in presented results. This grid will be processed into an image by scaling the data in accordance with an intensity scale to clearly depict power density variations in respect to the weakest background. Applying an objective basis of analysis is somewhat reduced with graphics but the actual data in the area of interest has quantified values that can be quantifiably compared.

Further processing of signal data will be to investigate the power density within millimeters from the emerging test face. Approximately 3 to 5 mm away from test structure is where the probe begins to acquire power measurements; reason for variation is due in part to the mounting probe hardware. This data will be closely processed to prepare for the comparison of surface waves before and after the test structure. There will be an attempted correlation with respect to x, y and z coordinates of the object slits so as to further examine how signal data compares.

Before examining the experimental results it will help to have a clear picture of exactly how the field was probed in relation to the test structure. Briefly an antenna probe is positioned in front of the exiting face of any one of the models. The probe is

then repositioned within an area plane that is parallel to the sidewalls of the test structure and extended in both the vertical (up and down) in front of the selected model and then moved further away in the direction of propagation. With these comments in mind please refer to FIGURE 73 for a graphic illustration.

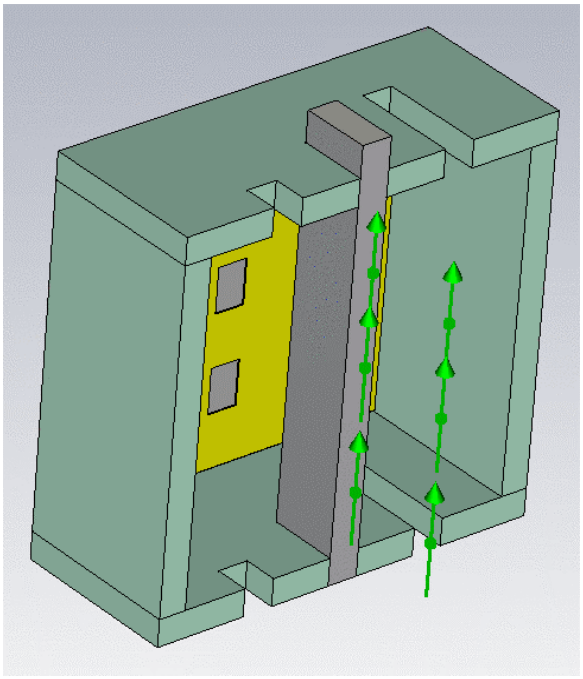

FIGURE 73: Outline of the test space being measured behind the test model

FIGURE 73 also shows a double slit in the background that can be adjusted either closer or further away from the input face of the shown model. It's this setup that mimics the CST simulation setup. The results that follow can be easier to think about by proceeding in the following manor. Each experimental result is portrayed directly below the simulated results for ease of comparison. The gray scale being employed can be interpreted as the brighter the shade, the higher the power density and vice versa. Though not easily seen, each model is composed of forty circuit board layers each having an identical patterned S printed on the surface that results in a two-centimeter depth.

Each structure is approximately two hundred and eighty one millimeters in height. The front to back thickness varies from approximately twenty-three millimeters to seventy-one millimeters. The slits have the following dimensions, three centimeters high, fifteen millimeters wide and are separated by approximately four centimeters. The slits are located in the lower half of the structures so as to have a distinguishable effect if one were observed. Last point before analyzing the results is to understand that some noise contributions seen in the resulting waves can be attributed to the exhaustive memory usage of the spectrum analyzer. In short, the analyzer must update more frequently than would otherwise be expected. This updating or active realignment of the front-end circuitry introduces erroneous measured data. There is not any convenient way to correct this behavior given that the analyzer uses windows based operating system, which is inherently slow compared to the direct memory access being used by the controlling computer. One other source of noise occurs when the positioning translation stage is interrupted from the analyzer update and this causes a temporary probe movement off the prescribed track. This type of irregular or unexpected behavior happens about four to five times in a ten thousand-point measurement on the average. Also please keep in mind that these measurements represent power, which is the square of the field divided by the spatial impedance when attempting to calculate the wavelength. The first set of results consists of both simulation and experiment of a plane wave entering and exiting the 2S model. The wave shown entering the experimental model was the actual measure of the source excitation traveling wave. To the right of the actual 2S model is the emerging plane wave. These images require slow and thoughtful analysis taking into account all

available points mentioned so as to objectively decide if the result makes consistent sense.

To further reinforce the comprehensive analysis, it's important to describe the physical test circumstance as it relates to the measurement space. For the case of an unmasked structure it helps to imagine the actual location of the plane wave with respect to the test space seen in FIGURE 74.

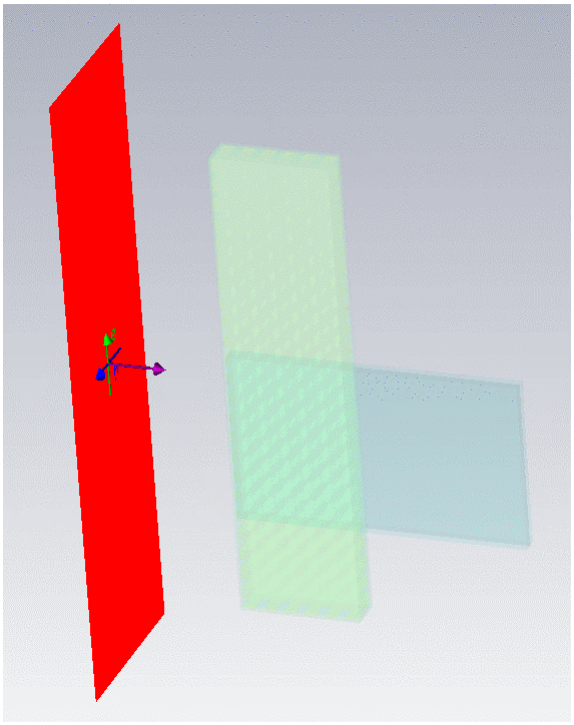

FIGURE 74: Plane wave illumination of model showing the test space in blue

Plane wave is aligned with the test structure and the sample region is shown in the darker blue area placed to the immediate right side of the test structure. Please note the extended darker blue area to the right of the 6S test structure in this case but it could be any model. This darker blue area represents the sampled power density measurement area. In each instance of experimental test the probe will be moved in this area.

Resulting measured data will represent the response for this particular test region, which has a physical size, 10 cm by 10 cm square with a ten thousand-point pixel density.

For the case of a masked structure it helps to imagine the actual location of the slits with relation to the test space. So what follows here is an image of the basic masked structure setup being illuminated with a plane wave shown in FIGURE 75.

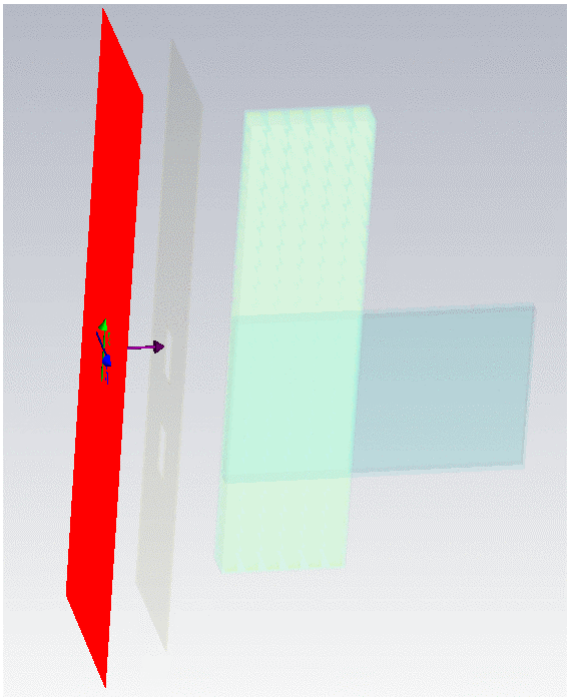

FIGURE 75: Plane wave illumination of masked model showing the test space in blue

Presented results will represent the actual measured plane wave at the prescribed frequency from the left, incident on select model, depicted by a light colored cyan. On the right side will be shown the measured response in the dark blue area. Areas on both sides of the test model will be equal. Area dimension is in square millimeters and for every case will be one hundred square millimeters. These areas are large enough to include both objects as input. Without objects the area remains the same, this is to maintain comparable consistency. Imagine the section being described on both sides of

the test structure as being the evaluation regions. These region or sections will be displayed in all cases. This description can be visualized in FIGURE 76.

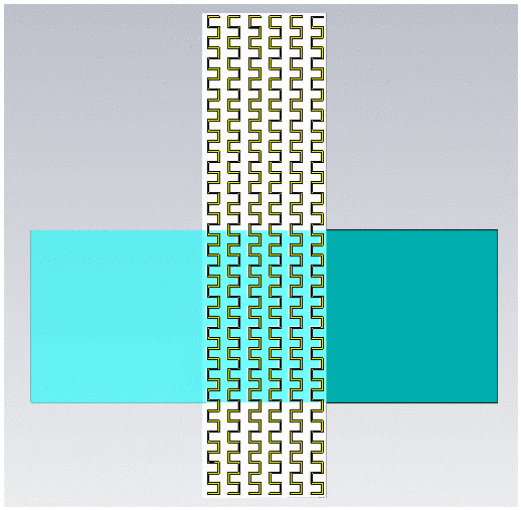

FIGURE 76: Comparison of plane wave illumination on left and test space on right

For the case with a mask involved the following depiction is presented. The same basic interpretation of signal input and output remain unchanged. This is seen in FIGURE 77.

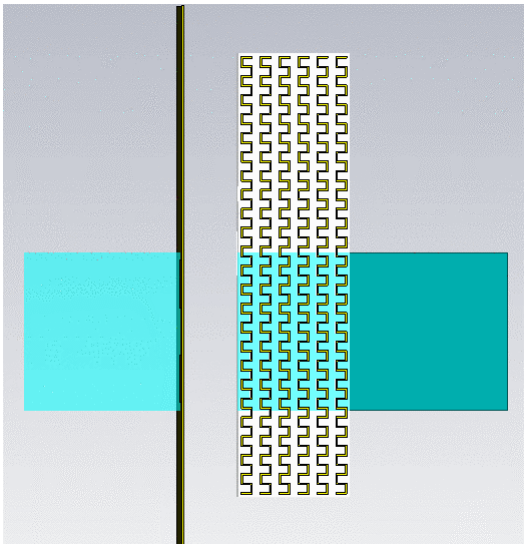

FIGURE 77: Masked model comparison of blue test areas shown on left and right

With the above-mentioned detail in mind the experiments will now be shown in a format as follows. Simulation results will appear at the top of the page, experimental results will be presented in the middle of the page as described. At the bottom of each results page will be a descriptive explanation about the graphical comparison. This discussion is intended to provide further insight of the measured test data. There will also be a qualitative comment about the helpful aspects of the experiment.

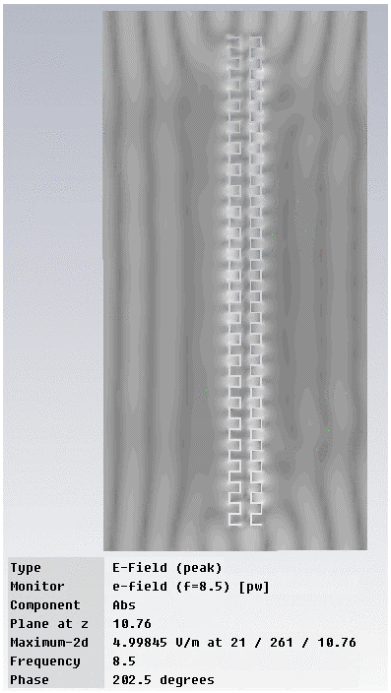

FIGURE 78: CST simulation of the 2S model at 8.5 GHz without a mask

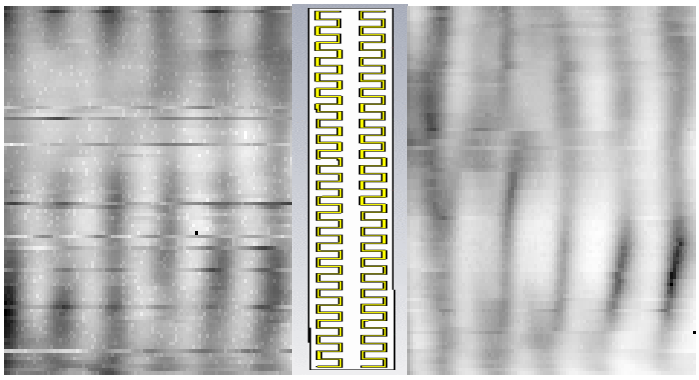

FIGURE 79: Comparative experimental tests to CST simulation seen in figure 78

The figures shown above are with reference to 8.5 GHz traveling from left to right into the 2S model.

Here the 2S model in FIGURE 79 is being evaluated with a plane wave excitation at 8.5 GHz to explore the affect on the transitioning input wave. The process of evaluation involves comparison between actual wave behaviors shown on the emerging side of the test model to the simulated response. Close examination here will reveal similar types of wave bending and minimal power differences. It appears that the experiment shows some turbulence near the exiting surface but there after resumes as an ordinary traveling wave, which is similar to the CST simulation. In summary here the experiment supports the simulation.

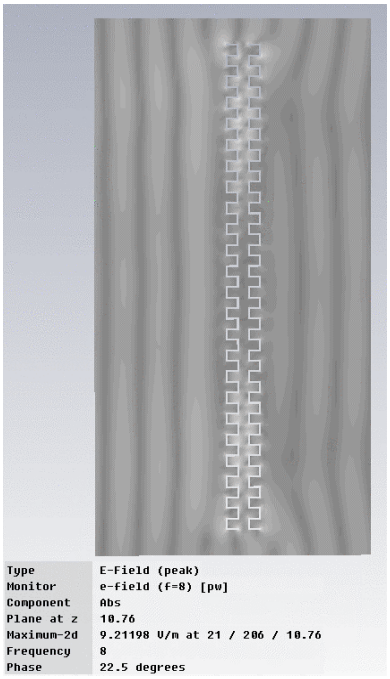

FIGURE 80: CST simulation of the 2S model at 8.0 GHz without a mask

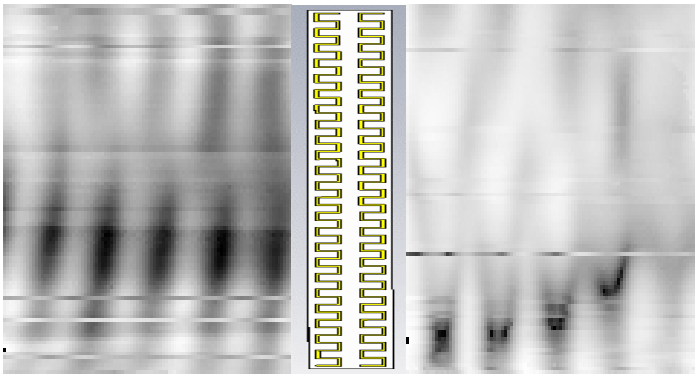

FIGURE 81: Comparative experimental tests to CST simulation seen in figure 80

The figures shown above are with reference to 8.0 GHz traveling from left to right into the 2S model.

Here the 2S model in FIGURE 81 is being evaluated with a plane wave excitation at 8.0 GHz to explore the affect on the transitioning input wave. The process of evaluation here involves a notable difference between actual wave input and output of the test 2S model. Close examination here reveals wave dampening along with an inward upward bending delineated by some absorbing regions. The degree of similarity here is comparable to the 8.5 GHz result. Wave bending and stronger power differences appear more noticeably at this frequency. It appears that this experimental result is not as easy to describe from the power point of view. The exiting wave still resembles an ordinary traveling wave, which is similar to the CST simulation. Close examination of the CST emerging wave shows that there is a smooth contour change of the wave in the immediate area to the right of the structure. As this changing contour is followed upward then there is another bending effect downward and to the right. This behavior is also seen in the experimental rest as well. Also to keep in mind here is the fact that this result is related to the lower section of the structure as was clearly depicted in the preceding discussion of

how the measurement space relates to the structure. It is further helpful to remember how CST simply shows a moderate change of the wave in the near exiting region of the structure, followed by normal plane wave resuming travel, which is comparable to the experimental display of similar behavior. In summary here the experiment moderately supports the simulation but clearly is consistent with correlation to the input incident wave.

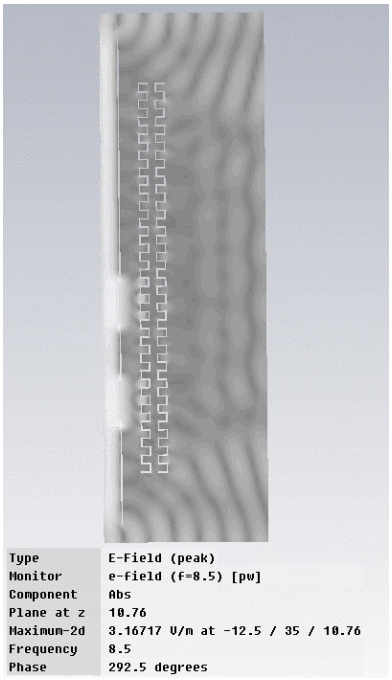

FIGURE 82: CST simulation of the 2S model at 8.5 GHz with a mask

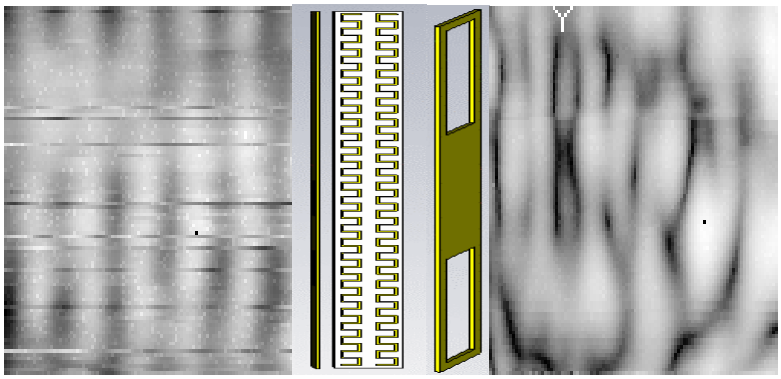

FIGURE 83: Comparative experimental tests to CST simulation seen in figure 82

Here these figures show object illumination at 8.5 GHz positioned approximately less than half of the 2S lens thickness, which is one centimeter.

Here is the first imaging case studied shown in FIGURE 83 and clearly there is a response that warrants the suggestion of possible imaging given what appears at approximately 25 mm away from the 2S model, which is coincident in this case with the imaging plane calculated to be approximately 24mm from the model face. Please recall that the 'Y' marker placed at the top of each imaging test space denotes the location of the image plane. It also appears as though the location is reasonably close to the slit locations vertically. Before continuing on it will be helpful to discuss FIGURE 82 and any possible association with an image formation. In most all cases simulations are intended for support and comparison without any suggestion as to being the final decision. FIGURE 82 displays in the lower half section two object inputs within a wavelength of the 2S model input surface. Now given that this real 2S model is estimated to have a negative index close to –0.8 then only a limited range of k vector angles will enter the metastructure. Theoretically when the medium exhibits a –1.0 then and only then will all the k vectors up to 90 degrees be collected into the metamaterial. CST will follow this theoretical basis as prescribed by Veselago [6]. Therefore one can expect a possible partial simulated image formation and in this case it will be plus or minus 40 degrees about the central normal line. Given that the two objects represent two half spheres then only approximately forty five percent can be expected to contribute to the possible image formation. With this theoretical basis in mind it will be further instructive to examine the physical limitations as well. There is a loss factor that is inherent to the metal that forms the S pattern and this loss as described in section 5.1

translates into minimum image spot size. So for an estimate at 8.5 GHz using copper as the conductivity parameter with a thickness less than 50 mm then the image size would be close to 6 mm. This size or larger is thought to be resolvable. Taking all these aspects into account suggests that the possible image formation for the thinnest lens (2S model) is still possible given the slit dimensions of 30 mm long and 14 mm wide. If the theoretical basis is believed then there will be a cone of angles passing into the metamaterial or another way to view this is by sector length, which is the product of the angle and radius from center distribution of the object slit, roughly this approximates to 7 mm. CST will follow the math precisely as it simulates or numerically evaluates the structure. Being on the border of these mentioned parameters make it difficult to easily observe simulated images, but there is a small but noticeable output cluster section located close to half way between the two slits on the output side which corresponds to the observed region of the experimental results.

Though it is worth noting, there is strong association to the simulation regarding the localized formation immediately in front of the test structure as well. Given the actual values of permittivity $\varepsilon = -0.99 - i0.36$ and permeability $\mu = -0.99 - i0.36$ taken from the ideal model parameters it's likely to make the image-bearing wave very hard to see. We know from simulations that if the loss could be reduced from –0.36 to approximately -0.03, a factor of 12 in this case, then definitely an mage can be seen. There was always the hope that since the effective medium is only just satisfied that there might have been some scattered component we could detect against the scattered straight through wave. These realized limitations help in understanding that unless loss is reduced there will be

essentially no penetration of the field into the structure thus explaining why the image is so difficult to see.

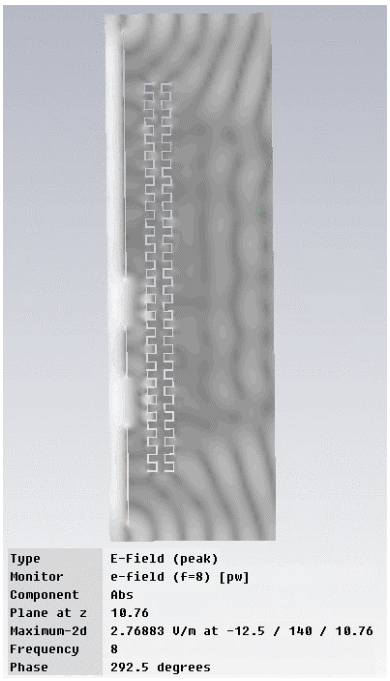

FIGURE 84: CST simulation of the 2S model at 8.0 GHz with a mask

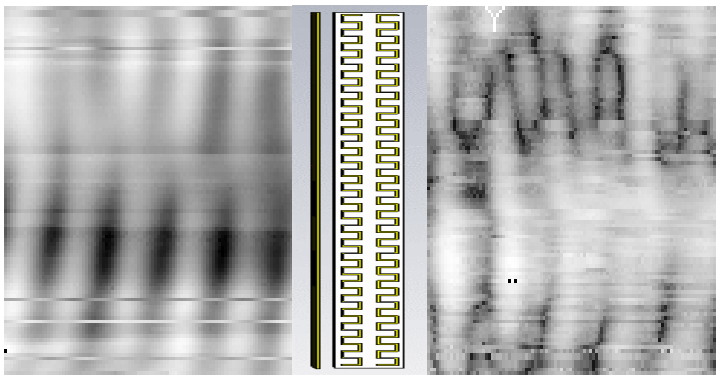

FIGURE 85: Comparative experimental tests to CST simulation seen in figure 84

Here these figures 84 and 85 show object illumination at 8.0 GHz positioned approximately less than half of the 2S lens thickness, which is one centimeter.

The results for 8.0 GHz is without question significantly different than at 8.5Ghz. What appears is still some imaging possibility but not closely aligned with the CST

simulation. There are some defining lines and localized regions but not clearly associated to the objects. Plane wave absorption is also noticed here. Opinion here is that the imaging evidence is minimal at best.

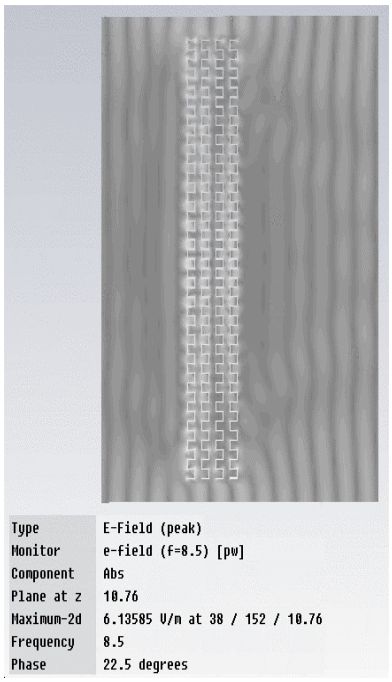

FIGURE 86: CST simulation of the 4S model at 8.5 GHz without a mask

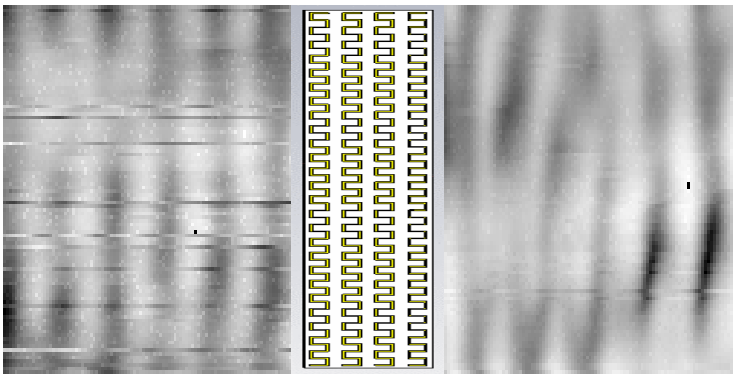

FIGURE 87: Comparative experimental tests to CST simulation seen in figure 86

The above 4S model seen in FIGURE 87 is being evaluated shows agreement between simulation and experiment at 8.5 GHz in terms of shallow plane wave emergence bending toward the center. Minimal absorption is similar to CST. This experiment is in fairly good agreement to the simulation.

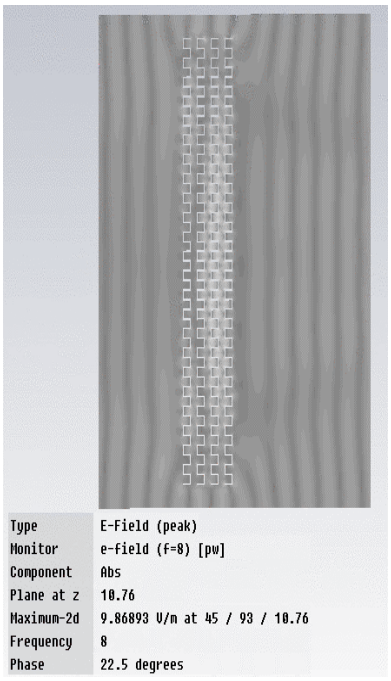

FIGURE 88: CST simulation of the 4S model at 8.0 GHz without a mask

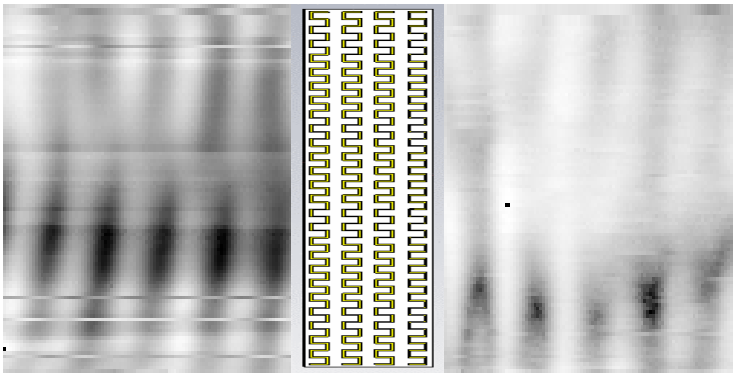

FIGURE 89: Comparative experimental tests to CST simulation seen in figure 88

FIGURE 89 shows at 8.0 GHz there appears to be minimal attenuation and ordinary wave emergence traveling to the right. Not much more to say here, other than this is in partial agreement with the simulation.

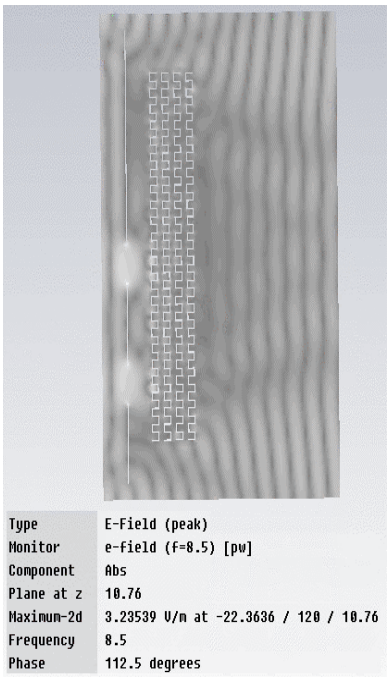

FIGURE 90: CST simulation of the 4S model at 8.5 GHz with a mask

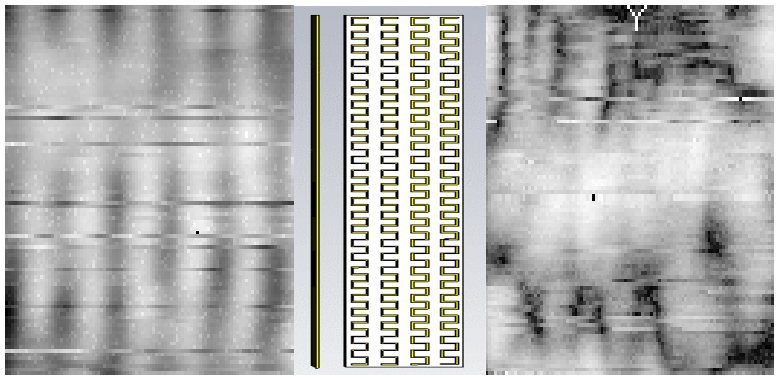

FIGURE 91: Comparative experimental tests to CST simulation seen in figure 90

Figures 90 and 91 show object illumination at 8.5 GHz positioned approximately less than half of the 4S lens thickness, which is approximately two centimeters.

This is the first imaging evaluation for the 4S model and it appear obvious that the agreement between simulation and experiment has broken down. It's not clear as to why the disagreement, but there may be some additional noise in these results given the analyzer unexpected updates of the memory registers as well as the possibility of more

frequent alignment of the internal power heads. These results will be taken to be weakly at best following the simulation and therefore is undecided as to contribution.

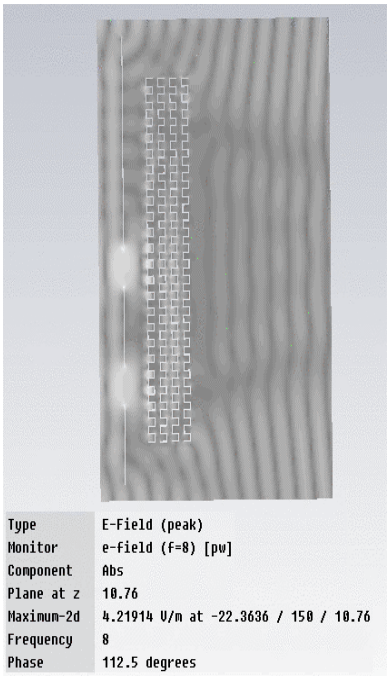

FIGURE 92: CST simulation of the 4S model at 8.0 GHz with a mask

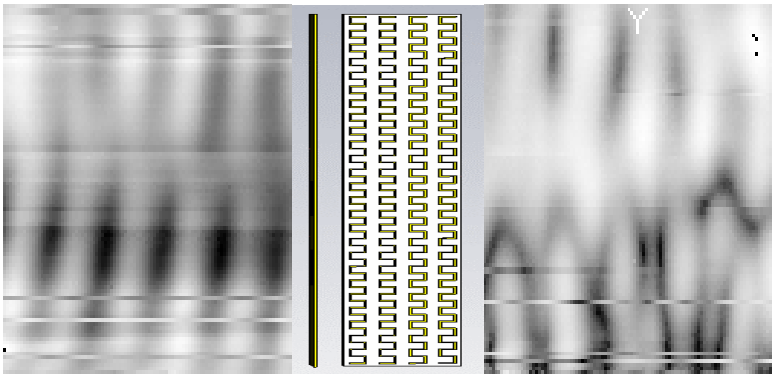

FIGURE 93: Comparative experimental tests to CST simulation seen in figure 92

Figures 92 and 93 show object illumination at 8.0 GHz positioned approximately less than half of the 4S lens thickness, which is approximately two centimeters.

Now come some interesting observations. Notice in the emerging area there is somewhat bending from the top and bottom along with noticeable attenuation. There is

not any clear imaging evidence from the depiction but there is moderate agreement between the lower defining region and the simulation. The lower tracks with interrupted power along with the upward bending are similar. In brief, not any imaging evidence, though there is moderate agreement with CST.

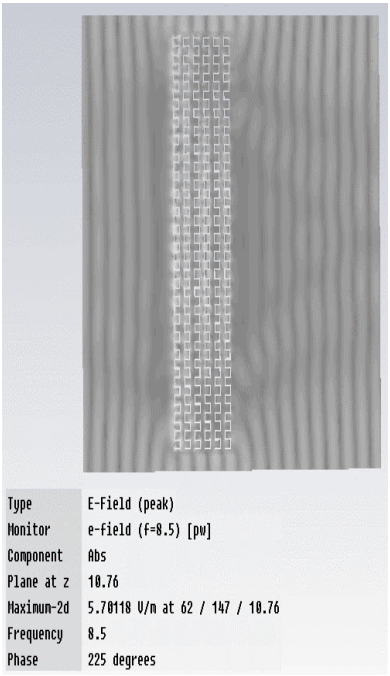

FIGURE 94: CST simulation of the 6S model at 8.5 GHz without a mask

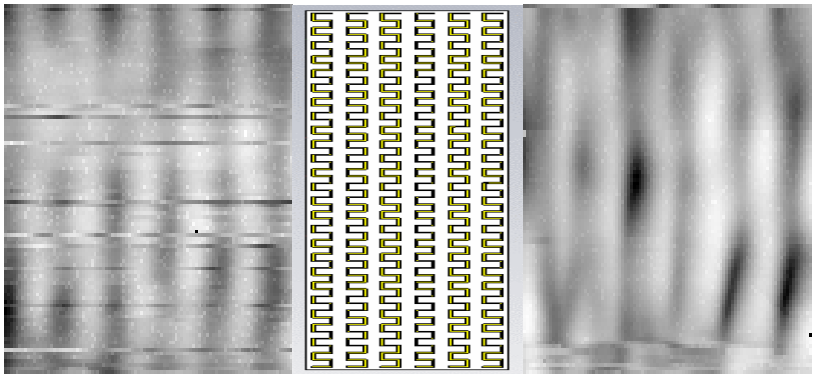

FIGURE 95: Comparative experimental tests to CST simulation seen in figure 94

Figures 94 and 95 shown above are with reference to 8.5 GHz traveling from left to right into the 6S model.

For the case of 6S model shown here excited at 8.5 GHz, it simply appears as a plane wave input and a plane wave output. Yes there is some agreement with the simulated response and not anything further to be discussed. The experiment follows the simulation.

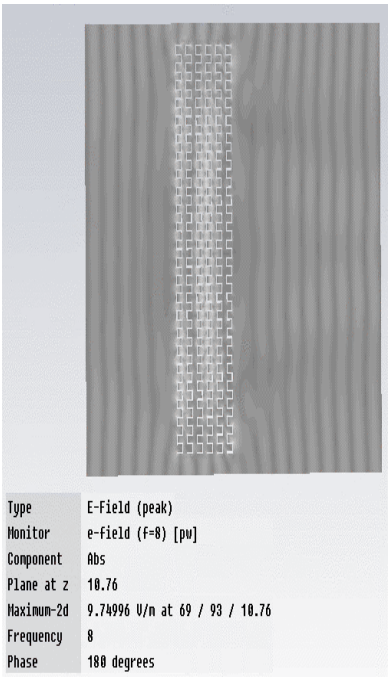

FIGURE 96: CST simulation of the 6S model at 8.0 GHz without a mask

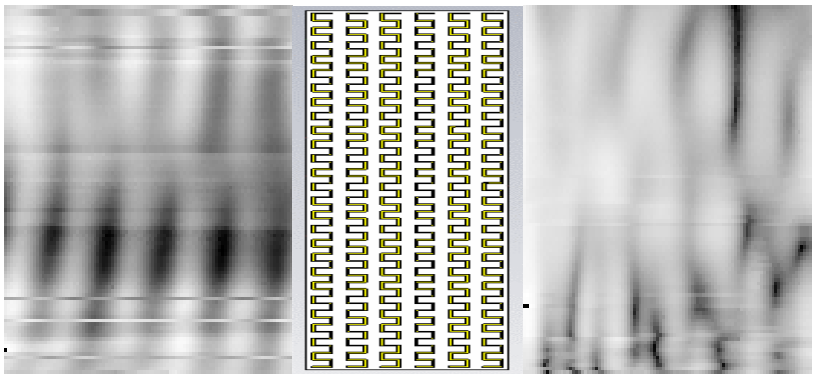

FIGURE 97: Comparative experimental tests to CST simulation seen in figure 96

Figures 96 and 97 shown above are with reference to 8.0 GHz traveling from left to right into the 6S model.

At 8.0 GHz there is without doubt strong difference when compared to the 8.5 GHz, such as the energy bunching effect immediately in front of the exiting face. The plane wave appears to bend in an unusual display near the lower region. There is agreement between this and the strange bending effects observed in the simulated results as well. There is not any defining statement here other than it is not as closely in agreement as is the 8.5 GHz case. In summary this is undecided.

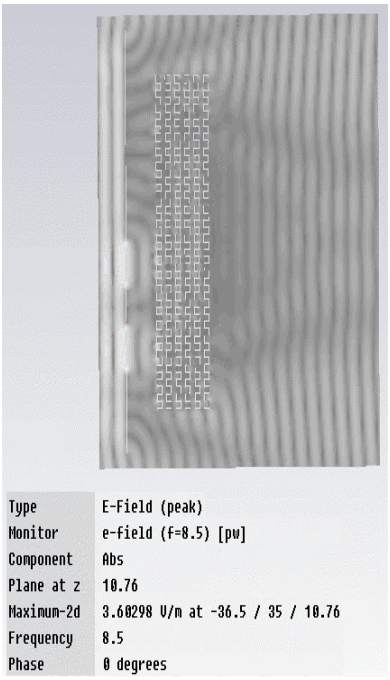

FIGURE 98: CST simulation of the 6S model at 8.5 GHz with a mask

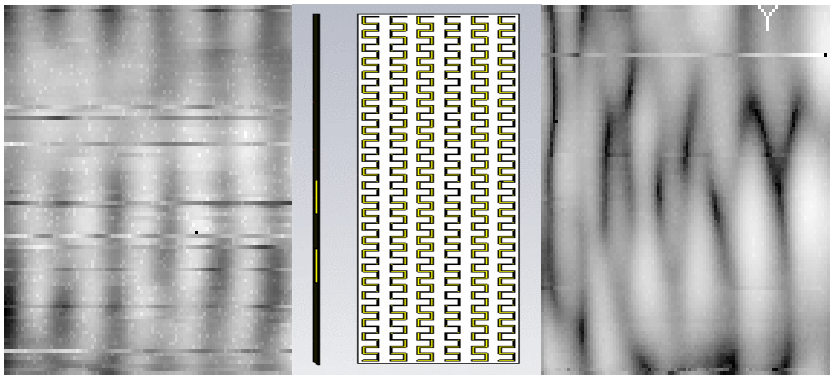

FIGURE 99: Comparative experimental tests to CST simulation seen in figure 98

Figures 98 and 99 show object GHz illumination at 8.5 positioned approximately less than half of the 6S lens thickness, which is approximately three centimeters.

Again this imaging experiment at 8.5 GHz is showing interesting association to the objects in terms of horizontal position and vertical location. If attention is given to the location estimated to be approximately two to three centimeters away, it almost appears as the central portion of the metal spacing between the slits given the darkened line. There is also gradual bending from the lower section upward to the center and there also appears to be attenuation more so in the upper section. In conclusion, there is agreement with the simulation as mentioned.

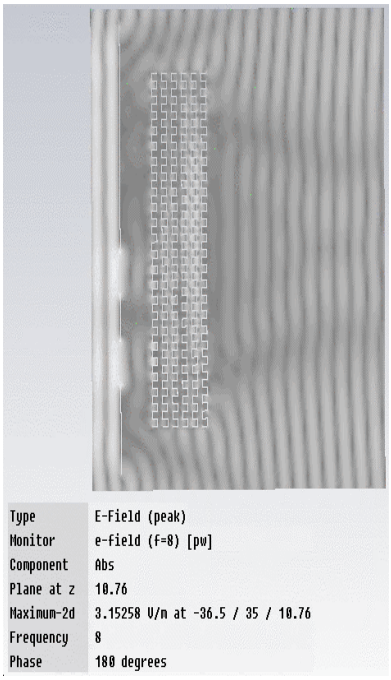

FIGURE 100: CST simulation of the 6S model at 8.0 GHz with a mask

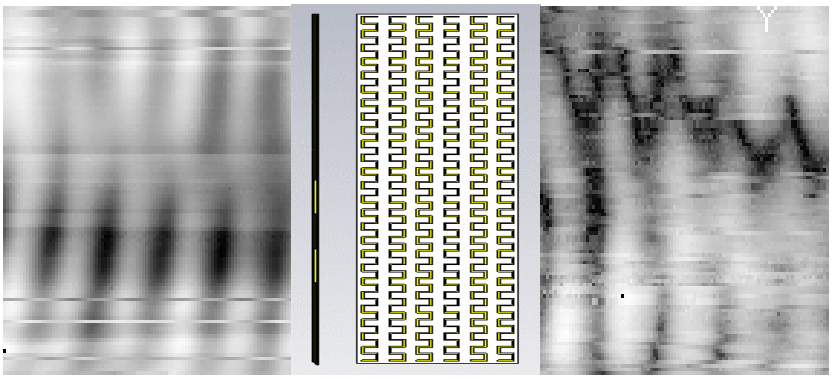

FIGURE 101: Comparative experimental tests to CST simulation seen in figure 100

Figures 100 and 101 show object illumination at 8.0 GHz positioned approximately less than half of the 6S lens thickness, which is approximately three centimeters.

This experiment is almost the reverse of the 6S results shown at 8.5 GHz. There is a clear projection from the upper region toward the central section, bending down. There is one section in the upper half near the estimated two-centimeter location away fro the exiting face that displays what might be described as a small window opening. This opening may be imaging evidence, notice the shade of this apparent window is in between bright and dark. This result has both agreement with the simulation and the possibility of imaging. In summary, there is agreement some notable aspects of imaging.

7.6 Conclusion of final experiments

In summary these physical experiments agree with the CST simulated results showing that imaging is not observable when the index is far enough away from –1. These experimental results strongly support the CST simulations in various ways leading to the understanding that CST is capable of continued guidance toward obtaining a working model that exhibits a –1 index. In the future CST and the experiment can become linked in real time to effect closer cause and effect relationships. Also the experimental test

equipment will need upgrading to accommodate the memory demand required of high-resolution imaging. This equipment would need to be modified for lock step synchronization, which disallows one system from affecting another due to inherent slower performance and memory restrictions. Computer control will incorporate a movable test platform that will ensure fractional millimeter placement of the model under test. Given these experimental results it would make sense to continue further research into this negative one index pursuit. Also the equipment change would allow much higher variability along with continuous twenty-four hour real time measurements. In closing actual photos of the equipment and setup are included in the appendix.

CHAPTER 8: CONCLUSIONS AND FUTURE RESEARCH

In this dissertation, research conducted on studies of the electromagnetic properties of various metamaterials has been presented. Early research on the use of form-birefringent metamaterials for field enhancement and reduced group velocities was supplanted by an in depth study of negative index metamaterials. This was driven by the promise such materials have for achieving, in principle, "perfect" or arbitrarily high resolution images for any given wavelength. Investigating the designs and methods to make an artificial material exhibiting an index less than one with the final goal being an index equal to –1 thus became the dominant objective of this research.

Globally, there is continued ongoing effort to design and build metamaterials exhibiting a negative index over some useful band of electromagnetic frequencies. Metamaterial models typically follow examples introduced by Sir John Pendry's thin wire structure and split ring resonator. Though these models successfully predict negative indices, few as of yet have provided bulk materials for practical applications. Researchers including Kong have refined these initial examples through mathematical and experimental analysis, leading to a modified version of a split ring resonator, which we refer to as the "S model." Some experimental results based on this model were published and claim to demonstrate experimentally a negative index. This dissertation has argued that the S structure is attractive as a starting point given the existence of a

closed form mathematical model for it, which was derived as part of this dissertation work.

After the review of Kong's S model, through the newly derived mathematical model it became obvious how to further refine Kong's S model to more readily lead to the negative index property required at microwave frequencies. The use of microwave circuit theory along with thorough CST simulations helped with this analysis. Specifically, the backside mirrored metal pattern was removed leaving just the patterned S topside metal trace on a substrate. Placing this single patterned circuit board on top of another resulted in an improved working unit model that clearly demonstrated a smooth continuous backward wave, indicative of a negative index. This structure exhibits an index closer to –1 as compared to the original model that did not. The original work by Kong's group had three limitations: (1) material alignment with respect to polarization and propagation direction were not clearly specified; (2) initial inductance calculations were dimensionally incorrect and (3), while the mirrored pattern reduced the permeability as proposed, it adversely limited the permittivity. After these issues were addressed, a new model was designed and analyzed using CST. Following this, an actual structure was built and experimentally tested using computer controlled microwave test equipment. Experimental and numerical results were consistent to the degree expected but unfortunately, the design did not lead to an index that was close enough to –1. Nevertheless, CST predicted responses that were consistent with the observable results when compared side by side, giving confidence in the new model and its potential to be further modified to more closely approach -1. As was known from the literature,

significant deviation from an index of -1 combined with material losses can reduce the image resolution.

With respect to the simulated and experimental results supporting the conclusion that an index of –1 is required to realize very high resolution imaging, it makes sense to consider the following observations gleaned from this research. One of the most significant facts realized during the early stages of this research was that making conductivity a variable is central toward achieving an index less than one. This appreciation provided a strong basis upon, which to adopt a conductivity model that could be varied in such a way as to tune the observable negative index. The Drude conductivity model also provided the initial evidence to support the hypothesis that an index of n = –1 would allow high resolution imaging as demonstrated in chapter 5. Following this realization was the fact that liquids could provide a physical means through which to introduce a variable conductivity in practice. This taken in conjunction with the fact that the S-shaped resonator also exhibits an electrical plasma behavior, made it clear that this particular modified S-split ring resonator demonstrates a plasma behavior for both magnetic and electric fields and lends itself to a microfluidic channel for conducting liquids to be incorporated. The final salient point to mention is that loss mechanisms are associated with the imaginary part of the permittivity and which is a function of conductivity. Consequently, varying conductivity also directly impacts the image resolution obtained. Based on these observations, we suggest the next step toward the pursuit of the ideal low loss index close to –1 be the following suggestion. An S or helix like structure of conductive liquid within an ionizable gas forming the bulk negative index metastructure. This structure of conductive liquid surrounded by an ionized gas

results in a plasma-based permittivity that closely associates with the ideal model evaluated in this dissertation. The converse of a structure of ionized gas immersed in conducting liquid, behaving as a quasi-permittivity plasma surrounded by a variable permeability would also work. Reducing losses while not losing the resonance-driven negative index over the bandwidth we require or making the effective medium approximation less valid needs to be emphasized in future work to aid in observing possible image formation. These suggestions for future work need to be modeled and experimentally tested and could provide the path forward to greatly improved image resolution and to some degree, subwavelength resolution not currently possible using traditional materials for lenses.

REFERENCES

[1] Alex Figotin and Ilya Vitebskiy,"Gigantic transmission band-edge resonance in periodic stacks of anisotropic layers" Physical Review E 72,036619, (2005).

[2] K. Y. Jung and F. L. Teixeira,"Photonic crystals with a degenerate band edge: Field enhancement effects and sensitivity analysis " Physical Review B 77,125108, (2008).

[3] AA Chibanov,"Strongly resonant transmission of electromagnetic radiation in periodic anisotropic layered media" Physical Review A 77,033822, (2008).

[4] J. B. Pendry, "Negative Refraction Makes a Perfect Lens" Physical Review Letters Volume 85, Number 18, pages 3966 – 3969, (2000).

[5] V. E. Pafomov, “Transition radiation and Cerenkov radiation”, Soviet Physics JETP, Volume 36 (9), Number 6, pages 1321 – 1324, (December 1959).

[6] V. G. Veselago “The Electrodynamics of Substances with simultaneously negative values of permittivity and permeability" Usp. Fiz Nauk 92, 517-526, (1968).

[7] Norris, A. N., Sheng. P. and Callegari. A. J. “Effective medium theories for two-phase dielectric media”, Appl. Phys.Lett. 57, pages 1990-1996, (March 1985)

[8] B. A. Munk, “Metamaterials Critique and Alternatives” Wiley, 2009

[9] Alex Figotin and Ilya Vitebskiy, "Slow-wave resonance in periodic stacks of anisotropic layers”, Physical Review A 76, 053839, (2007).

[10] Hongsheng Chen, Lixin Ran, Jiangtao Huangfu, Xianmin Zhang, and Kangsheng Chen, Tomasz M. Grzegorczyk and Jin Au Kong "Left-handed materials composed of only S-shaped resonators" Physical Review E 70, 057605, (2004).

[11] D. A. G. Bruggeman, "Berechnung verschiedener ohysikalischer Konstanten von heterogenen Substanzen. I. Dielectrizitatkonstanten und Leitfahigkeiten der Mischkorper aus isotropen Substanzen", Ann. Physik (Leipzig) 24, 636-679 (1935).

[12] R. Landauer, "The electrical resistance of binary metallic mixtures", J. Appl. Phys. 23, 779-784 (1952).

[13] D. R. Smith, Willie J. Padilla, D. C. Vier, S. C. Nemat-Nasser, and S. Schultz "Composite Medium with Simultaneously Negative Permeability and Permittivity" Physical Review Letters, Volume 84, Number 18 pages 4184 - 4187 (2000)

[14] Xiangxiang Cheng, Hongsheng Chen, Lixin Ran, Bae-Ian Wu, Tomasz M. Grzegorczyk, and Jin Au Kong "Negative refraction and cross polarization effects in metamaterial realized with bianisotropic S-ring resonator", Physical Review B 76, 024402, (2007).

[15] Xudong Chen, Tomasz M. Grzegorczyk, Bae-Ian Wu, Joe Pacheco, Jr., and Jin Au Kong "Robust method to retrieve the constitutive effective parameters of metamaterials" Physical Review E 70, 016608,(2004)

[16] H. S. Chen, L. X. Ran, J. T. Huangfu, X. M. Zhang, and K. S. Chen "Magnetic properties of s shaped split ring resonators" Progress In Electromagnetics Research, PIER 51, 231-247, (2005)

[17] Ruopeng Liu, Tie Jun Cui, Da Huang, Bo Zhao, and David R. Smith "Description and explanation of electromagnetic behaviors in artificial metamaterials based on effective medium theory" Physical Review E 76, 026606, (2007)

[18] J. B. Pendry, "Refining the perfect lens" Physica B, Number 338, pages 329–332 (2003).

APPENDIX A: APPROACHING -1 INDEX MAKES PERFECT IMAGE

CST simulations showing how image formation approaches equal correspondence to the object as the negative index approaches –1 from either direction between (-.5 to –1.5). It will be helpful to have these images included here to clearly show how the image formation behaves given an index outside of the prescribed goal of –1. These images can be used to gauge how extreme the resulting image association can be when the design specifications move away from the targeted numbers. These images are also helpful to study the possibility of image formation occurring at locations other than expected. Also they are exceptional details that might in the future help understand evanescence at the boundaries. These images are also a quick comparison for estimations of object placement and image formation.

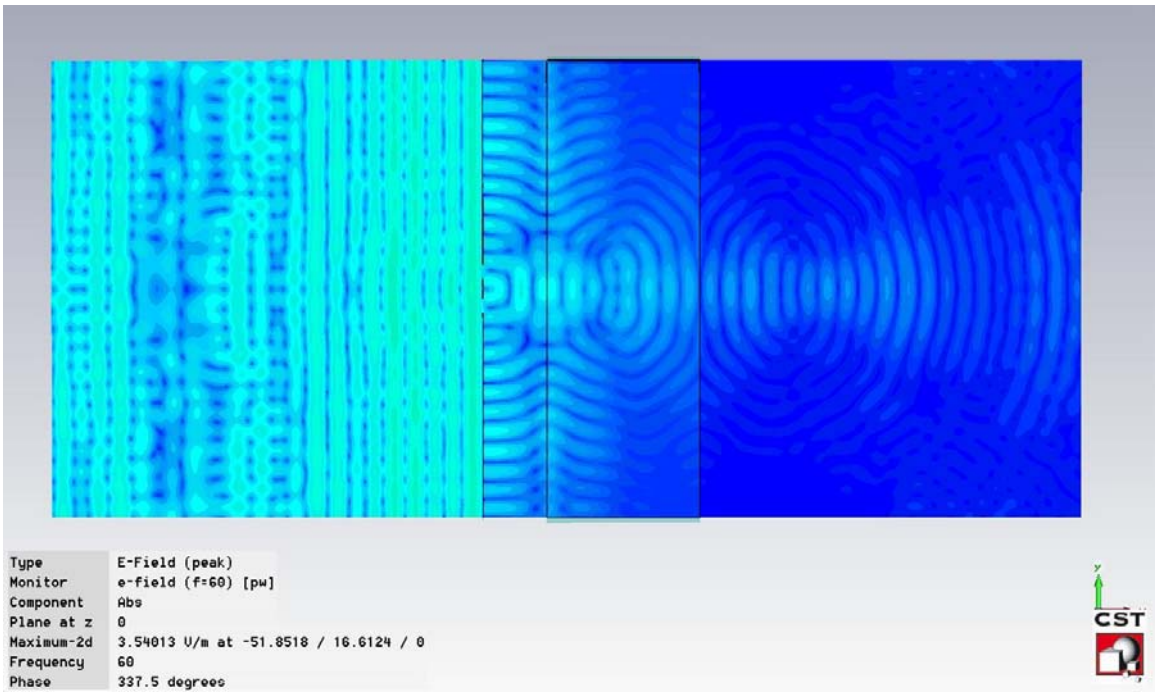

FIGURE 102: Double slit illuminations into –1 index region, two images seen

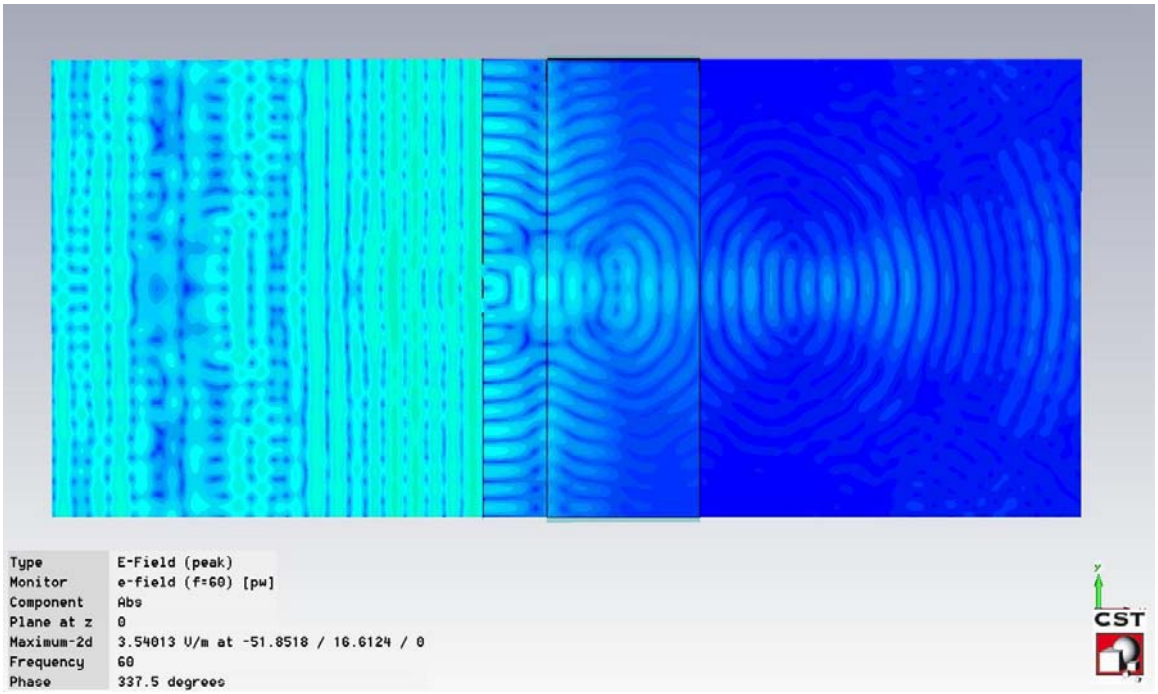

FIGURE 103: Double slit illuminations into –1 index region, two perfect images

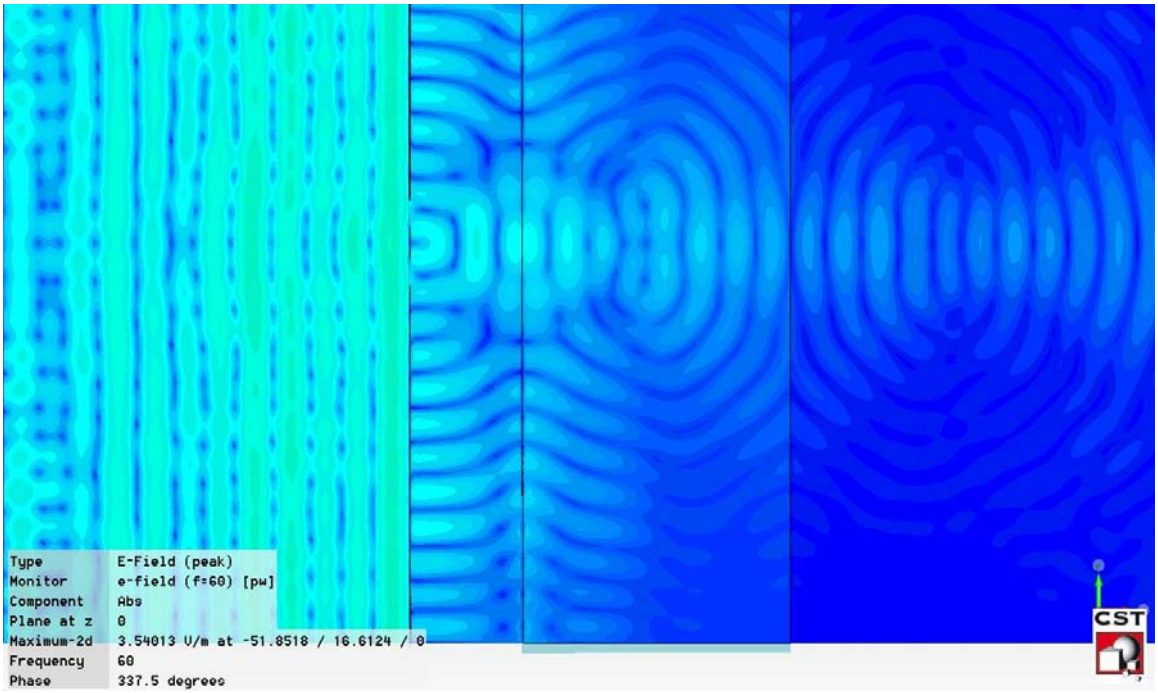

FIGURE 104: Double slit illuminations into –1 index region, two perfect images

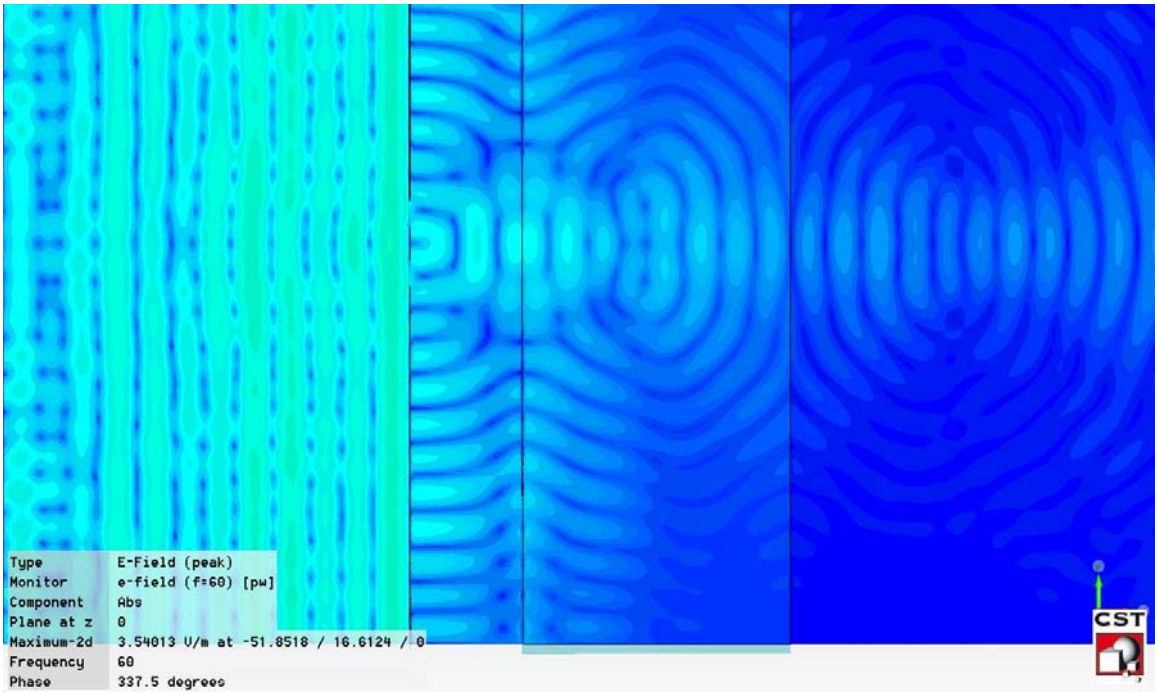

FIGURE 105: Double slit illuminations into –1 index region, two images seen

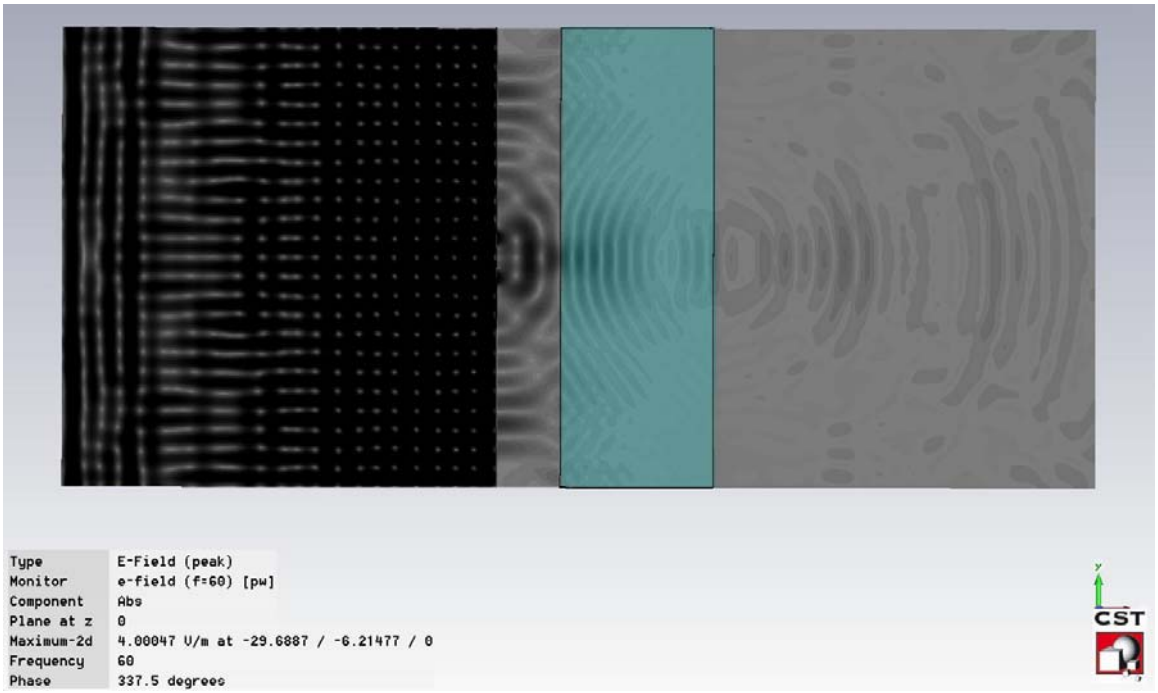

FIGURE 106: Double slit illuminations into –1.4 index region, two perfect images

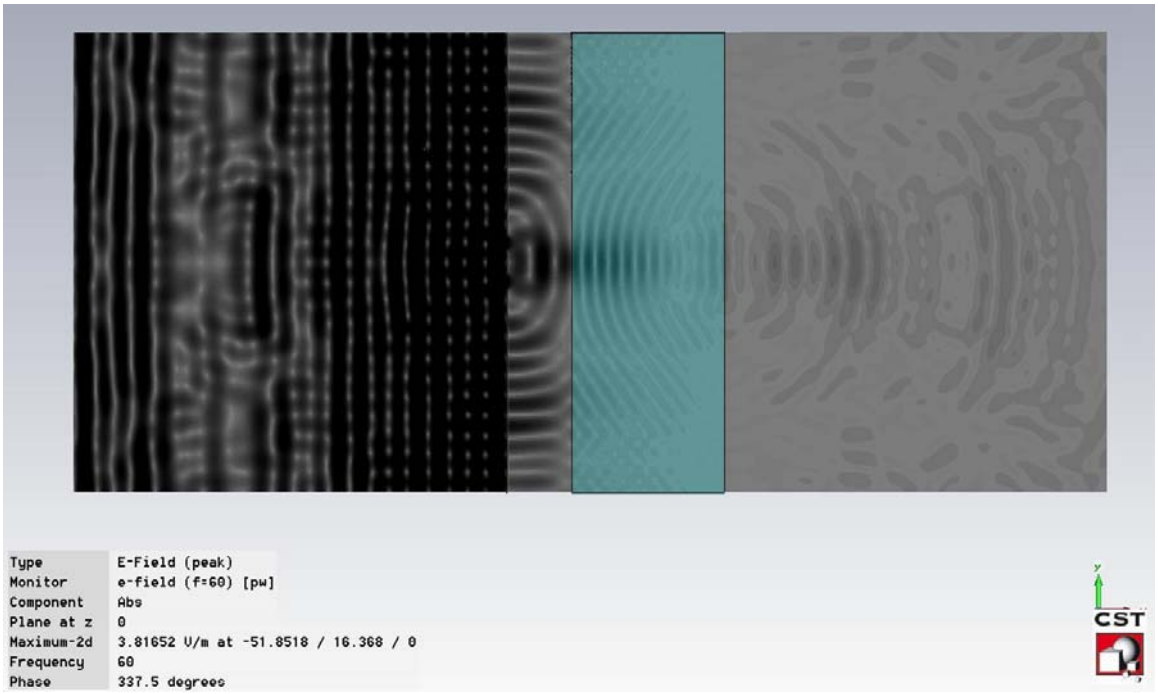

FIGURE 107: Double slit illuminations into –1.5 index region, two perfect images

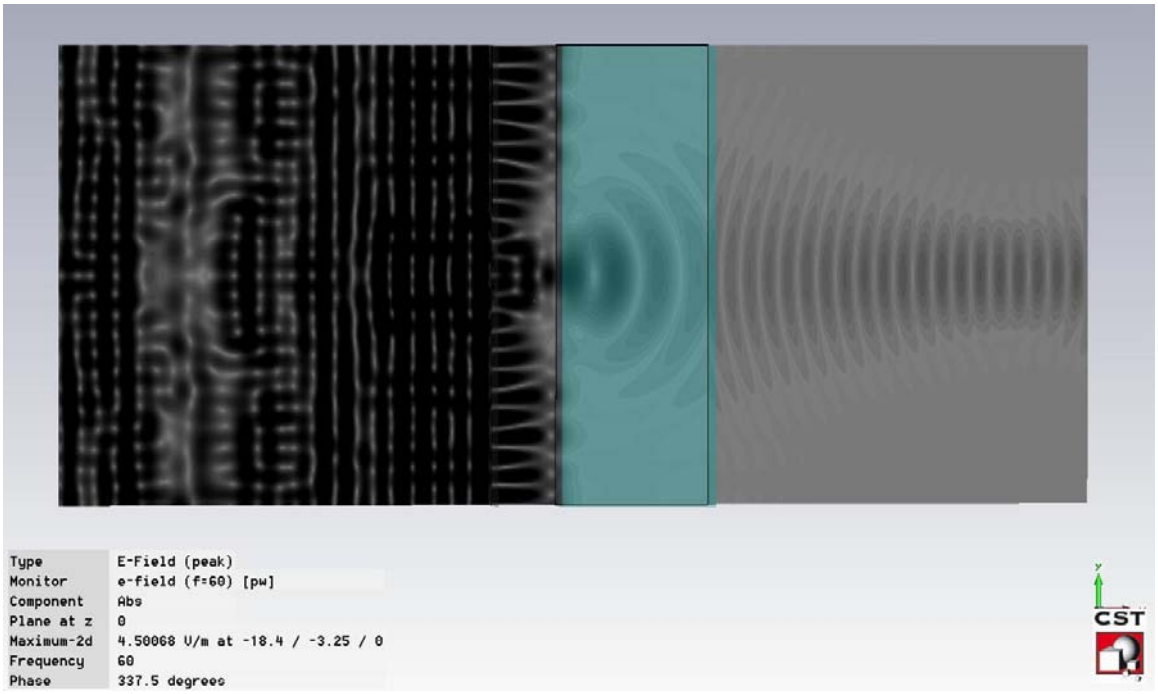

FIGURE 108: Double slit illuminations into –0.5 index region, two perfect images

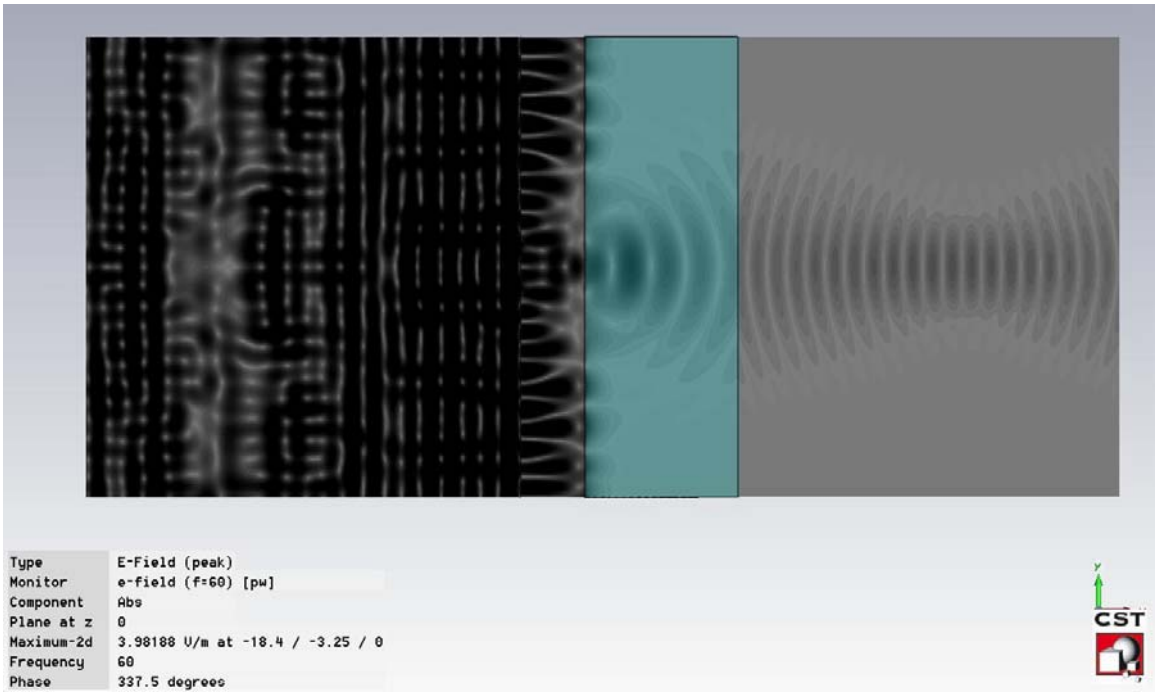

FIGURE 109: Double slit illuminations into –0.6 index region, two perfect images

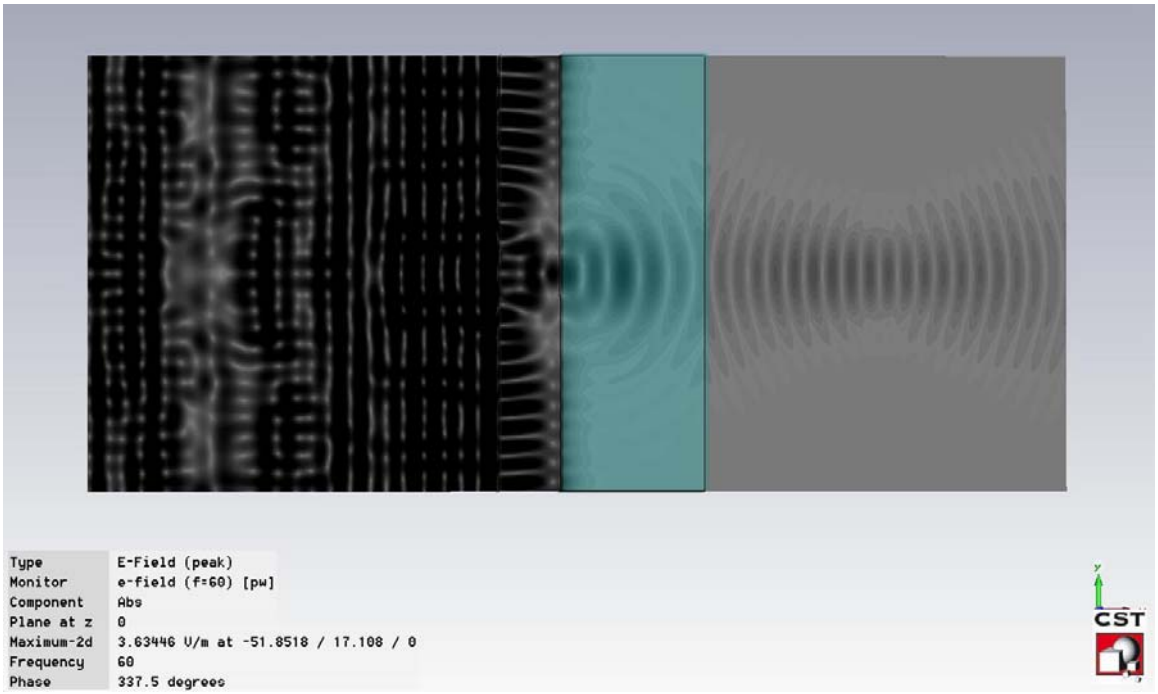

FIGURE 110: Double slit illuminations into –0.7 index region, two perfect images

APPENDIX B: THEORETICAL DESIGN AND APPLICATION OF DBE

Anisotropic Periodic Structure Exhibiting Gigantic Field Enhancements

J. O. Schenk, R. P. Ingel, Y. Cao and M. A. Fiddy,
Center for Optoelectronics and Optical Communications,
University of North Carolina at Charlotte, Charlotte, NC, 28223
mafiddy@email.uncc.edu; phone 704-687-8594; fax 704-687-8241

Abstract

A strongly anisotropic photonic crystal structure was designed using form birefringence. It has a low group velocity close to a split band edge (SBE) and large field enhancements proportional to the fourth power of the number of periods are predicted. Numerical results are presented illustrating the bandgap behavior as a function of anisotropy and an effective negative index property is discussed.

Keywords: Anisotropic photonic crystal, resonant effect, degenerate band edge, group velocity

INTRODUCTION

We have been investigating a 1D strongly anisotropic photonic crystal structure which was designed to have large resonant effects in transmission and reflection and a very low group velocity close to a degenerate band edge (DBE). Form birefringence is employed to realize the high degree of anisotropy required for a DBE as suggested by the theoretical work of Figotin and Vitebsky [1,2]. Anisotropies greater than 10% are needed and this is very hard to achieve with naturally occurring materials at optical frequencies. In addition, each period of the structure requires two anisotropic and one isotropic layer and the degree of anisotropy and layer thicknesses allow one to tune the resonance conditions. In principle, at a transmission resonance in the vicinity of a DBE, the resonant field intensity increases as N^4 within the structure where N is the total number of periods. In the case of a regular band edge, the field intensity is only proportional to N^2. Numerical results are presented illustrating the bandgap behavior as a function of anisotropy and both microwave and optical structures have been made. The optical structure is a challenge because of the form birefringent feature sizes that have to be fabricated. The microwave structure has exhibited the level of field enhancements predicted (~ X80 for the material properties we used) and unexpected field enhancements at specific frequencies and locations outside the structure were also observed. A closer look at these resonance effects have shown a strong correlation between the frequency at which the internal field enhancement occurs and a distinct and highly reproducible positive slope in the transmission phase spectrum. An interpretation of this is a change in sign of the group delay or effective negative refractive index.

band edge behaviors

1D anisotropic photonic crystal structures have attracted more attention in recent years due to their unusual and still somewhat surprising optical properties. Compared with 1D isotropic photonic crystal structures, the theoretical analysis, fabrication and characterization of 1D anisotropic photonic structures are less straightforward. Possible applications include slow-light devices and sensing [3-5]. Using band-edge resonances to slow down light in isotropic one-dimensional photonic crystal structure has been investigated by Scalora *et al*. [6]. It is well known that the maximum group delay and the associated field intensity enhancement occur at the transmission peak closest to the band-edge of the forbidden gap. Band edge resonant effects for anisotropic one-dimensional photonic crystal structures have been investigated by Mandatori *et al* [7] who specifically considered birefringence in 1D periodic band gap structures and Figotin and Vitebskiy [1,2]. The latter proposed that in the case of a transmission resonance in the vicinity of the degenerate band edge (DBE), which has degeneracy of the order 4, the resonant field intensity

enhancement is proportional to N^4, where N is the total number of periods rather than regular band edge (RBE) whose field intensity enhancement is proportional to N^2.

We consider a multiple layer structure including anisotropic media, which is nonmagnetic and not optically active and the Cartesian coordinate system is chosen such that the x axis is normal to the interface. From Snell's law, when a single plane wave propagates through the multiple layer structure, the tangential components of the wave vectors remain the same throughout the layered medium, and all the wave vectors lie in the same plane (the incident plane). Without loss of generality, the light propagation can be assumed to be in the *x*-*y* plane, as a consequence, the z-component of the wave vector is zero, the electric field has an $\exp i(k_0\alpha x + k_0\beta y - \omega t)$ dependence in each layer, where, $k_0 = 2\pi/\lambda = \omega/c$, $\alpha = n\cos\theta$ and $\beta = n\sin\theta$. A plane wave propagating in the *x*-*y* plane and incident on a single parallel-sided layer of biaxial material, as illustrated in Fig.1 will initiate four plane waves in the biaxial layer, two forward-traveling waves and two backward-traveling waves in the same *x*-*y* plane. The four waves are linearly polarized, and share the same value of the Snell's law quantity β with the incident wave. Representing the electromagnetic field in the form of the plane harmonic waves $\vec{E} = \vec{E}_0 e^{i(\vec{k}\vec{r}-\omega t)}$ and $\vec{H} = \vec{H}_0 e^{i(\vec{k}\vec{r}-\omega t)}$, one can obtain Maxwell's equations in the matrix form [1]

$$n\hat{s}\vec{E} = z_0\vec{H}$$
$$n\hat{s}\vec{H} = -\frac{1}{z_0}\hat{\varepsilon}\vec{E} \tag{1}$$

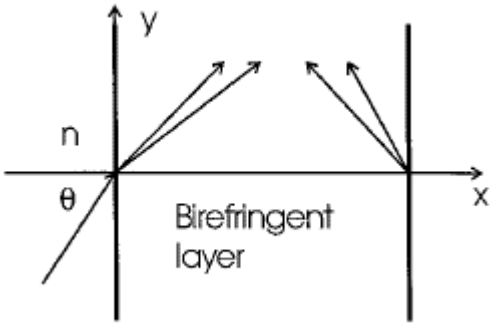

Figure. 1: An incident pane wave establishes four traveling waves in a biaxial layer.

where matrix $n\hat{s}$ implements the $(\vec{k}/k_0)\times$ operation, which can be represented by equation (2)

$$n\hat{s} = \begin{bmatrix} 0 & 0 & \beta \\ 0 & 0 & -\alpha \\ -\beta & \alpha & 0 \end{bmatrix} \tag{2}$$

Here $\hat{\varepsilon}$ is the permittivity tensor, and $z_0 \equiv (\mu_0/\varepsilon_0)^{1/2}$.

The four traveling wave fields in a biaxial layer change phase linearly with displacement in the *x*-direction, but at different rates. Along the same path, which is assumed to be always in the same layer, the absolute values of the field coefficient a's remain constant but the phase changes. The phase matrix,

$$\hat{A}_d = \begin{bmatrix} \exp(-i\phi_1^+) & 0 & 0 & 0 \\ 0 & \exp(-i\phi_1^-) & 0 & 0 \\ 0 & 0 & \exp(-i\phi_2^+) & 0 \\ 0 & 0 & 0 & \exp(-i\phi_2^-) \end{bmatrix}$$

(3)

where $\phi_{1,2}^{\pm} = k_0 \alpha_{1,2}^{\pm} d$ transforms the traveling wave field coefficient from one point (at $x = x_0$, say) to the traveling wave field coefficients at another point (at $x = x_0 - d$). The transformation property of $\hat{A}_d$ can be written as $\vec{a}_{x_0-d} = \hat{A}_d \vec{a}_{x_0}$, and thus this the phase matrix transforms the field coefficients between two points in the same layer.

The propagation of the plane wave in a periodic medium obeys the Floquet theorem [1,2] by which we can get an equation for a unit cell

$$\hat{M}_L \vec{E}_K(x) = \exp(-iKL)\vec{E}_K(x)$$

(4)

The subscript K indicates that the function $\vec{E}_K(x)$ depends on K which is known as the Bloch wave number. *L* denotes a period of the lattice with a defined cell and its field transfer matrix $\hat{M}_L$. Therefore the Bloch waves $\vec{E}_K(x)$ are the eigenvectors of $\hat{M}_L$ and Bloch wave numbers K are related to the eigenvalues of $\hat{M}_L$, Λ_i by $\Lambda_i = \exp(-iK_iL)$. Because $\hat{M}_L$ depends on ω and Snell's law quantity β, equation (4) can be considered as dispersion relation $\omega(K, \beta) = 0$. For birefringent media, $\hat{M}_L$ is a 4 × 4 matrix, and one ω corresponds to four wave numbers K_i. Real K_i correspond to propagating Bloch waves and imaginary K_i correspond to evanescent modes.

Based on the degeneracy of the Bloch wave numbers K_i at a specific point $\omega = \omega_0$, one can find four types of special points in the dispersion curve. The first is an inflection point corresponding to a regular band edge point (RBE), which is the degenerate point of order 2 and one ω corresponds to two equal real K's. The second type is an inflection point called stationary inflection point (SIP), which has degeneracy of order 3 and one ω corresponds to three equal real K's. The third type is inflection point is called degenerate band edge point (DBE), which has fourth order degeneracy and one ω corresponds to four equal real K's. Finally one can realize a so-called split band-edge of SBE.

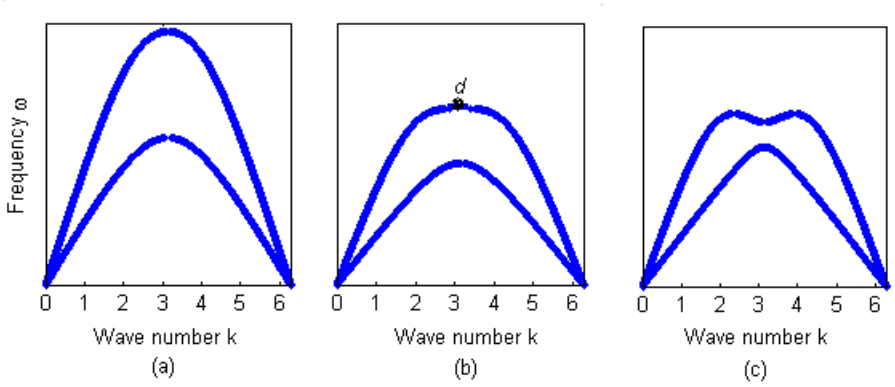

Figure 2: (a) $D_B = 0.4L$, regular band edge. (b) $D_B = 0.262894L$, degenerate band edge. (c) $D_B = 0.1L$, split band edge; where D_B is the width of the isotropic layer within each period.

Figure 2 illustrates the dispersion curves around these points. Since at the inflection points, the group velocities are all equal to 0, there is a strong field resonant effect connected with these points, but, because of their different degenerate orders, these resonant effects will differ from one to another.

Based on these predictions, we have investigated the band edge resonant field enhancement performance of anisotropic photonic crystal structures with various anisotropic materials [10]. The structure we studied has a unit cell with two misaligned in-plane anisotropic layers and one isotropic layer and simulations were based on the method described in ref [11]. By careful design of the parameters of the structure, one can design it to exhibit a degenerate band edge (DBE) around a central frequency of our choice. By making a comparison among different anisotropic materials, we have found that the giant resonant effects in the vicinity of the DBE need not only a relatively large degree of anisotropy (> 10%) but also low absorption of the materials used. We have made a number of prototypes for use at microwave frequencies using a rapid-prototyping tool. They are simple and inexpensive to make. The feature sizes are of the order of a tenth of the wavelength. Of course, another advantage of exploiting form birefringence is that the final structure is porous and lends itself to possible sensing applications, as well as the insertion of probes or other optical elements.

We believe that we are the first to observe the predicted "gigantic" field enhancement that was postulated to occur in a 1D photonic crystal designed to exhibit a degenerate band edge. However, discrepancies between the measured data and those predicted by theory and simulation revealed some other properties of the physical structure which still remain to be understood. Measured and simulated data are shown below.

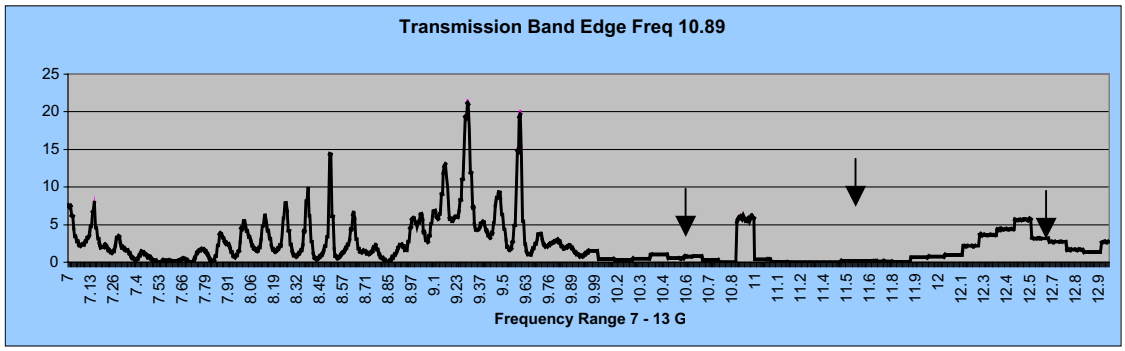

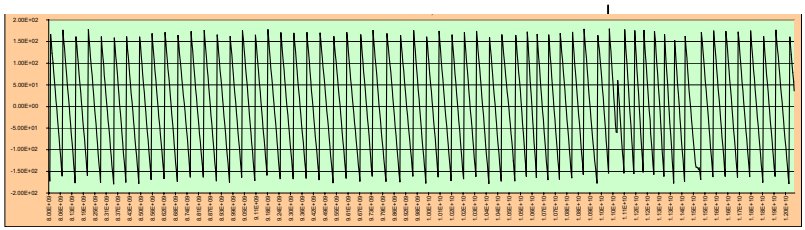

Figure 3: top graph shows measured TE-TE transmission spectrum for a finite cross section structure designed to have the response shown in the middle graph. The arrows indicate that the actual structure has a larger bandgap than expected, despite the refractive index values being accurately measured. The lower graph shows the measured phase spectrum which exhibits a phase inversion at 11.05GHz. The field enhancement occurs at a frequency close to this (10.89GHz). All three graphs have their frequency axes aligned.

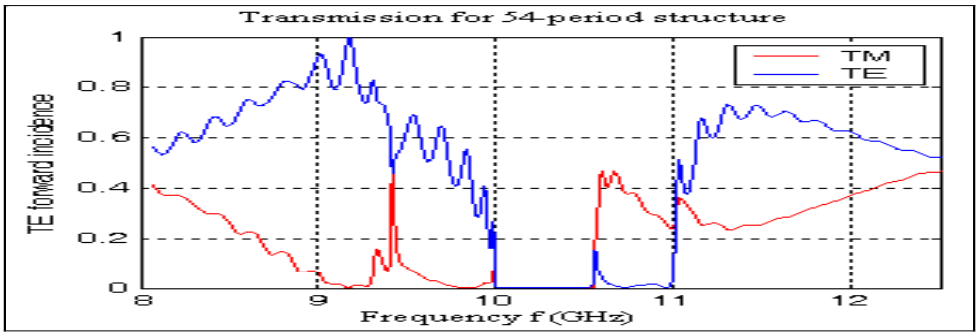

The data and the arrows above illustrate the discrepancy. Increasing the index contrast widens the bandgap but the measured indices of the form-birefringent layers are actually lower than predicted from the physical dimensions of the structure and the effective medium theory. For example, an index contrast of 1.2:1.35 has common TE and TM bandgap of width 0.6GHz, while 1.2:1.5 has common bandgap of 1GHz and 1.2:1.6 has a bandwidth of ~ 1.3GHz. By comparison, fixing the index contrast but reducing (increasing) the absolute index values shifts the bandgaps to higher (lower) frequencies but otherwise leaves the shape of the transmission spectrum the same. Thus constant contrast ratios produce the same bandgap and for example 1.2:1.35 has a band edge at 10GHz, while 1.1:1.23 shifts the edge to 10.85GHz.

The necessary condition for the existence of the DBE is that TE and TM modes should be coupled each other inside the structure so that 4×4 matrix has to be always involved to solve the dispersion relation. If TE and TM modes are decoupled, the field transfer matrix will be reduced to the block-diagonal form, the dispersion relation will exist for TE and TM modes separately, and there is no DBE point. Even if anisotropic layers are present, but the anisotropy axis in all anisotropic layers are either aligned, or perpendicular to each other, TE and TM modes are still decoupled. The only way to satisfy the DBE condition under the normal incidence is to have at least two misaligned anisotropic layers in a unit cell with the misalignment angle being different from 0 and $\pi/2$.

Design of the split band edge structure

Chabanov [12] recently presented experimental results showing a strongly resonant transmission associated with a split band edge phenomenon having near perfect impedance matching at the boundaries and polarization independence. Rotation of the angle ϕ between the anisotropic layers guaranteed a resonance for a given number of periods, N, even when N is small. He shows the superiority of SBE over DBE as a resonator and over a defect localized state in the bandgap. By an SBE resonance, he refers to a resonance at the frequency at which the two counterpropagating slow (Bloch) modes, indicated below, can co-exist. Microwave experiments were conducted with two horns and teflon rods attached to a thin ring and spectra were obtained using an HP N5230A VNA. Figotin *et al* [13] since showed that the DBE point would not be perfectly impedance matched for any polarization state, it being the result of a coupling with only one elliptic polarization state of the incident field. This paper shows that the "giant enhancement" predicted with the DBE point can still be achieved with an SBE resonance by changing ϕ. This has been our motivation for designing and fabricating a structure, with circular cross section form-birefringent layers that could be aligned and oriented with respect to each other, in order to exploit this SBE phenomenon. Our

simulations indicate an SBE-like dispersion diagram as shown below, at which we might have a single frequency at the band edge for two counterpropagating k vectors, k+ and k- , but we might also have four k vectors close to this frequency, or two frequencies at Fabry Perot resonances which are closer in frequency near the band edge.

A simulation is shown alongside of the transmission spectra for a form-birefringent periodic structure designed to be close to the DBE – SBE split. It is interesting to observe the phase inflection close to the overlapping TE (blue) and TM (red) band edges. At these frequencies we can expect a negative group delay which can be interpreted as also corresponding to a negative effective index and which qualitatively resembles the measured phase spectrum shown in figure 3. Consequently one can expect the normal guiding properties of the structure to cease at these frequencies and the field emerge from the waveguide.

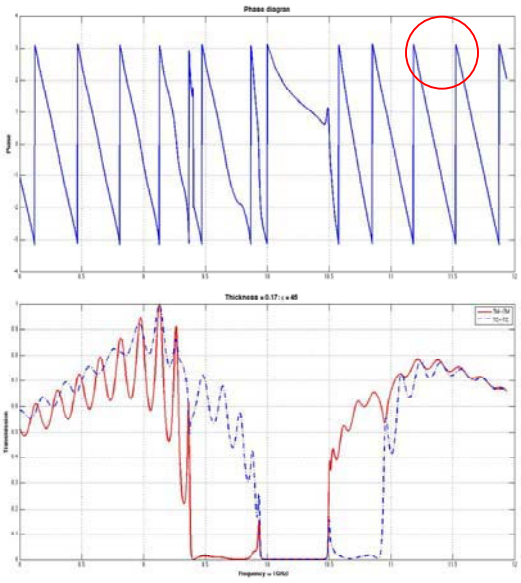

Figure 4: transmission spectrum close to DBE-

Both the simulations and the measured data show a transmitted spectral phase with a positive slope near the two common band edges. For the TE-TE case this could be responsible for the external field emission due to an effective negative index around that frequency range resulting in loss of guiding within the structure.

The first step in searching for an SBE or DBE point is to calculate the field transfer matrix for the unit cell. This depends on parameters such as the misalignment angle between two anisotropic layers φ, the dielectric permittivity and thickness of each layer, incident beam frequency ω, and incident direction θ ($\beta = n \sin\theta$, $\beta = 0$ for the normal incident situation). After the field transfer matrix of the unit cell is known, using equation (8), one can calculate the dispersion curves in our specified frequency ranges. Adjusting the misalignment angle between two anisotropic layers, and the thickness of the isotropic layer D_B, one can find a possible parameter range for the SBE or DBE point by checking the corresponding dispersion curves. For the exact DBE point, we fix one parameter such as making φ equal to $\pi/4$, and adjust another parameter such as D_B, until the desired band edge is found. Fig. 5 shows the dispersion curve and an SBE behavior indicated by the red arrow.

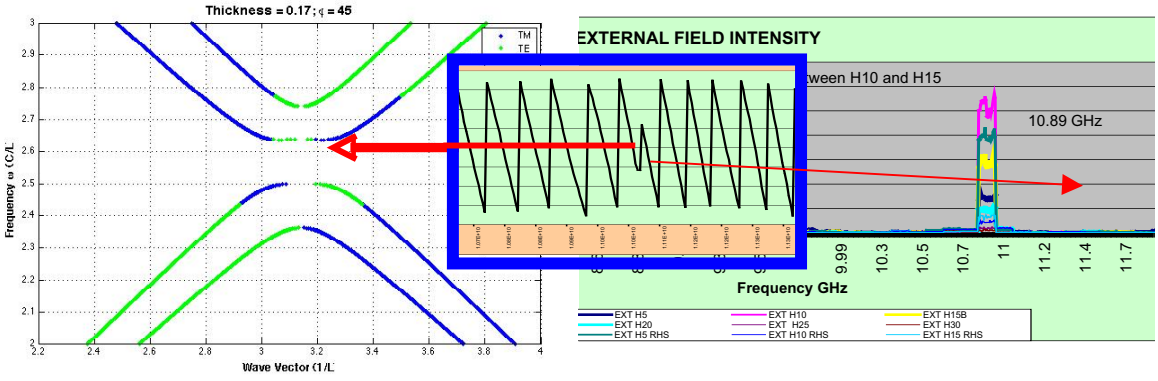

Figure5: dispersion diagram indicating the split band edge (left) and the associated measured phase inflection (center) and external field all at ~11GHz. Data were measured from a 52 period structure with measurement holes, Hn, along its length separated by 1.2 cm and with n = 1 to 52, n = 1 being the input end to the structure.

1.64. The entire structure consisted of up to 55 periods or unit cells, with each unit cell made up of three layers A1, A2 and D as shown in figure 6. A1 and A2 are identical subwavelength 1-D grating layers having a $\phi = 45$ degree grating vector orientation with respect to each other, and the D layer in this case is simply air. The thickness of one unit cell L = 1.23 cm, the thickness the anisotropic layer $D_{A1} = D_{A2} = 0.42$ L = 0.51cm, and the thickness of the air layer $D_B = 0.18L = 0.22$ cm. The period of the form birefringent grating $\Lambda = 1$ mm, which is about 1/30 of the incident wave wavelength, with a duty cycle 0.5. Effective medium calculations give $n_o = 1.36$, $n_e = 1.21$, which defines the dielectric tensor of the effective uniaxial thin film.

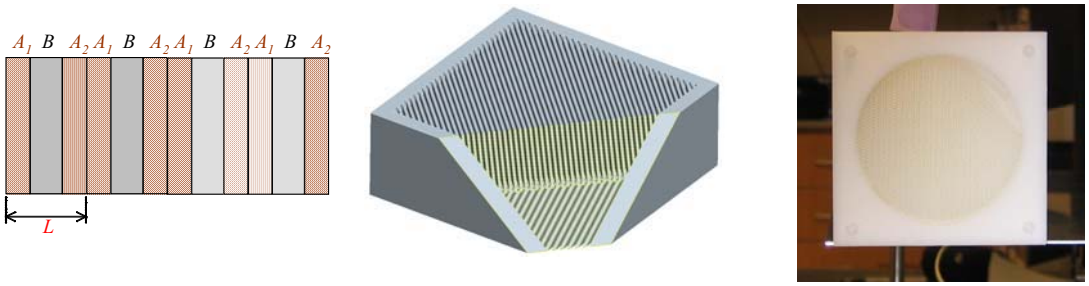

Figure 6: the physical structure: schematic, CAD diagram and actual element

Discussion and conclusions

Some important comments are appropriate at this time. Fairly sharp Fabry-Perot resonances can be seen, as expected, despite the fact that we have only an approximation to an incident plane wave. Also, it is well known that disorder or defects in the photonic crystalline structure can have a significant effect on the transmission properties especially near a band edge. Mookherjea and Oh [14] argue that the strongest effects are at the band edge and conclude that, at least for the case of resonator coupling, variations in coupling coefficients of 1% to 10% can lead to reduced slow down factors (X10 to X30) because of band tail effects. Also, Freilikher et al [15], when modeling 1D "periodic-on-average" structures show that localized states (resonances) can occur in pass and stop bands.

More needs to be done to fully understand the observed results but nevertheless, these data are in good qualitative agreement with the Figotin model. Measurements of the associated field intensity enhancement were made. Large enhancements are seen up to factors of 80 a frequencies, as shown below in figure 7. The spatial position of the maximum field is observed near hole 15, the structure having small openings in each period for a probe, hole 1 being closest to the source.

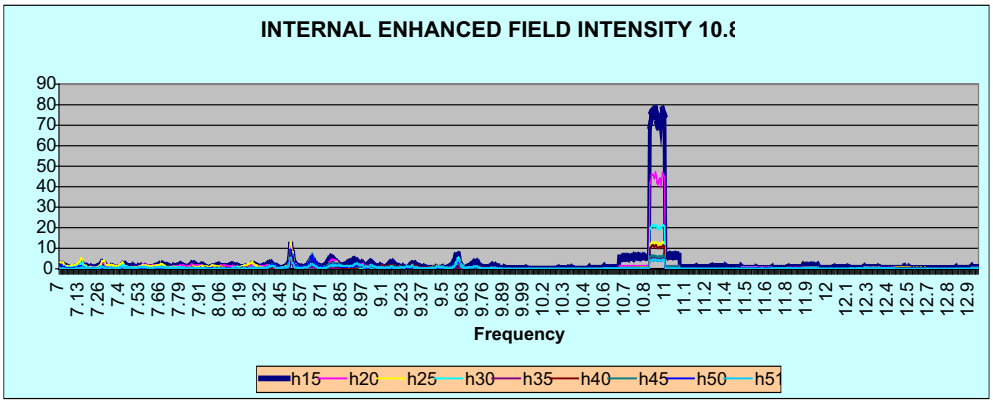

Figure 9: field intensity measurements inside the structure at different spatial locations, as a function of frequency, showing an enhancement factor of x80; on the right, predicted enhancement factors for approximately the same number of periods and a structure with an inherent material loss of 0.0035cm^{-1}.

That the peak enhancement occurs toward the input face of the structure is consistent with simulations in which the material properties exhibit some loss. Absorption losses can be seen to be quite significant but the measured enhancement we observed of 80 is consistent with the blue dashed curve in the lower left diagram. It is interesting to note that the initial rate of growth of the field is virtually independent of the number of periods, *N*. This is very encouraging since we can assume that an incident pulse experiences a significant slowdown factor corresponding to a large effective group index. It is this that can be exploited, where the field enhancement is at its largest, for sensing and superresolved imaging.

Significant and highly directional and frequency-specific fields were measured outside of the structure. The mechanisms responsible for this are likely to be due to the effective negative index at those frequencies. This may not be surprising since unusual scattering effects have been reported by others from aperiodic photonic structures [e.g. 16]. Also, as has been known for many years [e.g 17], the effective refractive index can become less and unity, zero or negative leading to ultra refractive or diffractive effects near a bandgap. These all trace back to Notimi [18] who explains superprism effects and negative refraction and discusses high resolution 3D photography using negatively refracting photonic crystals.

In summary, we have described a highly anisotropic 1D photonic crystal structure that was designed to exhibit maximum pulse delays and large field enhancements close to a degenerate band edge. The structure was designed by exploiting form birefringence for a number of reasons. Initially it was done because there are no materials that could easily be used to realize this phenomenon at optical frequencies. Additional advantages however, for both optical and microwave applications are that the structures are low cost and easy to manufacture and they can be porous. The large field enhancements possible both inside and outside the structure are a function of the number of periods, N, and are predicted to increase as the fourth power of N. This dramatic effect lends itself to exploiting those enhanced fields for increased antenna sensitivity and increased sensor sensitivity where large intensities are required (see for example [20]). Because of the very large group index, objects inside or possibly inset on the surface of the structure, will be probed by much shorter wavelengths allowing higher resolution imaging or testing of those objects. One can also imagine the slow wave structure to be somewhat similar to a very high index immersion lens. Finally, our ability to tune the SBE to find a strong resonance provides an important degree of freedom not only to maximize the field enhancement internally but also it appears to control the emission frequency. We have observed that as a function of local structural changes and disorder, the transmission phase inflection can occur at multiple frequencies, some of which are associated with an effective negative index. This opens up the possibility of exploiting a structure such as this for phased array applications and local control of refractive index for imaging and sensing applications. Very preliminary data from external field measurements indicate some potentially powerful applications arising from the control of near and far field beam patterns around the structure. These could be actively exploited for communication purposes or for sensing once the full parameter set determining the control of these external properties are fully understood. Under certain conditions, reciprocity holds which further extends possible applications.

ACKNOWLEDGEMENTS

The authors acknowledge the support of DOE grant DE-FG02-06CH11460 and DARPA/ARL through grant W911NF-05-2-0053, UNC GA RCF 07-08-2-02267-18 and the Charlotte Research Institute. We also acknowledge A. Figotin and I. Vitesbskiy whose theoretical work, referenced in the paper, provided the framework for our simulations and fabrication efforts.

APPENDIX B: References

1. A. Figotin and I. Vitebskiy, “Oblique frozen modes in periodic layered media,” *Phys. Rev. B*, **68**, 036609 (2003).

2. A. Figotin and I. Vitebskiy, “Gigantic transmission band-edge resonance in periodic stacks of anisotropic layers”, *Phys. Rev. E* **72**, 036619 (2005).
3. J. Ballato and A. Ballato, "Materials for freezing light", *Waves in Random and Complex Media*, **15**, 113-188, (2005)
4. A. Kanaev, Y. Cao, and M. A. Fiddy, "Axially frozen modes in finite anisotropic photonic crystals", *Opt. Eng*., **44**, (9), (2005).
5. Yang Cao, Michael A. Fiddy, “Resonant effect analysis at finite one-dimensional anisotropic photonic crystal band edges”, *Proc. SPIE*, **6128**, 345-356 (2006).
6. M. Scalora, R. J. Flynn, S. B. Reinhardt, and R. L. Fork etc. “Ultrashort pulse propagation at the photonic band edge: large tunable group delay with minimal distortion and loss”, *Phys. Rev. E* **54,** R1078-R1081 (1996).
7. A. Mandatori et al, “Birefringence in one-dimensional finite photonic bandgap structure”, J. Opt. Soc. Am. B, 20, p504, (2003)
8. P. Yeh, “Electromagnetic propagation in birefringent layered media”, *J. Opt. Soc. Am*. **69**, 742, (1972).
9. I. J. Hodgkinson and Q.-H. Wu, *Birefringent Thin Films and Polarizing Elements*, World Scientific, New Jersey, 1998.
10. A. Figotin and I. Vitebskiy, “Frozen light in photonic crystals with degenerate band edge”, *Phys. Rev. E*, **74**, 066613 (2006)
11. Y. Cao, J. O. Schenk and M. A. Fiddy, “Third order nonlinear effect near a degenerate band edge” (submitted for publication).
12. A.Chabanov, “Strongly resonant transmission of electromagnetic radiation in periodic anisotropic layered media”, arXiv:0709.1250v1 [physics.optics] 9 Sep 2007.
13. A. Figotin and I. Vitebskiy, “Slow wave resonance in periodic stacks of anisotropic layers,” *Phys. Rev. A*, **76**, 053839 (2007).
14. S. Mookherjea and A. Oh, “Effect of disorder on slow light velocity in optical slow-wave structures”, Optics Letters, Vol. 32, p289, (2007).
15. V. Freilikher et al , “Enhanced transmission due to disorder”, Phys Rev E vol. 51, p6301, (1995).
16. L. Dal Negro et al, “Spectrally enhanced light emission from aperiodic photonic structures”, App. Phys. Lett., 86, 261905, (2005).
17. J. P. Dowling and C. M. Bowden, “Anomalous index of refraction in photonic bandgap materials”, J. Mod. Optics, 41 No. 2 p345 – 351, (1994).
18. M. Notimi et al, “Theory of light propagation in strongly modulated photonic crystals: refractionlike behvior in the vicinity of the photonic band gap”, Phys. Rev. B, Vol 62, No 16, Oct 2000, p 10 696 – 10 705.
19. E. LeCoarer et al, “Wavelength-scale stationary wave integrated Fouirer transform spectroscopy”, Nature Photonics, Vol 1, p473, (2007).

APPENDIX C: PHOTOS OF FINAL EXPERIMENTAL TEST SETUP

These photos offer the reality association to theoretical explanations of model structures described within the final experimental section. They also serve to help think about experimental limitations and how to possibly affect helpful changes. These same photo also help to more closely understand how to best setup the model simulations given both the real circumstance and devices. Last point here is that this collection can possibly help explain why the measured results in chapter 7 appear as they do.

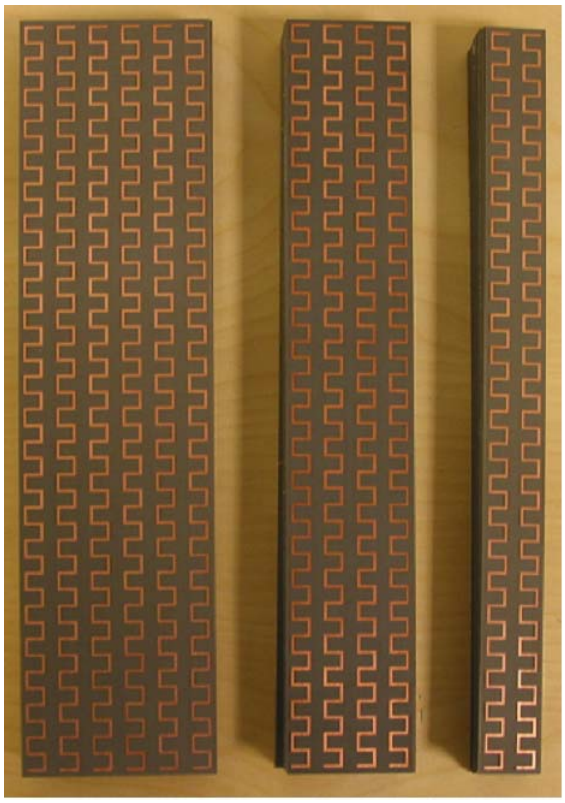

FIGURE 111: Three S models, referred to as 6S, 4S and 2S respectively

FIGURE 112: Styrofoam structure designed to hold S models in place for test

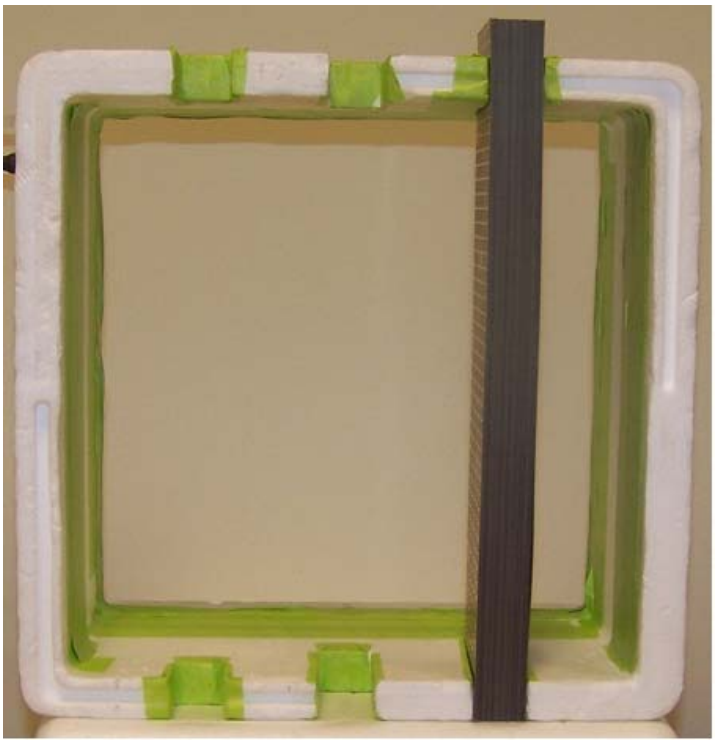

FIGURE 113: Here is an example demonstrating a model held in place for test

FIGURE 114: Aluminum test mask sheet with cut out holes used as image objects

FIGURE 115: Shown is a 2S model placed in front of double slits

FIGURE 116: Test setup with 4S model and the plane wave transmitter on right

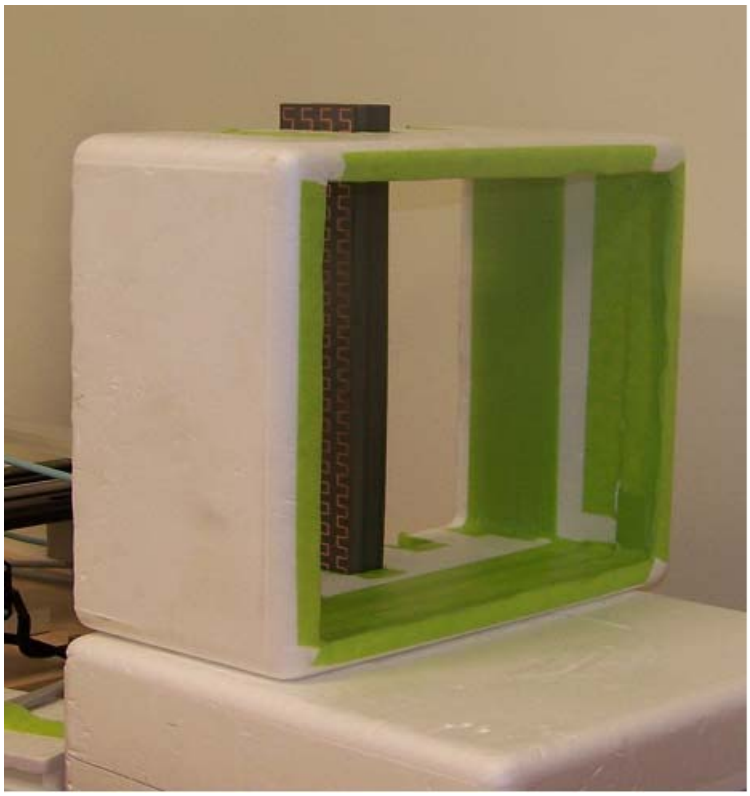

FIGURE 117: Back side view of 4S model as seen by the transmitter on right

FIGURE 118: Side view of the experimental test setup

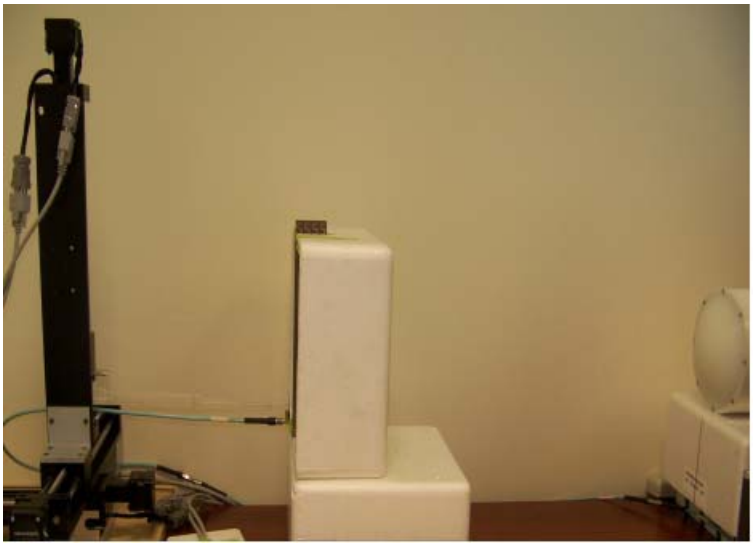

FIGURE 119: This is a side view of the 4S model being radiated from the right side

APPENDIX D: TEST AREA VIEWS OF THE MEASUREMENT PROBE

It's important to clearly see how the measurement is being made with respect to the actual model being sampled. This allows for a more comprehensive understanding of the results and how to effectively judge results. These FIGURES show to scale the actual physical limitation of probe placement as well as testable area. Last thought here is that these images can model a circumstance in the future for improved measurement techniques.

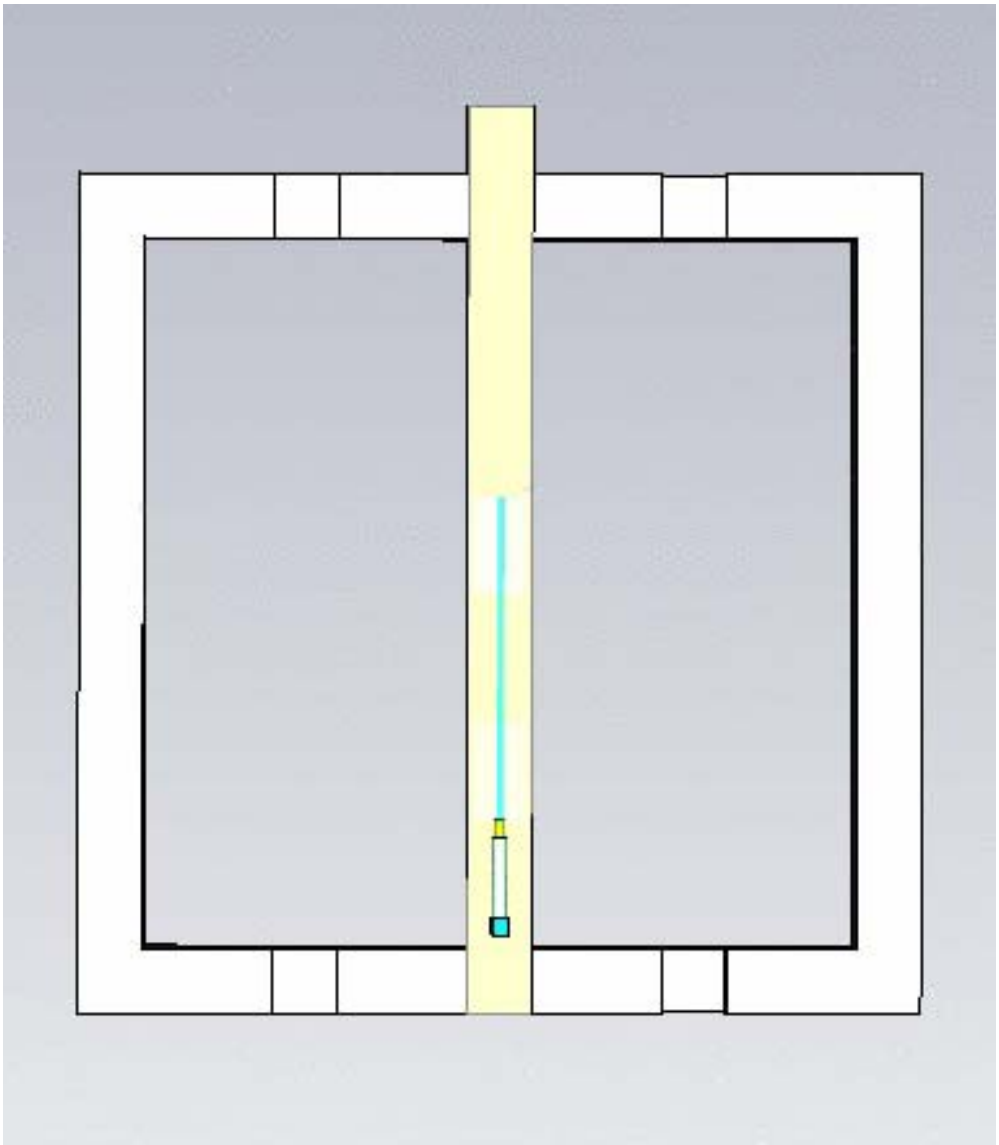

FIGURE 120: Test probe placement below the blue 10 by 10 cm test area

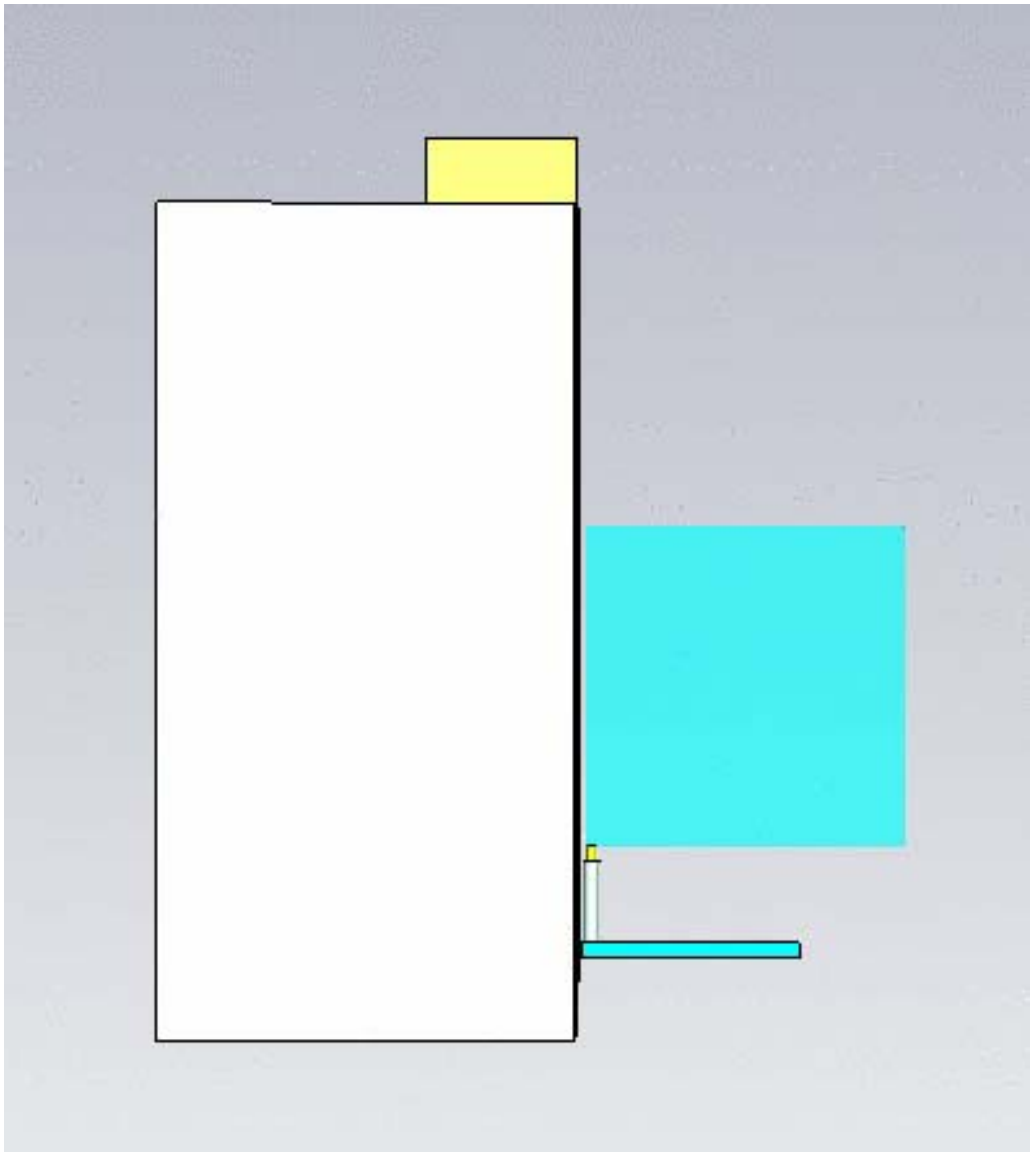

FIGURE 121: Side view of the test probe shown below the blue 10 by 10 cm area

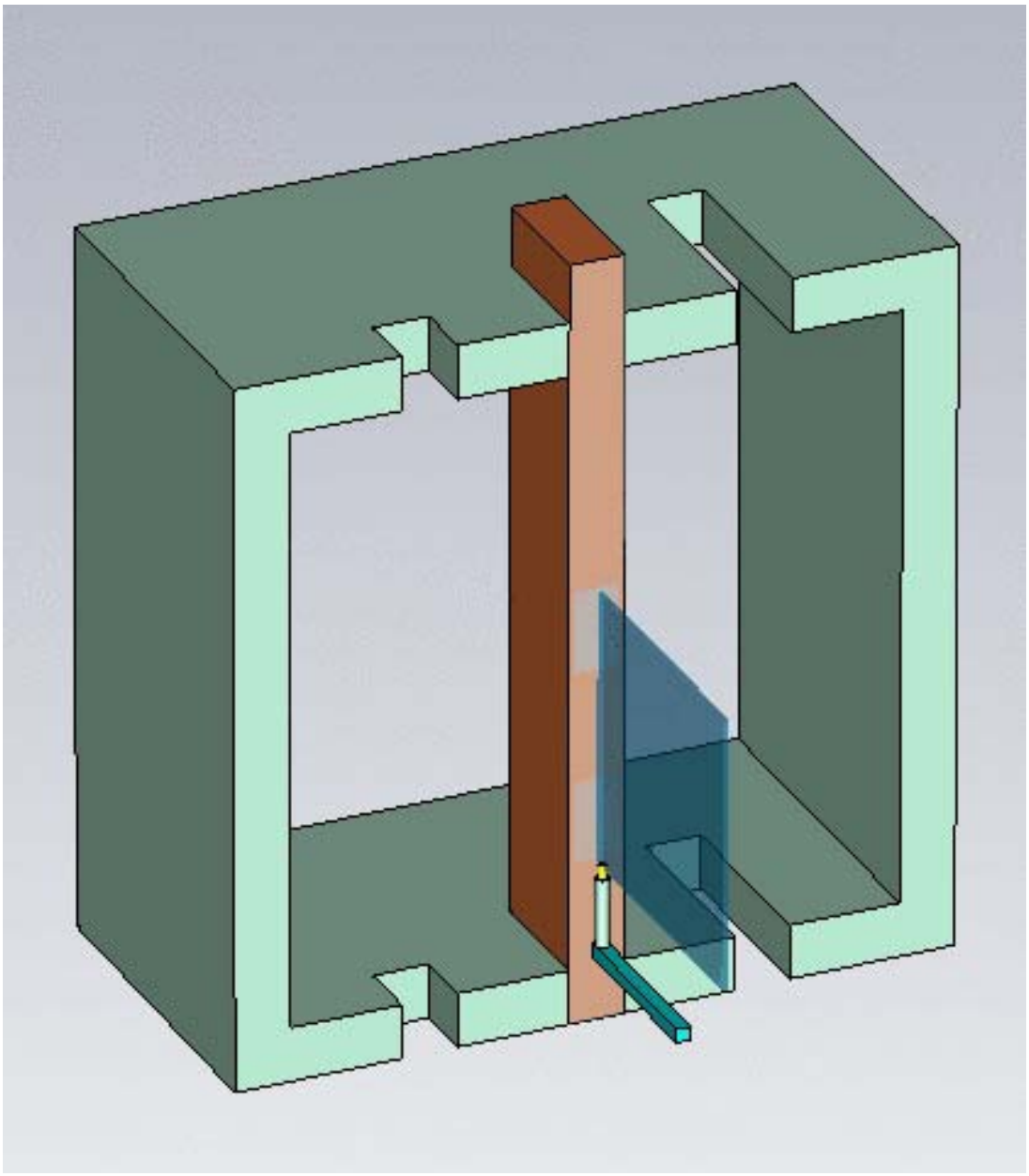

FIGURE 122: Test area perspective and its relative location along the 4S model

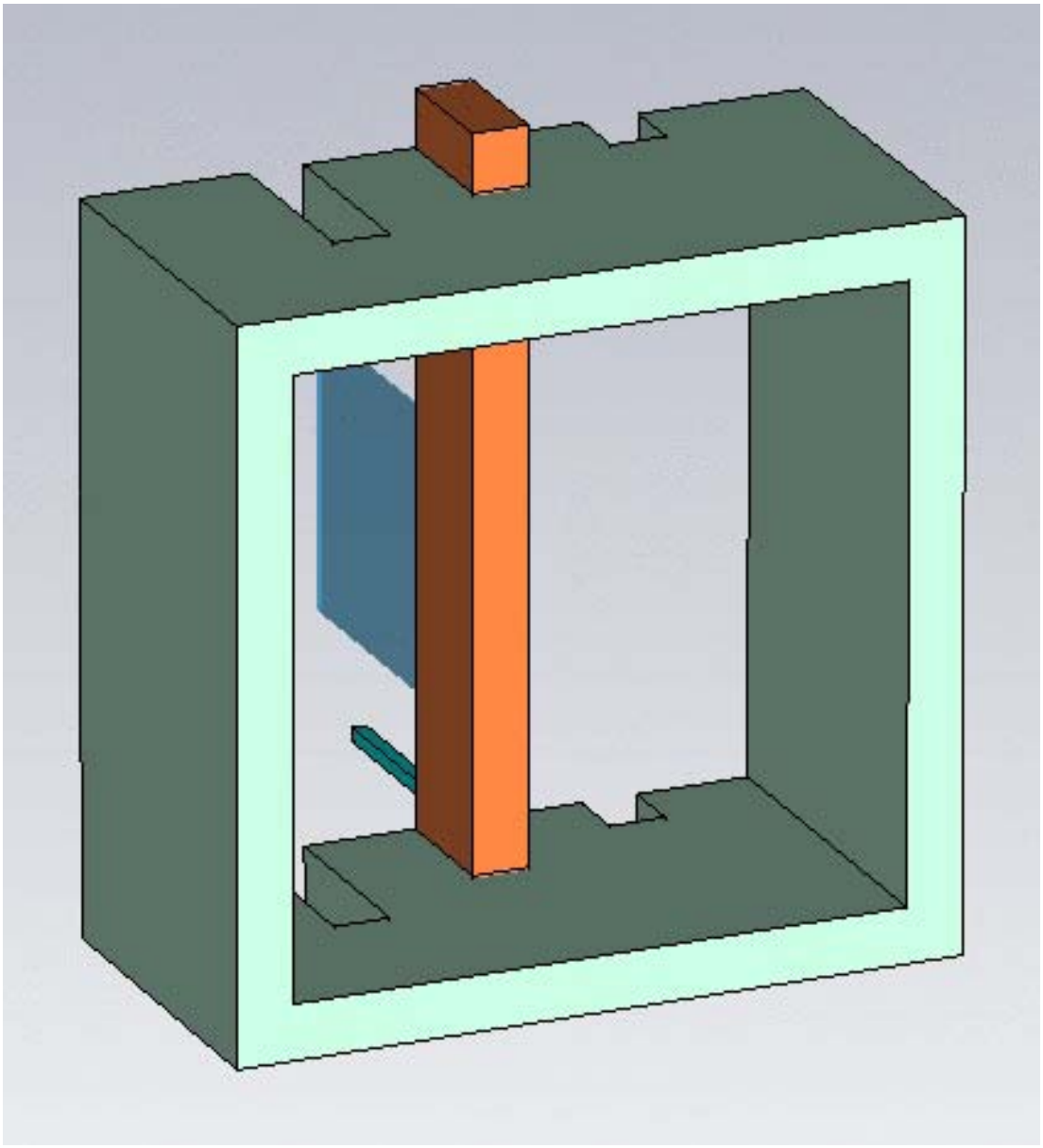

FIGURE 123: Backside view of the 4S model displaying the surrounding space

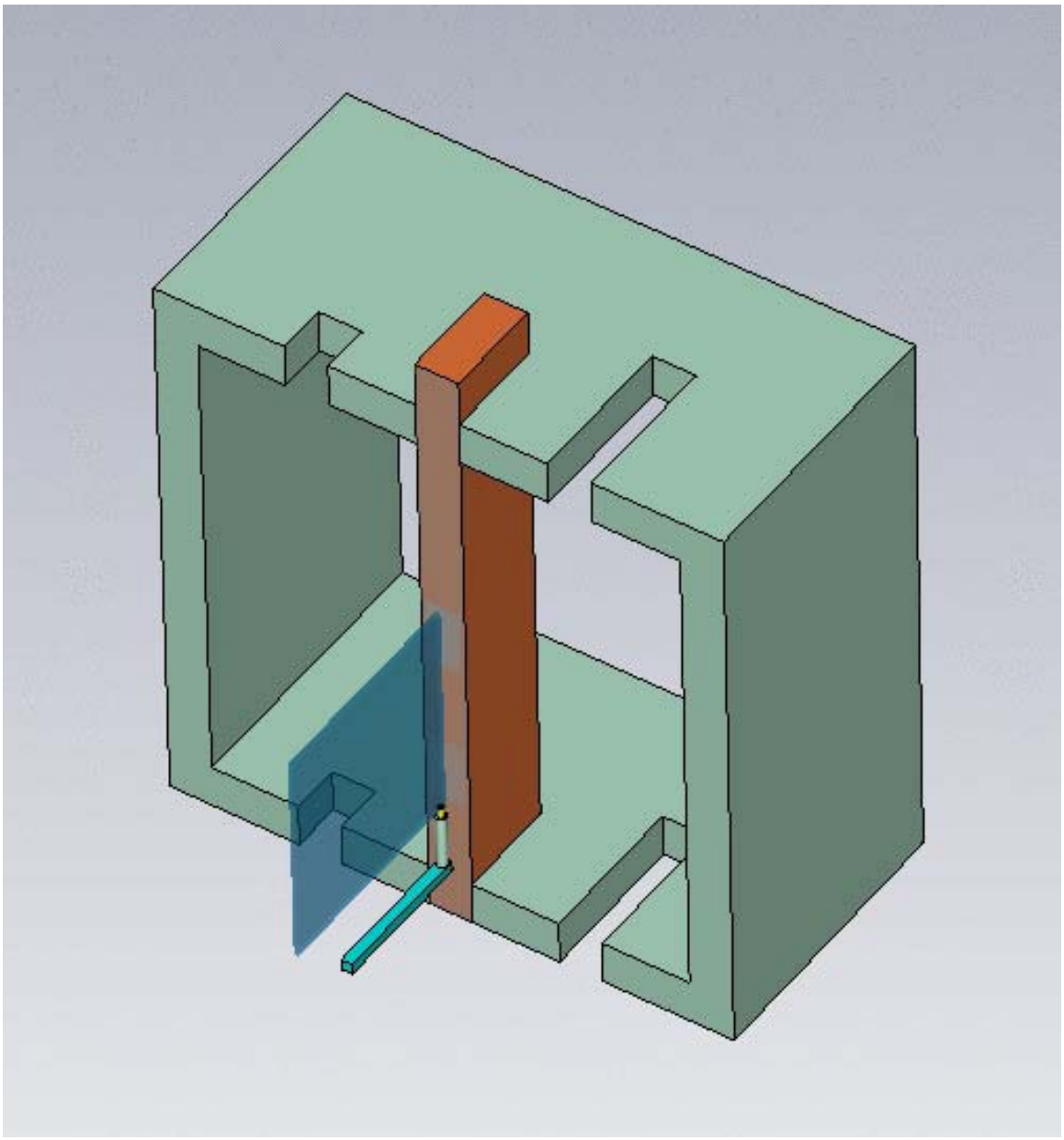

FIGURE 124: Top down view perspective of the test area

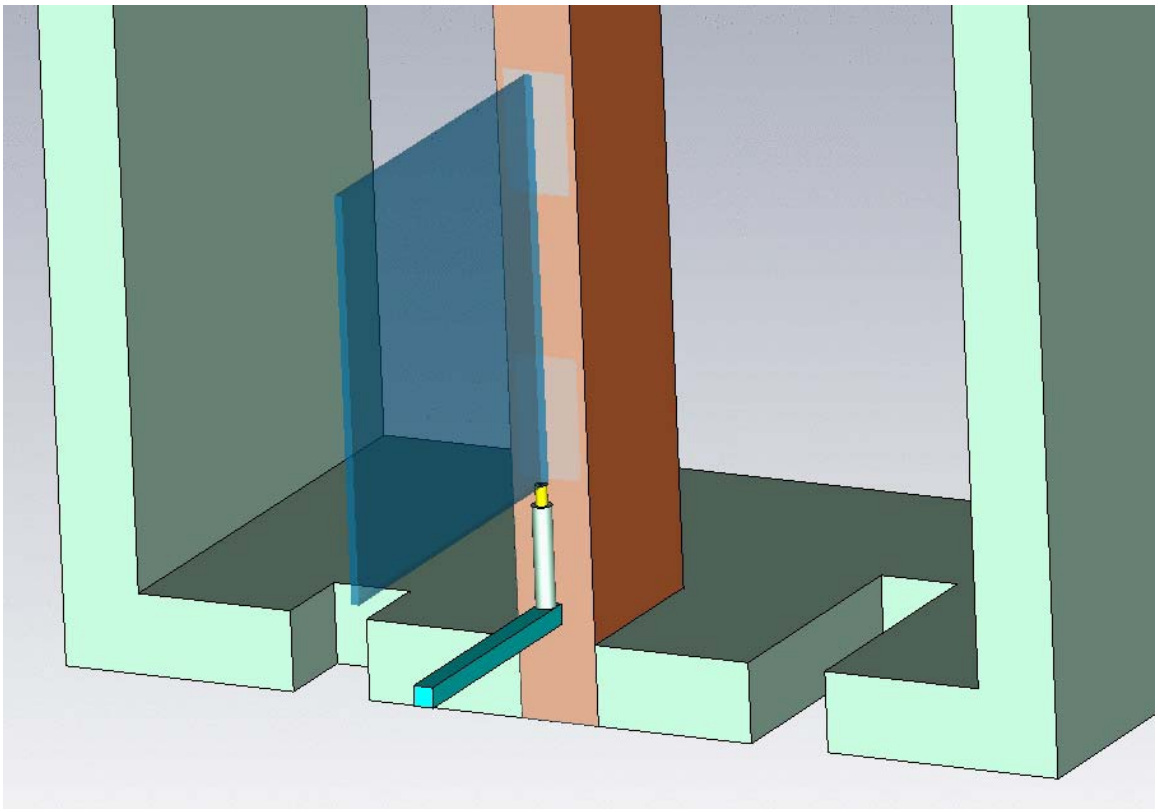

FIGURE 125: Enlarged detail of the test probe underlying the select test area

APPENDIX E: PLANAR CONVEX LENS POWER DENSITY RESPONSE

These additional images are intended to show what the correspondence would be to power density measurements, which is actually what could be physically measured using a spectrum analyzer. The power density measurements are the only microwave measurements available for direct energy density association as well. Power density measurements are also used to construct images of wave transitions before and after regions of interest. These images though somewhat similar to section 6.2 have the decided advantage of clearly painting the focused spots with direct correspondence power concentration and this can not be shown directly with just electric field measurements because this excludes the magnetic field which is absolutely required for actual power measurements. Also power density can more reliably follow absorption and the related mechanisms. These simulations can also be used to quickly judge how well a system responds internally as well.

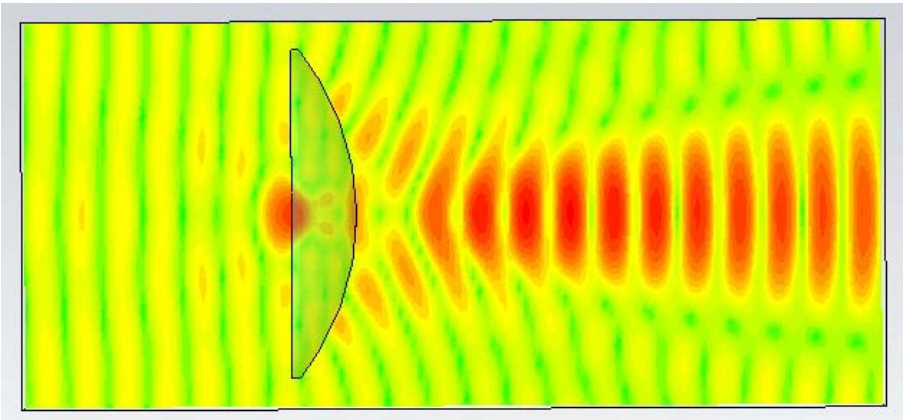

FIGURE 126: 20 GHz plane wave being focused by a planar convex lens

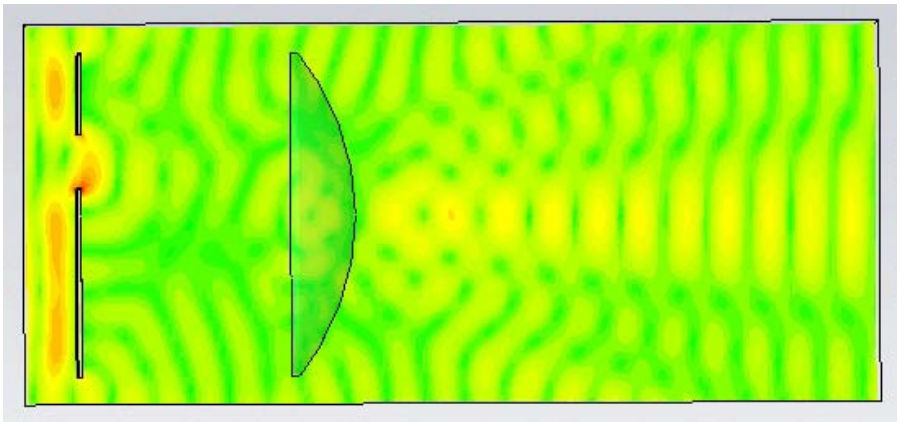

FIGURE 127: 20 GHz plane wave passing through a single slit object

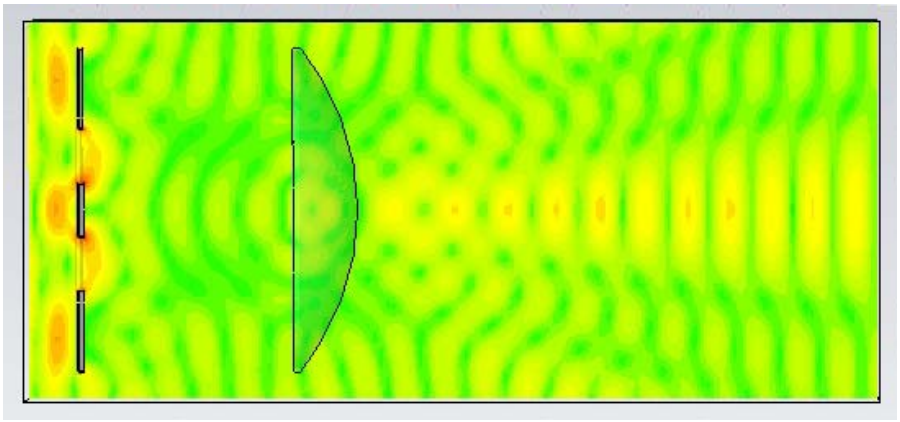

FIGURE 128: 20 GHz plane wave passing through a double slit object

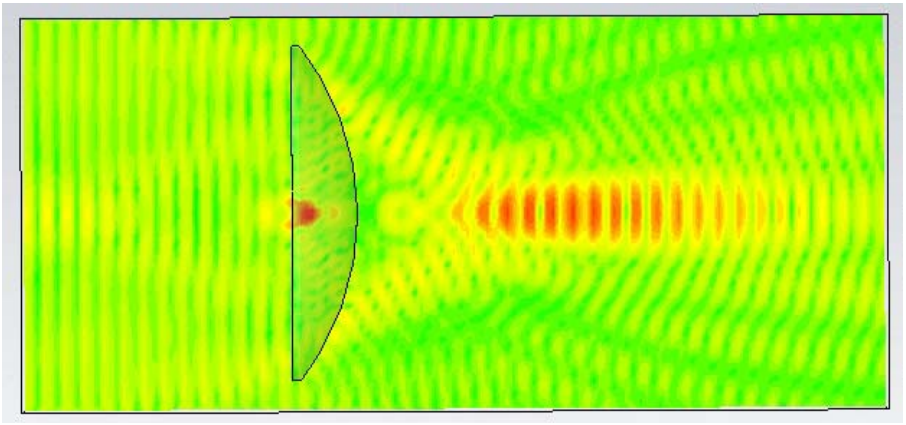

FIGURE 129: 40 GHz plane wave being focused by a planar convex lens

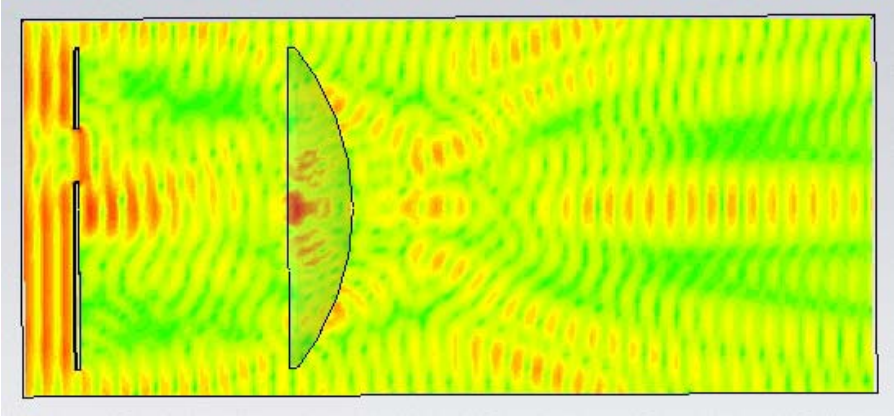

FIGURE 130: 40 GHz plane wave passing through a single slit object

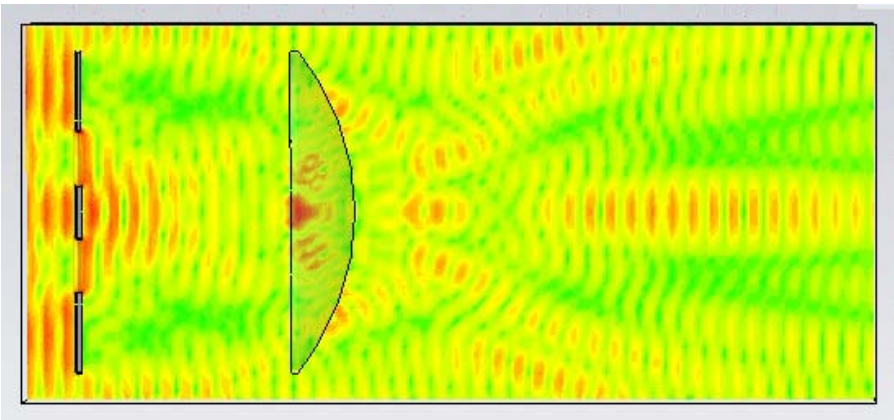

FIGURE 131: 40 GHz plane wave passing through a double slit object

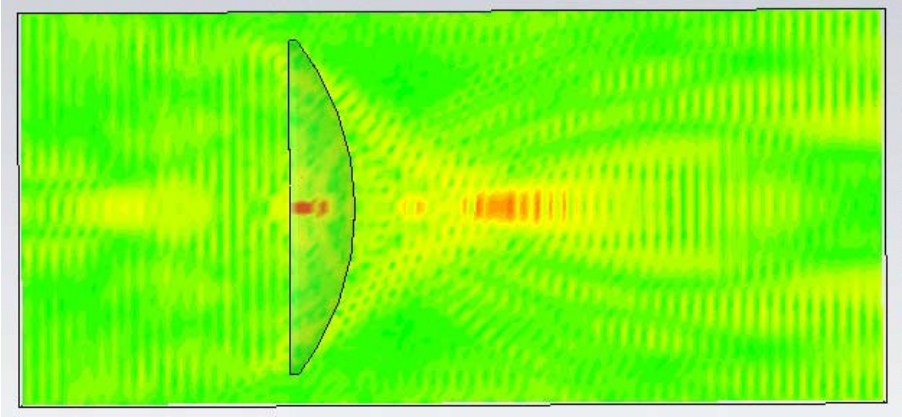

FIGURE 132: 60 GHz plane wave being focused by a planar convex lens

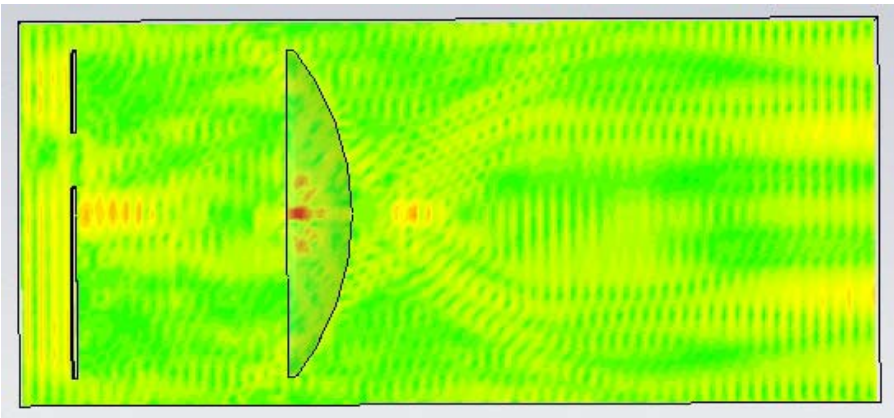

FIGURE 133: 60 GHz plane wave passing through a single slit object

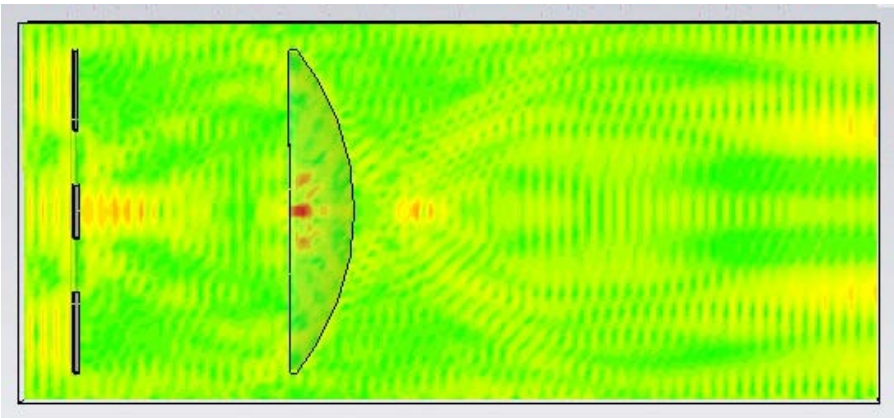

FIGURE 134: 60 GHz plane wave passing through a double slit object

APPENDIX F: ELECTRIC FIELD ENHANCEMENT

Figotin talks of the enhancement in the DBE structure as being an enhancement of field intensity, which means a build up of real power inside the structure due to the massive slow down velocity plus multiple reflections back and forth (as in a laser cavity) that is especially pronounced at the DBE hence the N^4 dependency rather than the usual laser cavity or etalon enhancement of N^2.

For the negative index lens, Pendry is quite clear that this is an amplification and the driving source of this, is again a resonance between the back and front face of the slab of the surface plasmon waves, seen as one approaches n = -1 as very high intensity surface waves. There is one surface wave for every high-k evanescent wave that is strong enough to reach the far side of the lens and generate a surface wave there as well as on the front face. There is a high k cut off that is lower and lower eventually collapsing to just the propagating wave (TM) highest k as the losses increase ¦the evanescent decay having been totally lost due to the material losses.

In the following pages there will be a fundamental circuit association as well to help further describe the idea of enhancement. Field enhancement will be related to voltage enhancement. These circuit analogies provide a material comparison in terms of the permittivity and permeability.

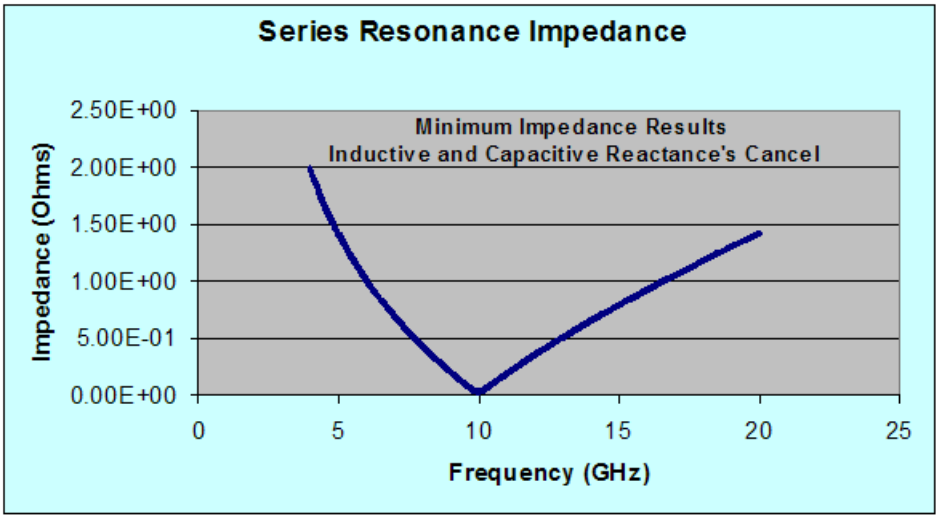

FIGURE 135: Minimum series resonant impedance dip at 10 GHz

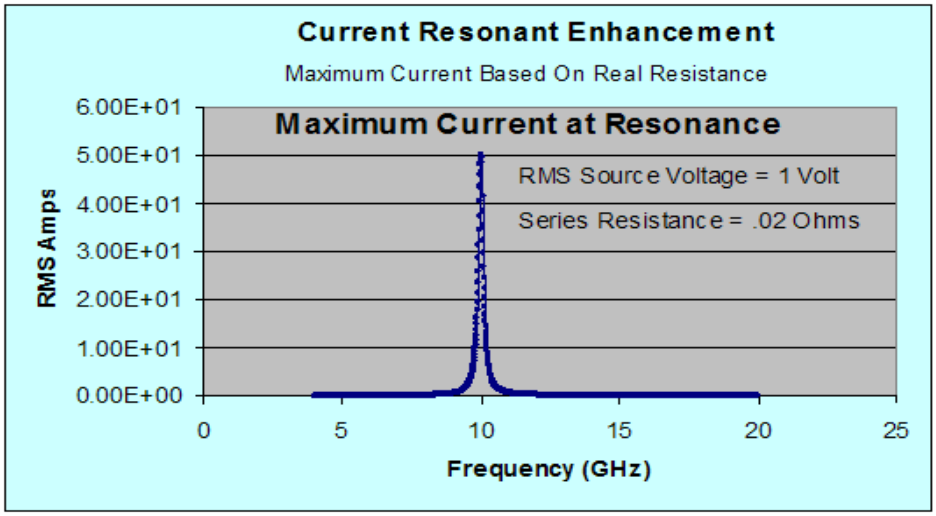

FIGURE 136: Maximum resonant current response at 10 GHz

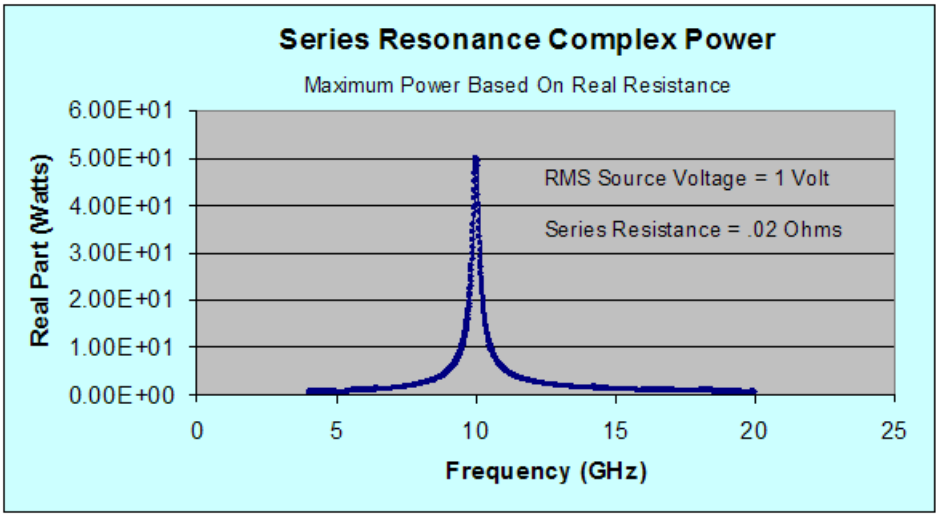

FIGURE 137: Real part of complex power, the average value

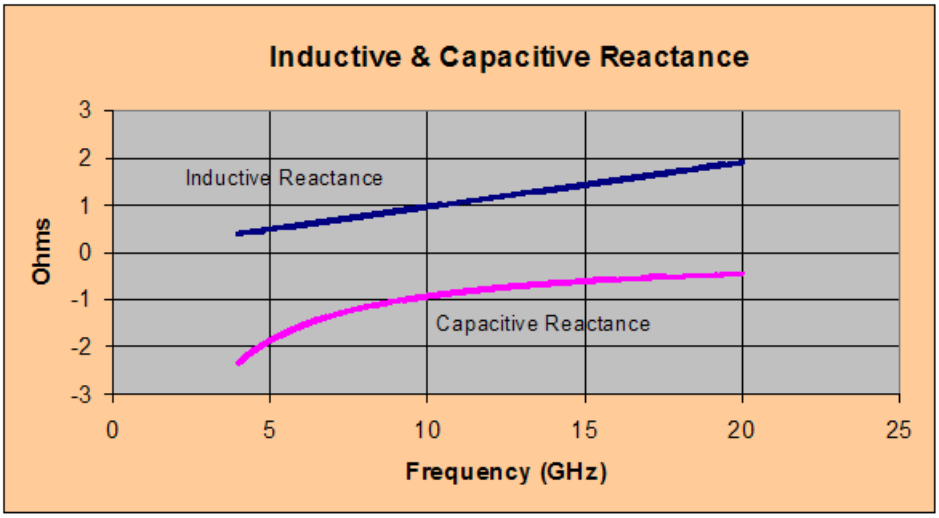

FIGURE 138: Inductive and capacitive reactance curves 180 degrees out of phase

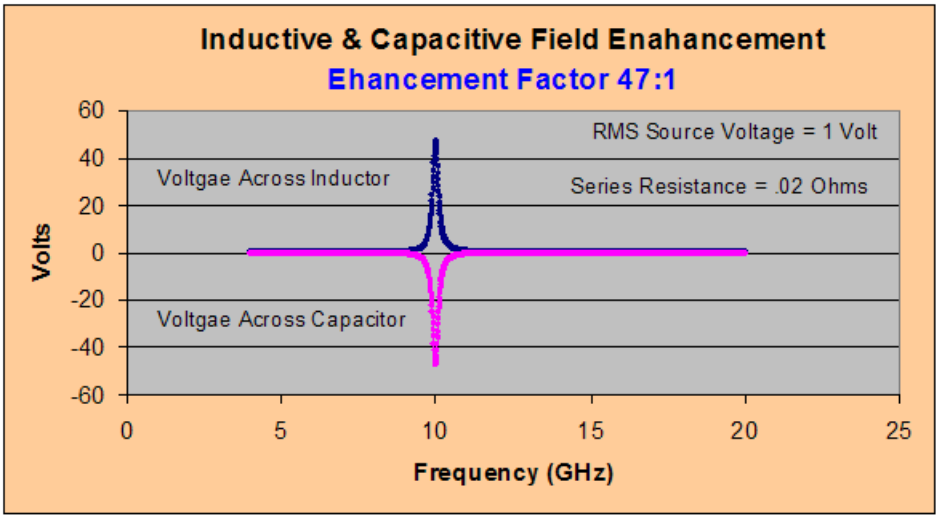

FIGURE 139: Voltage enhancement of 47:1 across the inductor and capacitor

Please refer to FIGURES 1 through 5 for the following discussion describing field enhancement. A special condition exists in an RCL (Resistance, Capacitance and Inductance) circuit, when it is energized at a frequency at, which the inductive reactance is equal to the capacitive reactance, $x_L = x_C$. As inductive reactance x_L increases as frequency increases, capacitive reactance x_C decreases, but there is one frequency at which they are both equal and this is shown in FIGURE 4. This is the resonant frequency of the circuit. Shown in FIGURE 29 is a depiction of an equivalent circuit representation of the S model consisting of three branches composed of series resonant circuits. At the resonant frequency there will be electric field strengths that exceed the applied field at various locations due to the series resonance phenomena, depicted in FIGURE 5. This apparent increase is typically referred to as an enhancement given the passive nature of the circuit. This field enhancement can sometimes have several orders of magnitude greater than the applied excitation, but the available current capacity will be limited to the extent of the series resistance, shown in FIGURE 2. The maximum power that can be

realized will not exceed that produced by the applied excitation and the resulting resonant current as seen in FIGURE 3. In most all cases the current limit available from the field enhancements are significantly reduced below the available resonant current, due mostly to the fact that the reactive components are in fact passive and not able to support any sustained current supply. In fact if the field enhancement is not correctly coupled out, then the field will become a fast acting exponential decay that will completely diminish the enhancement. Field enhancements are used to couple into high impedance devices or regions, after which further processing could be applied to preserve the effect. It's important to keep clearly in mind that the law of conservation of energy is not being violated but instead maintained. Massive field enhancement can sometimes cause ionization of the intervening column of gas between the regions if not correctly anticipated. As mentioned in the early part of the dissertation spark gap transmitters employ field enhancement except in that case, parallel resonance is being used. Parallel resonance differs from series resonance by the specific parameter being enhanced. Series resonance seen in FIGURE 1 leads to maximum current at resonance where as parallel resonance results in minimum current. In either case the strong field enhancements can be achieved. The choice of which topology to use is decided by the associating impedances and effects. So in summary field enhancement is used typically in association with passive circuits that have either series or parallel resonance.

APPENDIX G: DISPERSION RELATION AND PHASE VELOCITY

Wave Equation: $$\nabla^2 \vec{\mathrm{E}} + \omega^2 \mu\varepsilon \vec{\mathrm{E}} = 0$$

Example $$\frac{\partial \mathrm{E}_y}{\partial x^2} + \omega^2 \mu\varepsilon \mathrm{E}_y = 0$$

$$\vec{\mathrm{E}}(y,x) = \hat{y}\mathrm{E}_{oy} \exp(-jkx)$$

Dispersion $$(-k^2 + \omega^2 \mu\varepsilon)\mathrm{E}_o = 0$$

$$k^2 = \omega^2 \mu\varepsilon$$

Transform back into space and time. $$\vec{\mathrm{E}}(x,t) = \hat{y}\mathrm{E}_o \cos(\omega t - kx)$$

Spatial variation in successive time $$\lambda = \frac{2\pi}{k}$$

k is the change in phase over distance $$k = \frac{2\pi}{\lambda}$$

Require the phase of the wave to be constant $$\omega t - kx = 0$$

Derivative of x with respect to time $$\frac{dx}{dt} = velocity_{Phase} = \frac{\omega}{k}$$

APPENDIX H: DRUDE MODEL AND PHASE VELOCITY

$$\sigma(\omega) = \frac{f_o N e^2}{m(\gamma_o - j\omega)}$$

Drude Model of conductivity

$$\varepsilon(\omega) = \varepsilon_{dipole}(\omega) + j\frac{f_o N e^2}{m\omega(\gamma_o - j\omega)}$$

Low Frequency Anomolous Dispersion with Gama as damping constant

$$\omega_{Plasma}^2 = \frac{NZe^2}{\varepsilon_o m} \qquad \varepsilon(\omega) = \varepsilon_{dipole}(\omega) - j\frac{\omega_{Plasma}^2}{\omega}\varepsilon_o$$

NZ Number of electrons per unit volume m is the effective electron mass and e is the electron charge.

$$V_{Phase}(\omega,\sigma) = \frac{1}{\sqrt{(\varepsilon_o\varepsilon_r)(\mu_o\mu_r)}} \cdot \left[1 - \frac{1}{8}\left[\frac{\sigma}{\omega(\varepsilon_o\varepsilon_r)}\right]^2\right]$$

Phase Velocity as a function of frequency and conductivity

Drude model obeys Ohm's Law $\vec{J} = \sigma\vec{\mathrm{E}}$

APPENDIX I: IMAGE DISTANCE DERIVED FROM SNELL'S LAW

$$imageDist(\theta_i, LensThick, n_{Model}, objectDist) =$$

$$\frac{LensThick \cdot \cos\left[\theta_{inc} \cdot \frac{\pi}{180}\right]}{\sqrt{n_{Model}^2 - \sin\left[\theta_{inc} \cdot \frac{\pi}{180}\right]^2}} - objectDis$$

This result demonstrates how image distance will vary for all indices around n = –1 index. For indices above and below n = –1, this result further shows that only a limited range of k vectors will pass from object to image space.

n = -1 index required to demonstrate perfect image formation

Perfect image formation will consist of all transmitted k vectors (evanescent and propagating) from object to image space. This includes coupled evanescent surface waves.

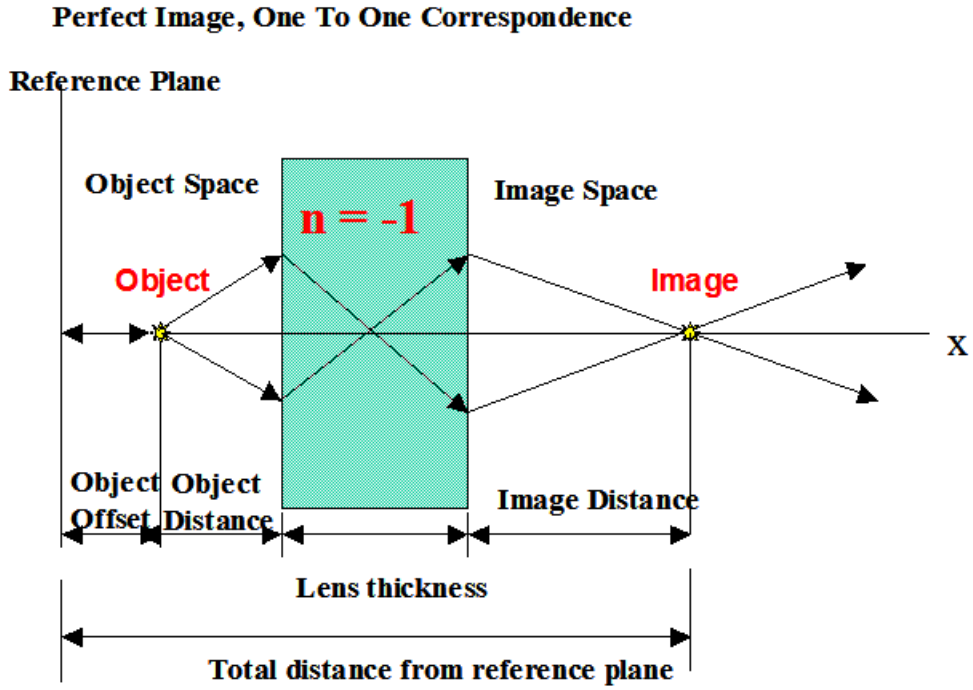

FIGURE 140: Object image relationship associated with a negative index metalens